EBERHARD KARLS
UNIVERSITÄT
TÜBINGEN

Zentrum für Angewandte Geowissenschaften (ZAG)

TÜBINGER GEOWISSENSCHAFTLICHE ARBEITEN (TGA)

Reihe C: Hydro-, Ingenieur- und Umweltgeologie

Benedict Miles

Practical Approaches to Modelling Natural Attenuation Processes at LNAPL Contaminated Sites

TGA, C105, 2007

Practical Approaches to Modelling Natural Attenuation Processes at LNAPL Contaminated Sites

Dissertation
zur Erlangung des Grades eines Doktors der Naturwissenschaften

Der Geowissenschaftlichen Fakultät
der Eberhard-Karls-Universität Tübingen

vorgelegt von
Benedict Miles
aus Blackburn, England

2007

Tag der mündlichen Prüfung: 22.11.07

Dekan: Prof. Dr. Peter Grathwohl

1. Berichterstatter: Prof. Dr. Georg Teutsch

2. Berichterstatter: Prof. Dr.-Ing. Olaf Kolditz

Herausgeber: Institut für Geowissenschaften der Universität Tübingen
Sigwartstraße 10, D-72076 Tübingen

Schriftleitung der Reihe C: Zentrum für Angewandte Geowissenschaften (ZAG)
Lehrstuhl für Angewandte Geologie

Prof. Dr. Thomas Aigner
Prof. Dr. Erwin Appel
Prof. Dr. Peter Grathwohl
Prof. Dr. Stefan Haderlein
Prof. Dr.-Ing. Olaf Kolditz
Prof. Dr. Georg Teutsch

Redaktion: Dipl.-Geol. Björn Sack-Kühner

ISSN 0935-4948 (Print)
ISSN 1610-4706 (Internet)

Acknowledgements

This work was funded by the German Ministry of Education and Research (BMBF) under grant 02WN0352 as a part of the KORA priority program, sub-project 1.2 and additional funding from the Brandenburgische Boden Gesellschaft für Grundstücksverwaltung und –verwertung mbH (BBG).

I would like to thank Georg Teutsch, who as supervisor and employer provided not just help and advice where needed, but also regular paycheques. Special thanks are due to Anita Peter for her continuous support and advice in all aspects of this work.

I would also like to thank the two Ulis (Maier and Mayer) for their help and suggestions relating to MIN3P. For all their help with CompFlow and multiphase flow simulations I would like to thank Rudy Maji and Ed Sudicky. Thanks also to Olaf Kolditz, Thomas Kalbacher and others in the RockFlow/Geosys development group for their help, input and extensive “user support” for the Brand flow model.

Last but not least to those without whom I wouldn’t have made it this far. Thanks.

Abstract Contamination of the subsurface by LNAPLs (Light Non-Aqueous Phase Liquids), particularly fuel hydrocarbons, is a widespread problem threatening groundwater quality at affected sites. Monitored natural attenuation (MNA) is increasingly used in site management strategies in such cases as an alternative to, or in conjunction with conventional remediation measures. For the implementation of MNA at a contaminated site, contaminant emission, transport and degradation processes need to be understood and quantified and a prognosis made for the likely future development of the contamination, especially with regard to the spatial and temporal stationarity of the contaminant plume. In this respect, mathematical models describing the relevant physical processes have come to play a central role in the investigation of contaminated sites. For the field-scale simulation of MNA-relevant processes, existing model codes offer manifold possibilities in terms of model complexity and process representation. The choice of modelling approach is site- and problem-specific, taking into consideration the site data available and the questions to be addressed (i.e. the processes of interest); there is no “one-size-fits-all” solution.

Three kerosene contaminated sites, which are broadly similar in terms of geology and contamination history, but differ in terms of scale, the quantity and distribution of kerosene in the subsurface and the data available from site investigations, are presented as case studies demonstrating different innovative modelling approaches for investigating MNA-relevant processes. The modelling approaches in each case consider different processes to address different questions of relevance for the implementation of MNA.

The three cases studies serve to highlight some important points for consideration in modelling LNAPL contaminated sites, as well as demonstrating how the modelling approach used can influence the model outcome. It is shown that in terms of the source zone geometry only the lateral extent is of significance for contaminant emission; the vertical extent and the NAPL distribution, as well as the source mass are of little relevance for contaminant emission. More important are hydrogeological and hydrological conditions, particularly groundwater flow velocity and recharge rates. Groundwater recharge is shown to be one of the most important parameters to consider for large area LNAPL contaminations. On the one hand it plays a significant role in contaminant emission, while on the other hand as a source of electron acceptors it can be a key determining factor for contaminant degradation. Comparing the case studies it can be seen how the processes considered in the modelling approach can affect the model outcome; where a simple first-order kinetic representation of biodegradation results in a steady state contaminant distribution, a more complex approach considering aqueous and solid phase electron acceptors can result in a transient situation.

Kurzfassung Die Verunreinigung des Untergrunds durch LNAPLs (Light Non-Aqueous Phase Liquids), insbesondere Kohlenwasserstoff-Kraftstoffe, ist ein weit verbreitetes Problem, das eine Bedrohung für die Grundwasserqualität an betroffenen Standorten darstellt. Die Überwachung natürlicher Schadstoffminderung (Monitored Natural Attenuation - MNA) wird in solchen Fällen zunehmend bei den Altlastenbearbeitungsstrategien verwendet – als Alternative zu oder in Verbindung mit herkömmlichen Sanierungsmaßnahmen. Für die Implementierung von MNA an einem verunreinigten Standort müssen Schadstoffemissionen, Transport und Abbauprozesse verstanden und quantitativ bestimmt werden, damit eine Prognose über die wahrscheinliche zukünftige Entwicklung der Verschmutzungssituation, besonders hinsichtlich der räumlichen und zeitlichen Stationarität der Schadstofffahne, erstellt werden kann. Mathematische Modelle, welche die relevanten physikalischen Prozesse beschreiben, spielen dabei mittlerweile eine zentrale Rolle. Für die Simulation der MNA-relevanten Prozesse im Feldmaßstab bieten vorhandene Modellcodes vielfältige Möglichkeiten hinsichtlich der Erfassung der Komplexität und der Prozessdarstellung. Die Wahl des Modellverfahrens ist standort- und problemspezifisch und erfolgt auf der Basis vorhandener Standortdaten und der zu untersuchenden Fragestellung (d.h. des zu untersuchenden physikalischen Prozesses). Dabei gibt es keine einheitliche Lösung, die auf alle Fälle anwendbar ist.

Drei mit Kerosin verschmutzte Standorte, die von geologischen Gegebenheiten und Schadensfall her ähnlich sind, die sich jedoch hinsichtlich Größenordnung, Menge und Verteilung des Kerosins im Untergrund sowie der erhobenen Daten aus Standortuntersuchungen unterscheiden, werden als Fallstudien vorgelegt. Diese stellen unterschiedliche innovative Modellverfahren zur Untersuchung MNA-relevanter Prozesse dar. Die in den jeweiligen Verfahren betrachteten unterschiedlichen Prozesse verfolgen unterschiedliche Fragestellungen, die relevant sind für die Implementierung von MNA.

Die drei Fallstudien dienen dazu, wichtige Gesichtspunkte hervorzuheben, die bei der Modellierung von LNAPL Standorten zu betrachten sind. Sie erlauben auch Aussagen darüber zu treffen, inwieweit das verwendete Modellverfahren das Endergebnis beeinflussen kann. Es wird gezeigt, dass bezüglich der Schadensherdgeometrie nur die laterale Ausdehnung für die Schadstoffemission von Bedeutung ist; die vertikale Ausdehnung und die Verteilung der NAPL Sättigungen sowie die gesamte Schadstoffmasse sind hingegen weniger relevant. Wichtiger sind hydrogeologische- und hydrologische Gegebenheiten, insbesondere die Grundwasserfließgeschwindigkeit und –neubildungsrate. Es stellt sich heraus, dass vor allem die Grundwasserneubildung einen der wichtigsten Parameter bei der Betrachtung

großflächiger LNAPL Schadensfälle darstellt. Die Grundwasserneubildung spielt einerseits eine bedeutende Rolle bei der Schadstoffemission. Sie kann aber anderseits auch als Quelle für Elektronenakzeptoren ein Schlüsselfaktor für den Schadstoffabbau sein. Anhand der vergleichenden Fallstudien kann gezeigt werden, wie die Prozesse, die bei der Modellierung betrachtet werden, das Ergebnis beeinflussen können: Dort wo eine einfache 1.Ordnung Kinetik des Bioabbaus zu einer stationären Schadstofffahne führt, kann ein komplexeres Verfahren, welches sowohl wässrige als auch mineralische Elektronenakzeptoren betrachtet, zu einer instationären Schadstofffahne führen.

1. Introduction

Contamination of the subsurface by LNAPLs (Light Non-Aqueous Phase Liquids), particularly fuel hydrocarbons, is a widespread problem threatening groundwater quality at affected sites. Monitored natural attenuation (MNA) is increasingly used in site management strategies in such cases as an alternative to, or in conjunction with conventional remediation measures.

The exact definition of monitored natural attenuation accepted by the legislative authorities varies depending on the country in question, but in principal most are similar to that developed by the United States Environmental Protection Agency, which defines MNA as the “reliance on natural attenuation processes (within the context of a carefully controlled and monitored site cleanup approach) to achieve site-specific remediation objectives within a time frame that is reasonable compared to that offered by other more active methods. The 'natural attenuation processes' that are at work in such a remediation approach include a variety of physical, chemical, or biological processes that, under favorable conditions, act without human intervention to reduce the mass, toxicity, mobility, volume, or concentration of contaminants in soil or groundwater. These in-situ processes include biodegradation; dispersion; dilution; sorption; volatilization; radioactive decay; and chemical or biological stabilization, transformation, or destruction of contaminants." (USEPA, 1999).

For the implementation of MNA at a contaminated site, contaminant emission, transport and degradation processes need to be understood and quantified and a prognosis made for the likely future development of the contamination, especially with regard to the spatial and temporal stationarity of the contaminant plume. In this respect, mathematical models describing the relevant physical processes have come to play a central role in the investigation of contaminated sites, with guidelines set by regulatory authorities for the assessment of MNA explicitly including the requirement for mathematical models in a quantitative or predictive role (LABO, 2005; UKEA, 2000; USEPA, 1999).

The last two decades have seen rapid advances in the modelling of subsurface environments, with constant advances in terms of site investigation and data collection, process understanding, the mathematical and computational methods required to represent the processes and the computational power available. However, mathematical models by their very nature are, and will always be, incomplete representations of the natural systems that they simulate, necessarily relying on limited input data and simplifying assumptions.

This does not undermine their role as predictive or interpretive tools, indeed their usefulness lies in the fact that they offer a possibility to understand and visualise processes and make predictions based on limited data, but in applying such models it is important to bear in mind the assumptions and limitations of the approach used, which may have significant bearing on the results obtained.

For the field-scale simulation of NA-relevant processes, existing model codes offer manifold possibilities in terms of complexity and process representation. The choice of modelling approach is site and problem-specific; there is no “one-size-fits-all” solution. Starting with a conceptual model for the site, the numerical modelling approach should take into consideration the site data available and the questions to be addressed (i.e. the processes of interest), as well as further considerations such as time and financial constraints.

This work presents different modelling approaches used to investigate NA-relevant processes in the form of three case studies for kerosene contaminated sites studied within the German KORA (Retention and Degradation Processes Reducing Contaminants in Groundwater and Soil) funding priority. The sites are broadly similar in terms of history, geological characteristics and contaminants, but differ in terms of scale, the quantity and distribution of kerosene in the subsurface and the data available from site investigations. The modelling approaches for the three sites reflect these differences and in each case consider different processes to address different questions relevant to the overall assessment of NA. Innovative methods are used in the application of the models, which are in each case applied with both quantitative and interpretative aims in mind, i.e. both for quantification of processes (e.g. contaminant emission or degradation rates) and for process understanding (identification of important parameters and relationships). Furthermore, applying the different approaches to three essentially similar problems allows some comparison of the approaches in terms of the results obtained.

Figure 1.1 shows a conceptualisation of the three sites considered here. All three are former tankfarms at decommisioned military airfields where the unsaturated zone and capillary fringe of a sandy-silty aquifer is contaminated with kerosene jet fuel. For the purposes of the study, the sites can be considered as representing three categories or “types” of LNAPL contamination, which could broadly be used to classify most cases of LNAPL contamination in a sand or gravel aquifer.

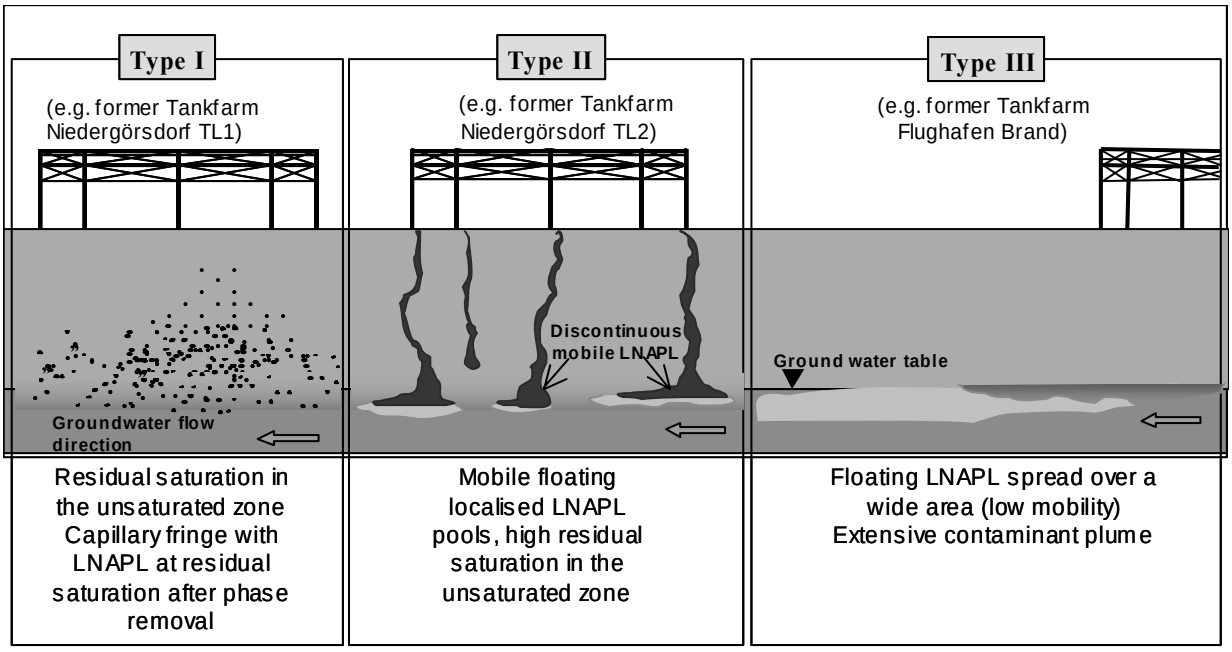

Figure 1.1 Conceptualisation of the three categories of LNAPL contamination considered in the case studies.

The first category, Type I, is a situation with immobile LNAPL at low residual saturation in the unsaturated zone and capillary fringe, for which the field site Niedergörsdorf Tanklager 1 (TL1) is used as an example. In the modelling study a chemically complex but geometrically simple representation of the kerosene source zone is used to investigate the emission of contaminants to the aqueous and gaseous phases in a model including both the saturated and unsaturated zones with simple geological heterogeneity. A basic first-order kinetic approach is applied for the degradation of contaminants, and a sensitivity analysis is carried out to determine the influence of various estimated parameters on the contaminant emission and aqueous phase plume lengths.

The second category, Type II, considers LNAPL at high saturations in the unsaturated zone forming mobile pools on the groundwater surface, for which the field site Niedergörsdorf Tanklager 2 (TL2) is used as an example. A multiphase modelling approach is applied to simulate the development of complex source zones and study contaminant emission for multiple realisations of statistically generated geological heterogeneity.

The third category, Type III, considers a situation with a large-area LNAPL pool with minimal mobility and an extensive and well-established downstream contaminant plume, for which the field site Flughafen Brand is used as an example. A detailed geological and hydrogeological model is developed for the site and used as a basis for a reactive transport

modelling study to investigate in detail the contaminant degradation processes in the plume and develop a prognosis for MNA at the site.

2. LNAPLs in the subsurface: Relevant concepts and governing equations

The common theme linking the three case studies presented in this work is that they all involve a complex organic LNAPL mixture, kerosene, which has been spilled over a period of time at the ground surface resulting in the contamination of a sandy-silty aquifer. Figure 2.1 shows a conceptualisation of such a spill, generally applicable to the cases studied here. Following a spill at the surface, the NAPL entering the ground will travel downwards through the unsaturated zone, with a portion remaining trapped in the pore volume of the material through which it passes until, if the volume spilled is sufficient, it reaches the capillary fringe where it begins to spread laterally. In the unsaturated zone a three phase NAPL-water-gas system develops in the pore volume of the sediment, while further down the soil column in the saturated zone a two-phase NAPL-water system develops. Dissolution and volatilisation of the NAPL in the pore spaces together with physical transport processes results in contaminant plumes spreading out from the source area in the aqueous and gas phases. The contaminants thus released may be subject to various processes leading to a reduction in their concentration or that hinder their further spreading, including dispersive processes, sorption on the aquifer matrix and microbially mediated degradation reactions.

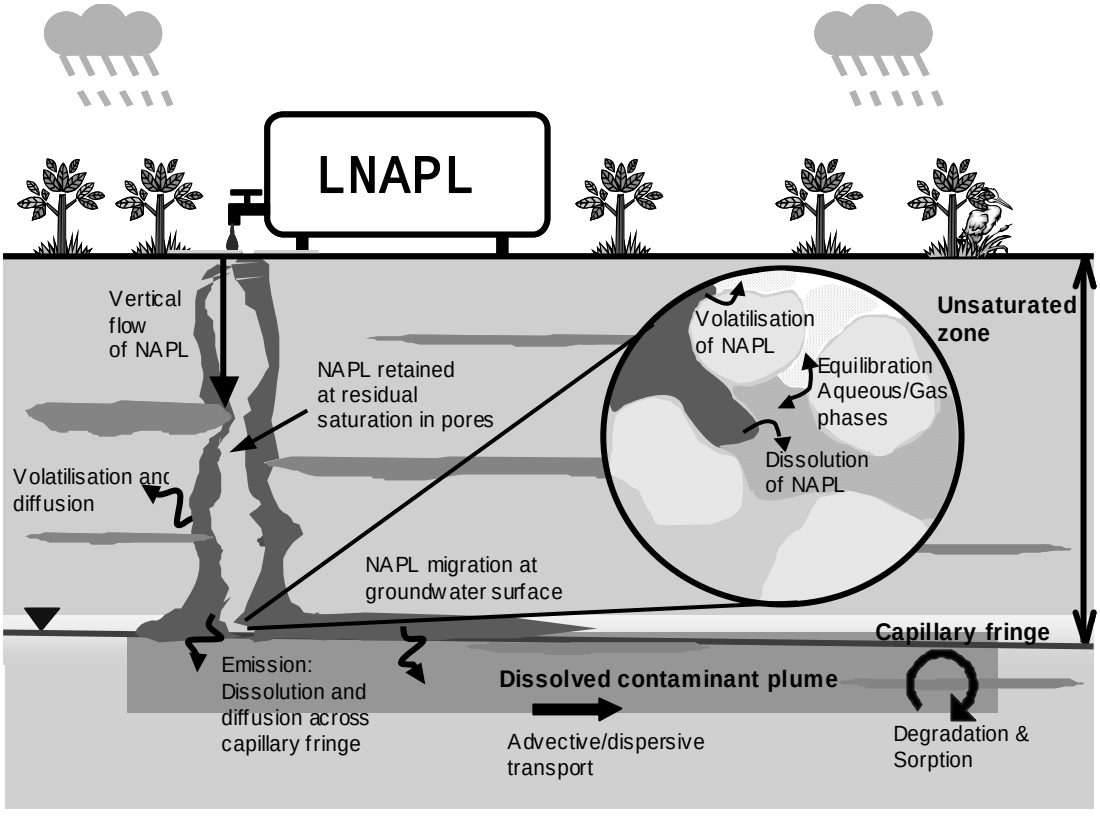

Figure 2.1 Conceptualisation of an LNAPL spill scenario in a sandy aquifer

The following sections summarise concepts, physical processes and relationships relevant to the case studies presented in this work.

2.1. Distribution of fluid phases in the soil column

The unsaturated or vadose zone refers to the region between the ground surface and the ground water table, which defines the boundary between the unsaturated and saturated zones. In this region the volumetric water content of the soil, or degree of saturation, varies over the soil column. Figure 2.2(a) shows a static water saturation profile between ground surface and saturated zone for a 20m column with the groundwater table at z = 5m. In the upper region the water in the pore volume is held at a minimum, residual saturation. The magnitude of the residual saturation depends on the soil in question; different soils have different water retention characteristics, with the capillary forces holding water in the soil structure determined by a number of factors such as grain size, porosity, electrolytes etc. In the capillary fringe, adjacent to the groundwater table the aqueous saturation increases, reaching unity at the groundwater table, which defines the boundary between the two-phase water-gas system of the unsaturated zone and the single-phase system of the saturated zone. Figure 2.2(b) shows the saturation profiles for the same sand column after an LNAPL has been introduced at the ground surface and migrated vertically to the groundwater table. The unsaturated zone is now a three-phase NAPL-water-gas system with both NAPL and water held at residual saturations in the upper region. At the capillary fringe this gives way to a two-phase NAPL-water system and below this is a single-phase system of water only.

For the two-phase water-gas system that exists in the unsaturated zone before the introduction of the NAPL phase, the change in water saturation, S_q with height above the groundwater table can be described as a function of the height above the groundwater table. The air-water capillary pressure head, h_{aw}, is defined by

$$h_{aw} = \frac{P_a}{\rho_w g} - \frac{P_w}{\rho_w g} \qquad (2.1)$$

where P_a and P_w are the air and water capillary pressures respectively, ρ_w is the density of water and g the gravitational acceleration constant. In the unsaturated zone P_w is negative. h_{aw} is related to hydraulic head, H by

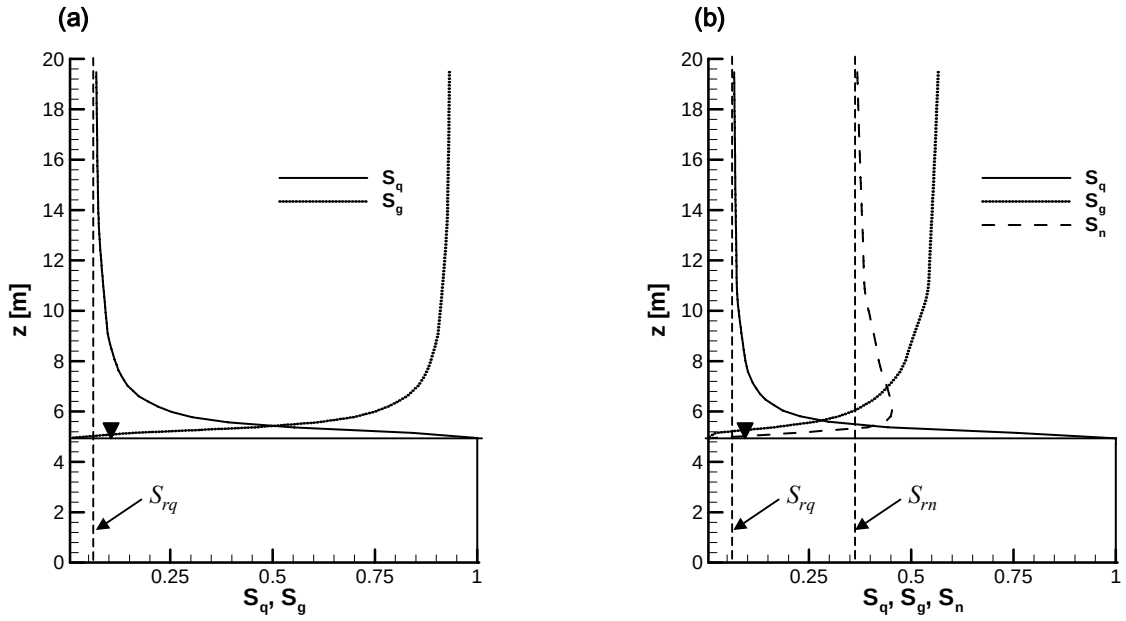

Figure 2.2 Saturation profiles for a sand column with the groundwater table at *z = 5m* and upper surface at *z = 20m*. S_q, S_g and S_n are the water, gas and NAPL saturations, while S_{rq} and S_{rn} denote the residual water and NAPL saturations. (a) Saturation profile with water only (b) Saturation profile after infiltration of LNAPL at the upper surface.

$$H = -h_{aw} + z \tag{2.2}$$

where z defines an elevation above a datum. Taking the elevation of the groundwater table as the datum, h_{aw} will increase with increasing height above the groundwater table. The functional relationship between h_{aw} and the volumetric water content S_q for a given soil can be described by a relationship such as that of Van Genuchten (1980):

$$S_q = S_{rq} + (1 - S_{rq})\left[1 + (\alpha h_{aw})^n\right]^{-m} \tag{2.3}$$

where S_{rq} is the residual aqueous saturation for the soil and α, n and $m=1-1/n$ (with units [-], [-], [L^3/L] respectively) are soil dependent parameters, the so-called van Genuchten parameters.

For the three-phase system that exists in the unsaturated zone after the addition of a NAPL, the capillary pressure relationships can be described using two-phase data for the different fluid pairs (Leverett, 1941). Capillary pressure curves for the two-phase oil-water and oil-gas fluid pairs can be estimated from the air-water curve by scaling factors, β_{nq} and β_{an}, determined from the interfacial tensions between the fluids (Parker and Lenhard, 1987), defined as $\beta_{nq}=\sigma_{aq}/\sigma_{nq}$ and $\beta_{an}=\sigma_{aq}/\sigma_{an}$ where σ_{ij} is the interfacial tension between phases i and j and the indices a, n, and q denote air, oil and water respectively.

2.2. Multi-phase fluid flow

Groundwater flow in a saturated medium can be described by Darcy's Law:

$$\upsilon_i = -K_{ij}^{w} \frac{\partial H}{\partial x_j} \qquad i, j = x, y, z \tag{2.4}$$

where υ_i is the Darcy flux vector, K^{w}_{ij} is the hydraulic conductivity tensor of water and H is the hydraulic head. This relationship can also be written in terms of fluid pressure:

$$\upsilon_i = -\frac{K_{ij}}{\mu_q}\left(\frac{\partial P_q}{\partial x_j} - \rho_q g \frac{\partial Z}{\partial x_j}\right) \qquad i, j = x, y, z \tag{2.5}$$

where K_{ij} is the intrinsic permeability of the porous medium, P_q is the water pressure in the groundwater, ρ_q and μ_q are the mass density and viscosity of water, g the gravitational constant and Z the depth.

Where more than one fluid phase is present in a porous media (i.e., gas and aqueous or gas, aqueous and NAPL phases in the unsaturated zone, or aqueous and NAPL phases in the saturated zone), each fluid phase interferes with the flow of the others. A fluid at its residual saturation is immobilised and does not flow at all. The reduction in mobility of a phase, l, in a multiphase system is described by multiplying the intrinsic permeability of the porous medium by a dimensionless relative permeability, k_{rl}, for the phase. Thus for the flow of phase l in a multiphase system,

$$\upsilon_i = -\frac{K_{ij} k_{rl}}{\mu_q}\left(\frac{\partial P_q}{\partial x_j} - \rho_q g \frac{\partial Z}{\partial x_j}\right) \qquad i, j = x, y, z \tag{2.6}$$

As with capillary pressures, three-phase relative permeability data are difficult to obtain directly and are usually based on an empirical extrapolation of two phase data for fluid pairs, e.g. (Stone, 1973):

$$k_{rn} = k^{*}_{rnq}\left[\left(\frac{k_{rnq}}{k^{*}_{rnq}} + k_{rq}\right)\left(\frac{k_{rng}}{k^{*}_{rnq}} + k_{rg}\right) - \left(k_{rq} + k_{rg}\right)\right] \tag{2.7}$$

where k^{*}_{rnq} is the relative permeability of NAPL at the residual saturation of water in the water-NAPL system, k_{rnq} is the relative permeability of NAPL in the water-NAPL system as a function of water saturation S_q, k_{rng} is the relative permeability of NAPL in the gas-NAPL system as a function of gas saturation S_g.

2.3. Contaminant emission

Emission of contaminants from an LNAPL source in the unsaturated zone results from mass transfer processes between the non-aqueous and aqueous phases (dissolution) and the aqueous, non-aqueous and gas phases (volatilization).

2.3.1. Dissolution of NAPL mixtures

For a complex organic mixture such as kerosene, the solubility of a single substance from the non-aqueous phase is a function of its individual aqueous solubility and mole fraction in the mixture, described by Raoult's law:

$$C_{w_i} = \chi_i \gamma_i C_{w_i}^{sat} \tag{2.8}$$

where C_{w_i} is the aqueous solubility of component i from the mixture, χ_i is the mole fraction of component i in the mixture, γ_i is the activity coefficient of i in the mixture (generally = 1) and $C_{w_i}^{sat}$ is the (liquid subcooled) aqueous solubility of pure compound i.

For the dissolution of a complex organic mixture such as kerosene, mass fluxes of individual components from the mixture, and respectively the composition of the mixture in terms of mole fractions of components, will change over time. As the mass fluxes of individual components to the aqueous phase are dependent on their solubility and their mole fraction in the mixture, components with high solubility or accounting for a large fraction of the mixture will show high mass fluxes at first, decreasing as their mole fraction in the mixture decreases. This decrease will lead to an increase in the mole fractions of compounds with lower solubility, which in turn will show increasing mass fluxes.

At low groundwater flow velocities and under homogeneous conditions, NAPL dissolution can generally be considered as an instantaneous equilibrium process, while at higher flow velocities or in heterogeneous media, kinetically controlled dissolution may be observed (Khachikian and Harmon, 2000; Mayer and Miller, 1996; Seagren and Moore, 2003). The dissolution rate can be described for example by:

$$R_{c_{nq}} = \phi M_q S_q \kappa_{c_{nq}} (X_{cq}^* - X_{cq}) \tag{2.9}$$

where Φ is the porosity, S_q is the water saturation in the pore volume, M_q is the molar density of water, κ_{cnq} is the forward dissolution rate for the contaminant from the non-aqueous to the aqueous phase, X_{cq} is the mole fraction of contaminant in the aqueous phase and X^*_{cq} is the mole fraction of contaminant in the aqueous phase in equilibrium with the

non-aqueous phase (Unger et al., 1998). One formulation for the forward rate dissolution rate parameter κ_{cnq} is (Berglund, 1997; Guiguer and Frind, 1994):

$$\kappa_{c_{nq}} = \lambda_R S_n^{\beta_2} \tag{2.10}$$

where λ_R is the forward dissolution rate constant for contaminant transfer from the non-aqueous to the aqueous-phase and β_2 is a parameter associated with the forward dissolution rate of the contaminant.

2.3.2. Volatilization from NAPL mixtures

There are two potential paths for the transfer of mass from the NAPL phase to the gas phase; direct volatilisation of the NAPL phase or via dissolution and partitioning between the aqueous and gas phase. The former is analogous to the dissolution process described by Raoult's law, where the saturated gas phase concentration, C_{g_i}, takes the place of the aqueous solubility C_{w_i}. The saturated gas phase concentration due to volatilisation is given by

$$C_{g_i} = \frac{MW_i}{RT} VP_i \tag{2.11}$$

where Mw_i is the molecular weight of component i, VP_i is the saturation vapour pressure of component i, R is the universal gas constant (8.314 J/molK) and T is the absolute temperature.

In the latter case, following dissolution partitioning between the aqueous and gas phases is determined by the Henry constant, K_H:

$$C_{g_i} = K_{H_i} C_{w_i} \tag{2.12}$$

In a 3-phase NAPL-water-gas system under equilibrium conditions, the gas phase concentration of a component, i, will be independent of the path.

2.4. Transport processes

The main transport processes of interest considering contaminants emitted from an immobile LNAPL distributed in both the saturated and unsaturated zones are advective-dispersive transport in the aqueous phase and diffusive transport in the gas phase.

2.4.1. Advective-dispersive transport

Advective transport, where contaminants are carried by the bulk movement of groundwater, is the principal process involved in contaminant migration in the aqueous phase. The advective transport velocity for a conservative compound is derived from the Darcy equation (Eqn. 2.4), by dividing the Darcy velocity by the effective porosity, n_e:

$$v_i = -\frac{K_{ij}^w}{n_e}\frac{\partial H}{\partial x_j} \qquad i, j = x, y, z \tag{2.13}$$

One-dimensional advective transport for flow in the x direction with velocity v_x is described by:

$$\frac{\partial C}{\partial t} = -v_x \frac{\partial C}{\partial X} \tag{2.14}$$

where C is the contaminant concentration, t is time and x is the distance along the flow path. Purely advective transport according to Equation 2.14 would result in a sharp concentration front moving downstream from a contaminant source. Hydrodynamic dispersion creates a zone of mixing at the advective plume front and results in a spreading of the advective front with distance from the source and contaminants migrating further than would be expected by advection alone. Hydrodynamic dispersion is a combination of two distinct processes; mechanical dispersion, a mixing process caused by local variations around the mean flow velocity in non-ideal media and molecular diffusion. Other than at extremely low groundwater flow velocities, mechanical dispersion is the dominant process, and hence the contribution of molecular diffusion may often be neglected (Domenico and Schwartz, 1990). Including dispersivity in the one-dimensional advective transport equation, Equation 2.14 becomes

$$\frac{\partial C}{\partial t} = D_x \frac{\partial^2 C}{\partial x^2} - v_x \frac{\partial C}{\partial X} \tag{2.15}$$

where D_x is the hydrodynamic dispersion coefficient (L^2/T).

2.4.2. Diffusive transport

Diffusive transport in the aqueous or gaseous phase is driven by concentration gradients; movement occurs from areas of higher concentration to areas of lower concentration. The resulting mass flux in one dimension under steady-state conditions can be expressed by Fick's first law:

$$F = -D\left(\frac{dC}{dx}\right) \tag{2.16}$$

where F is the mass flux of substance per unit time, D is the diffusion coefficient and dC/dx expresses the concentration gradient. If the concentration of the diffusing substance is time dependent Fick's second law applies, which, again for one dimension, is

$$\frac{\partial C}{\partial t} = D\frac{\partial^2 C}{\partial x^2} \tag{2.17}$$

where $\partial C/\partial t$ expresses the change in concentration with time.

The diffusion coefficient, D [L^2/T], is a property of the diffusing substance which may either be determined experimentally or calculated using empirical relationships. For example the Fuller-Schettler-Giddings (FSG) method for gas phase diffusion (Fuller et al., 1966):

$$D_g = \frac{0.001T^{1.75}\left[\frac{1}{m_g} + \frac{1}{MW}\right]^{0.5}}{P\left[V_g^{1/3} + V^{1/3}\right]^2} \tag{2.18}$$

where T is the temperature [K], P is the pressure [atm], m_g the molar weight of air [g/mol], V the molar volume of air (20.1 cm^3/mol at 1 atm, 20°C), V_g the molar volume of diffusing substance [cm^3/mol], MW the molar weight of diffusing substance [g/mol], or for aqueous diffusion (Worch, 1993):

$$D_{aq} = \frac{3.595\times10^{-7}T}{\eta_q MW^{0.53}} \tag{2.19}$$

where η_q is the dynamic viscosity of water (1.306 cP at 10 °C [$\times 10^3$ Nsm^{-2}]). Aqueous diffusion coefficients are typically in 4 or 5 orders of magnitude lower than their gaseous counterparts (Sleep and Sykes, 1989).

A diffusing substance in porous media must travel greater distances than in an unrestricted environment as it follows a non-linear path around mineral grains. This is accounted for by use of an effective diffusion coefficient, D_{eff}, which is related to D by a tortuosity factor, τ:

$$D_{eff} = \tau D \tag{2.20}$$

The tortuosity factor reflects the extended travel paths for diffusing substances in porous media and can be determined from diffusion experiments or estimated from empirical relationships, e.g. (Millington and Quirk, 1961)

$$\tau_l = \frac{(nS_l)^{7/3}}{n^2} \tag{2.21}$$

where n is the porosity of the medium and S_l the degree of saturation of phase l.

2.5. Sorption

Sorption is the process by which dissolved species partition from the aqueous phase (groundwater) to a solid phase (the aquifer matrix). This reversible reaction can lead to reduced aqueous phase contaminant concentrations and a retardation (slowing) of the spreading of a contaminant plume, or conversely a re-release of sorbed contaminants (desorption) if the aqueous phase concentration falls. As different compounds sorb to different degrees, in a plume containing multiple contaminants sorption may lead to differential retardation analogous to chromatographic separation. The partitioning of a contaminant between the aqueous phase and the aquifer matrix is commonly expressed in terms of the distribution coefficient, K_d, defined as the ratio of the sorbed concentration C_s to the aqueous phase concentration C_{aq}:

$$K_d = \frac{C_s}{C_{aq}} \tag{2.22}$$

Principally responsible for sorption are organic material (carbon) and clay minerals present in the aquifer matrix. In most quaternary aquifers however it is the carbon fraction that controls the sorption of organic contaminants. The value of K_d for a contaminant can be estimated from the mass fraction of organic carbon in the aquifer matrix, f_{oc} and the partitioning coefficient for the contaminant between octanol and water, K_{ow}:

$$K_{oc} = \frac{K_d}{f_{oc}} \tag{2.23}$$

with K_{oc} related to K_{ow} by an empirical relationship such as (Karickhoff et al., 1979):

$$K_{oc} = 0.62 K_{ow} \tag{2.24}$$

Sorption isotherms are models that describe the degree of sorption for different contaminant concentrations, for example the Freundlich isotherm which is expressed as

$$C_s = K_d C_{aq}^{1/n} \quad (2.25)$$

where n is a chemical-specific parameter, with $1/n$ typically between 0.7 and 1.1. If $n = 1$, Equation 2.25 reduces to the linear isotherm, $C_s = K_d C_{aq}$, which is valid for dissolved species at concentrations less of than half of their solubility, making it generally applicable for contaminants partitioning from fuel mixtures (Lyman et al., 1992).

The retardation of a contaminant with respect to the advective transport velocity v_x can be expressed as the ratio of v_x to the average velocity of the contaminant, v_c giving the Retardation Factor, R:

$$R = \frac{v_x}{v_c} \quad (2.26)$$

while R (assuming linear sorption) can be determined from K_d according to:

$$R = 1 + \frac{\rho_b K_d}{n} \quad (2.27)$$

where n is porosity and ρ_b the aquifer bulk density. Including retardation in the one-dimensional advective transport equation, Equation 2.15 becomes

$$R\frac{\partial C}{\partial t} = D_x \frac{\partial^2 C}{\partial x^2} - v_x \frac{\partial C}{\partial X} \quad (2.28)$$

2.6. Biodegradation

Biodegradation generally refers to the breakdown of a substance by living organisms. In the context of a hydrocarbon contaminated aquifer it refers to the breakdown of the organic contaminants by microorganisms. Biodegradation processes have been identified for a wide range of organic contaminants and vary widely in terms of the microorganisms responsible, degradation pathways, intermediate compounds and mechanisms (Wiedemeier et al., 1999).

2.6.1. Degradation processes for fuel hydrocarbons

In the case of fuel hydrocarbons, the dissolved contaminants are ultimately transformed into carbon dioxide, water and methane via a series of oxidation-reduction (redox) reactions. The driving force for the reactions is the transfer of electrons from an electron donor (hydrocarbon) to an electron acceptor, releasing energy that can be utilised by microorganisms for growth and reproduction. This can be summed up in a generalised equation (Wiedemeier et al., 1999):

microorganisms + electron donor + electron acceptor → metabolic by-products + energy + microorganisms

The electron acceptors typically available in a groundwater environment are oxygen, nitrate, Fe(III) (in the form of minerals), sulfate and carbon dioxide, while the metabolic by-products of fuel hydrocarbon degradation typically include carbon dioxide, water, nitrite or nitrogen gas, Fe(II) (aqueous ions), hydrogen sulfide and methane. The energy released by the transfer of electrons from donor to acceptor is quantified thermodynamically by the Gibbs free energy of the reaction, ΔG_r, where

$$\Delta G_r^\circ = \sum \Delta G_{f,products}^\circ - \sum \Delta G_{f,reactants}^\circ \qquad (2.29)$$

with ΔG_r° the Gibbs free energy of the reaction for standard state and $G_{f,products}^\circ$ and $\Delta G_{f,reactants}^\circ$ the Gibbs free energy of formation for the reaction products and reactants respectively. A negative value for ΔG_r° indicates an exothermic reaction, i.e. one releasing energy that can be utilised by microorganisms, which from the point of view of the microorganisms is a pre-requisite for the reaction to take place. For the oxidation of a given electron donor, the value of ΔG_r° for the reaction depends on the electron acceptor utilised (often referred to as the Terminal Electron Acceptor Process or TEAP). When multiple TEAPs are available, the reactions occur in order of their respective energy yields with the thermodynamically most favourable TEAPs utilised first (Stumm and Morgan, 1981).

Figure 2.3 shows the common TEAPs in order of decreasing energy yield, i.e. from most favourable to least favourable. Aerobic respiration, with dissolved oxygen as electron

	TEAP	Electron acceptor	
Aerobic	Aerobic respiration	O_2	 Decreasing energy yield
Anaerobic	Denitrification	NO_3^-	
	Iron reduction	$Fe(OH)_3$	
	Sulfate reduction	SO_4^{2-}	
	Methanogenesis	CO_2	

Figure 2.3 Common TEAPs ordered by decreasing energy yield

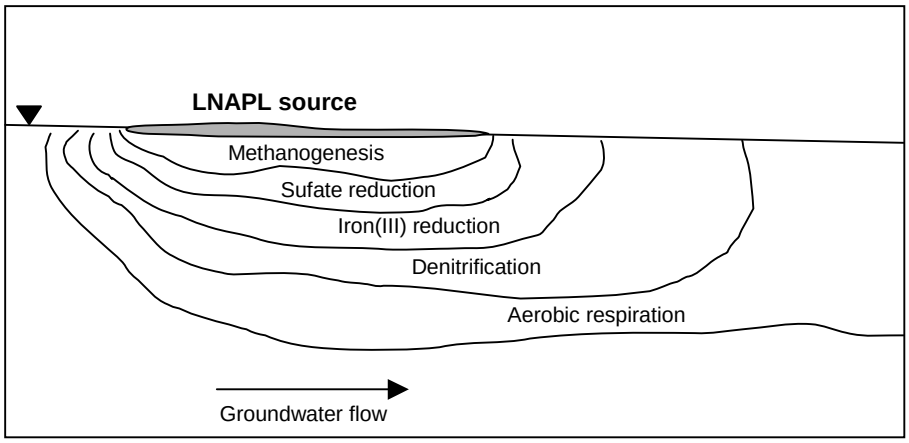

Figure 2.4 Conceptualization of dominant TEAP zones for an LNAPL contamination. Adapted from Lovley et al. (1994)

acceptor occurs first, followed by the anaerobic processes, nitrate, Fe(III) and sulfate reduction, and finally methanogenesis.

2.6.2. Distribution of TEAPs in a contaminated aquifer

This sequential utilisation of electron acceptors leads to the spatial and temporal zonation of TEAPs in a contaminated aquifer, generally referred to as redox zonation.

Figure 2.4 shows an idealized conceptualization of the redox zonation resulting from an LNAPL contamination. In the vicinity of the source zone where dissolved contaminant concentrations and fluxes are highest, the thermodynamically preferred electron acceptors are depleted and methanogenesis and sulfate reduction are the dominant TEAPs. Moving downstream, in the zone where Fe(III) is still present but NO_3 and O_2 are depleted, iron reduction is the dominant TEAP, while towards the fringes of the contaminant plume denitrification and aerobic respiration become dominant. In reality the redox zonation at a field site may be less clear cut and can deviate significantly from the ideal case. The dominant TEAPs can change temporally and spatially due to changing water levels and recharge fluxes affecting the availability of electron acceptors, while the different degradation processes may occur concurrently throughout the plume.

2.6.3. Biodegradation kinetics

The rates at which biodegradation reactions occur in groundwater are principally a function of the availability of electron donors and acceptors. The kinetics of the reactions can be described by mathematical functions, or kinetic models. Two models commonly used to describe the biodegradation of organic compounds in groundwater, and which have been

applied in the case studies presented in this work are Power law models and Monod kinetics.

2.6.3.1.Power law kinetic models

A power law kinetic model takes the form

$$\frac{\partial C}{\partial t} = -kC^n \tag{2.30}$$

where C is the concentration of the reacting species, t is time, k is the rate of decrease, or degradation rate constant for the species and the exponent n is the order of the reaction. Two forms of the power law are commonly applied to biodegradation kinetics. In first-order kinetics, where $n = 1$, Equation 2.30 becomes

$$\frac{\partial C}{\partial t} = -kC \tag{2.31}$$

and the rate of reaction is proportional to the concentration of the reacting species. In zero-order kinetics, where $n = 0$, Equation 2.30 becomes

$$\frac{\partial C}{\partial t} = -k \tag{2.32}$$

and the rate of reaction is constant, independent of the concentration of reacting species.

First-order kinetics are often implemented to model biodegradation by applying them as a simple decay term for degrading species with the degradation rate k used as a calibration parameter.

2.6.3.2. Monod kinetic model

The Monod kinetic model (Monod, 1942) is a hyperbolic function describing microbial growth rate, μ as a function of substrate concentration, C:

$$\mu = \mu_{\max} \frac{C}{k_c + C} \tag{2.33}$$

where μ and $\mu_{\max}$ are the growth rate and maximum growth rate (1/time) and k_c is the half-saturation constant. At very low or high substrate concentrations, the function reduces to a power law approximation; when $C << k_c$ Equation 2.33 becomes

$$\mu = \frac{\mu_{\max}}{k_c} C \tag{2.34}$$

and the reaction approaches first-order kinetics, while for $C >> k_c$ Equation 2.33 becomes

$$\mu = \mu_{\max} \tag{2.35}$$

and the reaction approaches zero-order kinetics.

The rate of substrate utilisation (contaminant degradation) is related to μ by a yield coefficient, Y which is a measure of the organisms formed per substrate used:

$$\frac{\partial C}{\partial t} = \mu_{\max} \frac{MC}{Y(k_c + C)} \tag{2.36}$$

where M is the microbial mass (mg/l). In groundwater modelling studies it is commonly assumed that the proportional change in the microbial population in response to the contaminant concentrations is negligible (Simkins and Alexander, 1984). In this case Equation 2.36 becomes

$$\frac{\partial C}{\partial t} = k \frac{C}{(k_c + C)} \tag{2.37}$$

with $k = \mu_{\max} \cdot M_0$, where M_0 is the initial microbial mass.

2.7. Contaminant plume behaviour

The preceding sections summarise processes involved in the development of a dissolved contaminant plume emanating from a source zone and spreading downstream. If the boundary of the plume is defined by the isoline of a given concentration, on the one hand emission from the source and transport processes drive the growth of the plume, while on the other hand degradation, sorption and dilution act to hinder the growth. The behaviour of a plume can broadly be defined by one of three types; growing, steady-state and shrinking. These are illustrated in Figure 2.5. In a growing plume, the driving forces, i.e. the emission and transport of contaminants from the source, outstrip the processes hindering the growth, i.e. degradation, sorption and dilution and the isoline defining the plume boundary will move downstream away from the source. This is typical of the initial stages of the plume development following the contaminant spill. In a steady-state plume the emission and transport processes are in equilibrium with the degradation, sorption and dilution processes

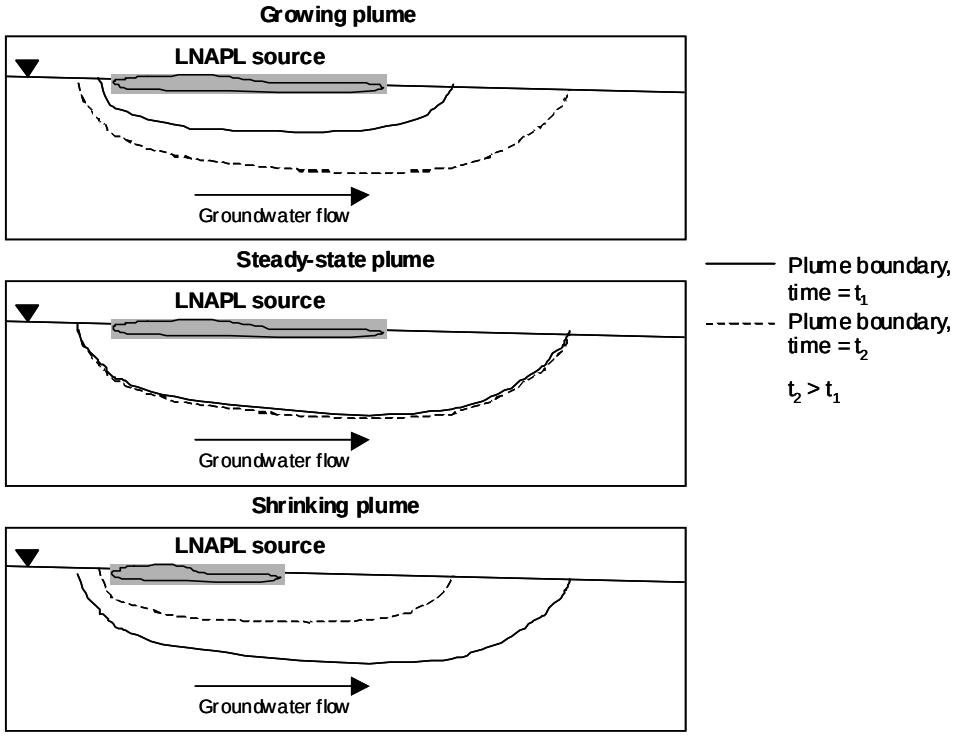

Figure 2.5 Conceptualization of the three types of plume behaviour; growing, steady-state and shrinking.

and the isoline defining the plume boundary is stationary. In a shrinking plume the degradation, sorption and dilution outstrip the emission and transport from the source, and the isoline defining the plume boundary moves upstream towards the source. This is typical of a situation where the contaminant source is depleted or has been removed.

3. Case Study 1: Niedergörsdorf Tanklager 1

3.1. Introduction

Niedergörsdorf Tanklager 1 (TL1) represents an example of a Type 1 LNAPL contamination in terms of the contamination type definitions used for this study (see Section 1), with a historical LNAPL spill at the ground surface, and LNAPL contamination at low residual saturations in the unsaturated zone and capillary fringe. The overall aim of the numerical modelling at TL1 was to estimate and characterise the emission from the source zone to both the gaseous and aqueous phases and to assess the potential development of contaminant plumes in the saturated and unsaturated zones, as well as to develop a prognosis for the implementation of MNA at the site. Of particular interest were the temporal evolution of the contaminant emission, i.e. the change in contaminant emission over time as the LNAPL composition changes, contaminant plume development, i.e. the prognosis for steady state and maximum plume lengths for contaminants of varying degradability, and the potential lifetime of the contaminant source. Additionally, the modelling was intended to address a more general problem associated with the assessment and field scale modelling of contaminated sites. With all field sites the spatial density of measurements and sampling points is generally low due to financial and practical considerations and field data has inherent uncertainties arising from sampling and analysis. Accordingly, numerous assumptions are made and estimated or averaged values are used for parameters where data is not directly available. The modelling at TL1 was intended to assess the potential effects of uncertainties in field data and the use of estimated and averaged values in models for the assessment of this type of contaminated site.

To consider contaminant emission and transport in both the aqueous and gas phases, a two-dimensional variably-saturated reactive transport model was developed for the site using the MIN3P model code (Mayer et al., 2002). The emission of multiple contaminants with temporal evolution of the LNAPL source composition was considered by defining an LNAPL source with finite mass with dissolution according to Raoult's law (see Section 2.3). A constituent averaging technique was applied to simplify the source composition (Gaganis et al., 2002). Biodegradation of contaminants was represented using a simple first-order decay approach (see Section 2.6.3). This is one of the most widely used approaches for simulating degradation of organic hydrocarbons in groundwater (Wiedemeier et al., 1999). The advantage of applying this approach as opposed to a more sophisticated kinetic

model such as Monod kinetics was that first-order degradation rates can be estimated directly from field data. The consideration of electron acceptors and the role of different TEAPs in the contaminant degradation, which are not accounted for in the first-order kinetic model, were beyond the scope of the work at TL1.

Multiple scenarios were simulated to determine the influence of various parameters on both the emission of contaminants from the source zone and the subsequent plume development. This is of importance in developing a prognosis for the site, as well as being of interest to identify parameters of importance both for sites of this type and the modelling approach used here.

3.2. Site description

Flughafen Niedergörsdorf is a disused military airfield located approximately 60km southwest of Berlin, Germany. The site, which has been used for various military purposes since the 1800's, was operated as an airfield by the Russian military from 1945 until the German Reunification at the beginning of the 1990's. The airfield, shown in Figure 3.1(a), consists of a main runway running approximately East-West and number of buildings and constructions, now mostly derelict, relating to its former use; hangars, parking areas, shelters etc. There are five former tank farms (Tanklager) around the site. Tanklager 1 (TL1), shown in Figure 3.1(b), is located at the western end of the main runway. The site covers approximately 2.5 hectares and consists of an open area, where the above-ground fuel storage tanks, and a bunker construction, which housed pumping machinery. A number of investigations have been carried out at TL1 over the last ten years, with periodic monitoring of groundwater levels and concentrations of contaminants and electron acceptors. In addition to 18 existing conventional monitoring wells, TL1-1 – TL1-18, a number of multilevel groundwater and soil gas monitoring wells were installed during an intensive Geoprobe direct push campaign conducted during 2003 to further characterise the site and contamination.

The subsurface in the area of TL1 is extensively contaminated with the kerosene fuel that was stored and handled there. In March 2003 the measured kerosene phase thickness in monitoring wells at the site ranged between 3 cm and 60 cm, from which the extent of the kerosene phase in the capillary fringe can be estimated (see Figure 3.1(b)).

(a)

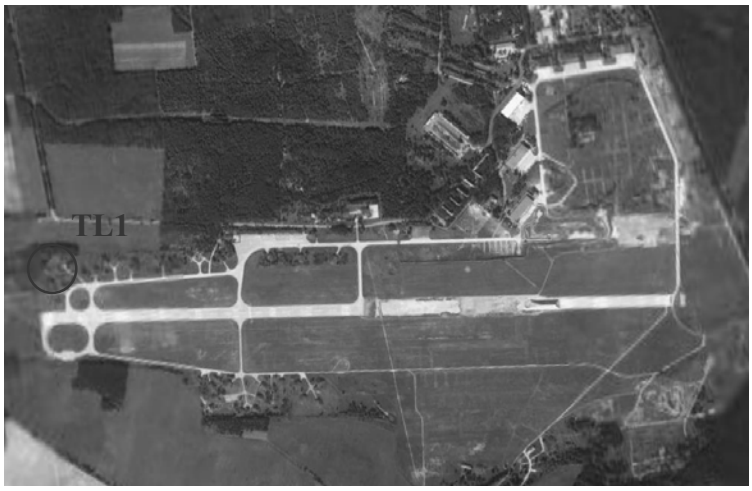

(b)

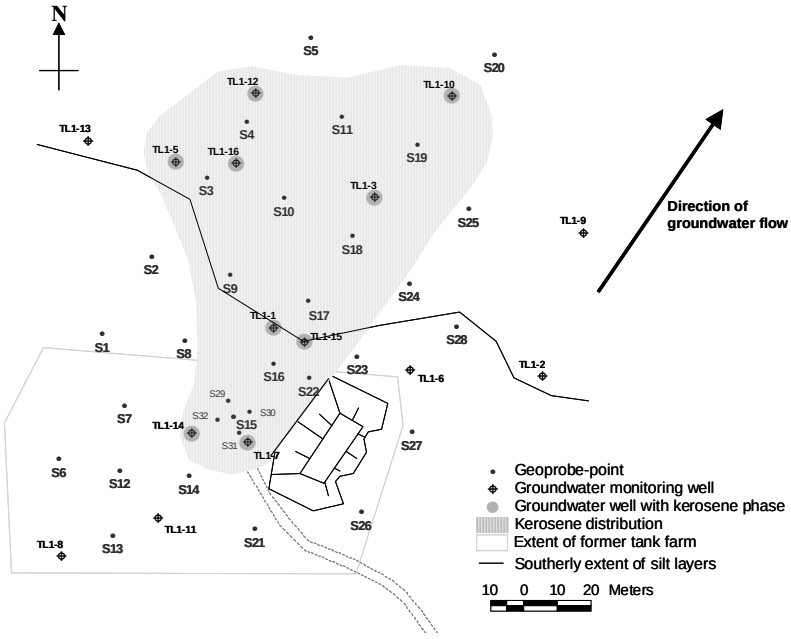

Figure 3.1 (a) Flughafen Niedergörsdorf (b) Tanklager 1, showing locations of existing boreholes, geoprobe points, the approximate southerly extent of silt lenses and the estimated area of kerosene contamination

The site lies in a heathland area known as Heinrichsdorfer Heide, with an elevation of 93m asl. at the southern end of the site increasing gradually to 108m in the north. The geology of the area is typical of the Fläming-Waldhügelland in which it is located, with cohesive and non-cohesive soils overlying older marl and sand deposits. At a local scale the geological profile consists predominantly of fine to coarse sands of moderate to high hydraulic conductivity containing lenses of low conductivity silt, clay and marl ranging in thickness from a few decimetres to several meters. Climatically, the area is subject to a continental

type climate with a fairly low annual precipitation in the order of 550 mm/yr, with monthly averages highest in July and August at 61mm and lowest in January and February at 35mm[1].

From existing drilling logs and electrical conductivity soundings carried out during the geoprobe campaign, the soil profile beneath TL1 is known to consist mainly of fine to medium sands with silt lenses of varying thickness in the unsaturated zone in the northern part of the site. The approximate southerly extent of the silt layers can be seen in Figure 3.1(b). The groundwater surface at TL1 is typically about 20m below ground level, with groundwater flow in an approximately north-easterly direction.

3.3.Model description and governing equations

The numerical modelling code MIN3P (Mayer et al., 2002) is a generalised mechanistic multi-dimensional, multi-component reactive transport model for variably saturated media. Figure 3.2 shows a conceptualisation of the physico-chemical system in MIN3P, where the aqueous and gaseous phases are considered as mobile and the solid phase immobile. The aqueous phase consists of organic and inorganic dissolved species and the solvent water, the gaseous phase of atmospheric and other gases including organic compounds in the gas phase. The solid phase consists of minerals, amorphous phases, surface species and organic matter. Operationally, NAPLs are treated as a part of the solid phase, i.e. immobile, and their dissolution as a mineral dissolution process, which as such may be kinetically controlled. The dissolution of solid phase components and gas exchange between the aqueous and gaseous phases are regarded as heterogeneous reactions, i.e. reactions resulting in inter-phase mass transfer (homogeneous reactions would be those taking place within a single phase, for example redox or hydrolysis reactions in the aqueous phase). These contribute to internal source-sink terms describing increase or decrease of a particular constituent within a Representative Elementary Volume (REV), represented in Figure 3.2 as $Q^{s,s}$, $Q^{s,a}$, $Q^{a,a}$ and $Q^{a,g}$, where the indices s, a and g denote the solid, aqueous and gaseous phases respectively. The external source and sink terms (shown as $Q^{a,in}$, $Q^{a,out}$, $Q^{g,in}$ and $Q^{g,out}$) arise from physical transport of components into and out of the REV by advection, dispersion, diffusion etc. Reactions, kinetic parameters and component properties are defined in external databases, which can be edited to tailor the model to specific problems. The conceptual model is described by two sets of governing equations, one for groundwater

[1] Average values 1985-2002, Wetterstation Jänickendorf, www.jaenickendorf-wetter.de

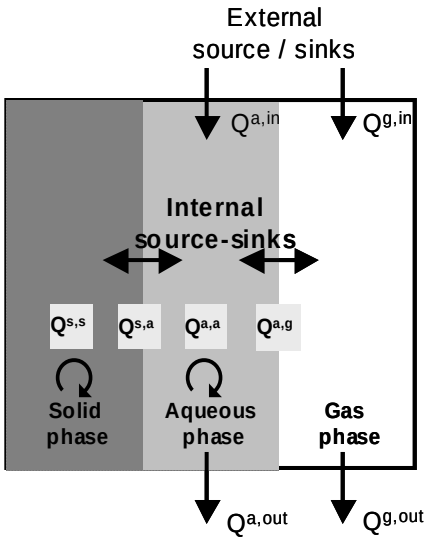

Figure 3.2 Conceptualisation of three-phase system in Min3P. Adapted from Mayer et al. (2002)

flow in variably saturated media, the other for reactive transport in variably saturated media. The former is described by the Richard's equation and van Genuchten soil hydraulic functions. The latter is based on a global implicit solution method with substitution of primary variables.

A generalized formulation is used for intra-aqueous biogeochemical reactions. The reaction formulation allows the reaction progress to depend on the total aqueous concentrations and/or activities of any number of dissolved species. Any reaction order can be accommodated with respect to any of the species. Monod and inhibition terms expressed as functions of total aqueous concentrations are also included and can be used to describe microbially mediated reactions, or applied to activate or deactivate reactions in response to changing geochemical conditions. The rate expression is given by (Mayer et al., 2002):

$$R_k^a = -k_k^a \underbrace{\left[\underbrace{\prod_{\substack{j=1 \\ o_{kj}^{at} \neq 0}}^{N_c} \left(T_j^a\right)^{o_{kj}^{at}}}_{\text{fractional order } T_j^a} \underbrace{\prod_{\substack{j=1 \\ o_{kj}^{at} \neq 0}}^{N_c} \left(\gamma_j^c C_j^c\right)^{o_{kj}^{ac}}}_{\text{fractional order } C_j^c} \underbrace{\prod_{\substack{j=1 \\ o_{kj}^{at} \neq 0}}^{N_c} \left(\gamma_j^x C_j^x\right)^{o_{kj}^{ax}}}_{\text{fractional order } C_j^x} \underbrace{\prod_{\substack{j=1 \\ o_{kj}^{at} \neq 0}}^{N_c} \frac{T_j^a}{K_{kj}^{a,mo} + T_j^a}}_{\text{Monod } T_j^a} \underbrace{\prod_{\substack{j=1 \\ o_{kj}^{at} \neq 0}}^{N_c} \frac{K_{kj}^{a,in}}{K_{kj}^{a,in} + T_j^a}}_{\text{inhibition } T_j^a} \right]}_{} \underbrace{\left[1 - \frac{IAP_k^a}{K_k^a}\right]}_{\text{affinity term}} \quad (3.1)$$

k_k^a is the rate constant for the aqueous phase kinetic reaction (denoted by the indices *a* and *k*), to which any of the other multiplicative terms may be applied in defining a reaction scheme for N_c components. The three fractional order terms are for the total aqueous component concentration T_j^a, aqueous species concentration C_j^c and aqueous complex concentration C_j^x for the *j*th component, with activity coefficients γ_j^c and γ_j^x for the aqueous

species and complexes respectively. o_{kj}^{at}, o_{kj}^{ac} and o_{kj}^{ax} define the reaction orders with respect to the total aqueous component, species and complex concentrations, respectively. In the Monod and inhibition terms $K_{kj}^{a,mo}$ defines the Monod half saturation constant, while $K_{kj}^{a,in}$ is an inhibition constant. Bacterial growth and die-off are not included in the kinetic formulation. The affinity term, where IAP_k^a is the ion activity product of the reaction and K_a^k the equilibrium constant, can be excluded to define an irreversible reaction.

An analogous generalised expression is used to describe surface-controlled mineral dissolution-precipitation reactions (Mayer et al., 2002):

$$R_k^{ms} = -S_i k_k^m \left[\underbrace{\prod_{\substack{j=1 \\ o_{kj}^{mt}\neq 0}}^{N_c} \left(T_j^a\right)^{o_{kj}^{mt}}}_{\text{fractionalorder } T_j^a} \underbrace{\prod_{\substack{j=1 \\ o_{kj}^{mc}\neq 0}}^{N_c} \left(\gamma_j^c C_j^c\right)^{o_{kj}^{mc}}}_{\text{fractionalorder } C_j^c} \underbrace{\prod_{\substack{j=1 \\ o_{kj}^{mx}\neq 0}}^{N_c} \left(\gamma_j^x C_j^x\right)^{o_{kj}^{mx}}}_{\text{fractionalorder } C_j^x} \underbrace{\prod_{\substack{j=1 \\ o_{kj}^{m,mo}>0}}^{N_c} \frac{T_j^a}{K_{kj}^{m,mo}+T_j^a}}_{\text{Monod } T_j^a} \underbrace{\prod_{\substack{j=1 \\ o_{kj}^{m,in}>0}}^{N_c} \frac{K_{kj}^{m,in}}{K_{kj}^{m,in}+T_j^a}}_{\text{inhibition } T_j^a} \right] \underbrace{\left[1-\frac{IAP_k^m}{K_k^m}\right]}_{\text{affinity term}} \quad (3.2)$$

where R_k^{ms} [mol dm^{-3} porous medium s^{-1}] is the reaction rate for the k^{th} reaction, S_i the reactive surface area of the mineral phase [m² mineral dm^{-3} porous medium] and k_k^m the rate constant for the dissolution of the mineral. The remaining parameters are analogous to those in Equation 1, with the index *m* denoting the mineral phase.

Linear sorption of aqueous phase components is included in MIN3P as a non-kinetic equilibrium according to a distribution coefficient, K_d, and thus in the model is implicitly assumed to occur equally in all aquifer materials.

The equation systems are solved by Newton iteration, with locally mass-conservative finite volume spatial discretisation. For temporal discretisation, fully implicit time weighting is used. A comprehensive description of the theoretical development of the model is given in Mayer et al. (2002).

3.4. Model setup

A two-dimensional multiphase, multi-component reactive transport approach with steady state flow was developed based on a 200m long transect of the site. A number of scenarios were created based on this transect in order to test the effects of uncertainties associated with the field data and the use of estimated or averaged parameters for the site.

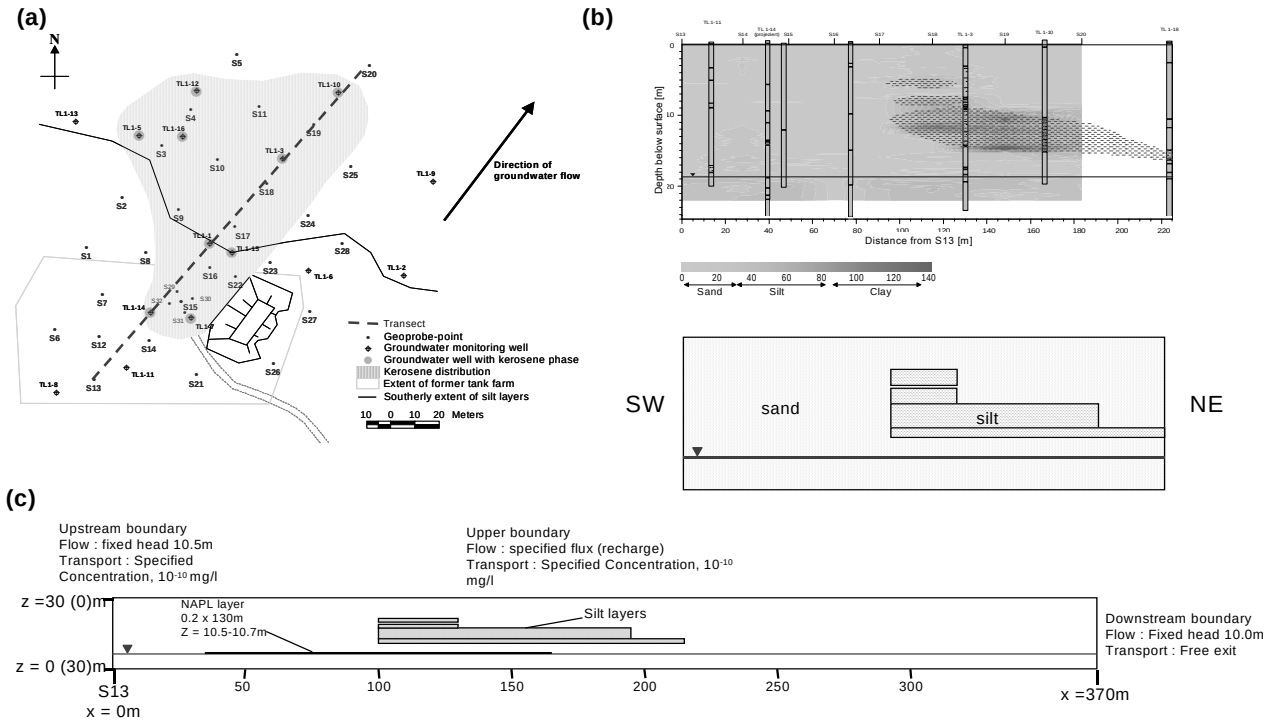

Figure 3.3 Development of the model domain (a) sitemap showing the location of the transect (b) interpretation of electrical conductivity data to showing positions of silt lenses and representation of the lenses as rectangular features in the model domain (c) schematic of 2D model domain

3.4.1. Development of the model domain

The model domain was created based on a transect running parallel to the estimated groundwater flow direction from south-west to north-east across TL1 between points S13 and S20 (see Figure 3.3(a)). A geological interpretation for the transect based on direct-push resistivity profiles is shown in Figure 3.3(b). The profile is mainly sandy material, with significant silt lenses occurring in the unsaturated zone towards the northern end. The transect geology is reduced to two material types in the model, sand and silt, with homogeneity assumed within both sediment types. The major silt lenses identified in the geological interpretation are approximated by rectangular forms in the model domain (Figure 3.3(b)). Physical parameters assigned for the sand and silt in the model were estimated from grain size distribution curves for a number of samples of each material type from the site using the code SOILPROP (ESTI, 1990a). The values used in the model are averages for the material types.

Two sets of boundary conditions were applied to the model, the first for variably saturated flow, the second for reactive transport. For the variably saturated flow model, fixed head (Dirichlet) conditions were set at the upstream and downstream boundaries and a specified

flux (Neumann) condition was set at the upper boundary for infiltration of groundwater recharge. No condition was specified for the lower boundary, making it no flow by default. Hydraulic heads of 10.5m and 10.0m were assigned to the upstream and downstream boundaries respectively, resulting in a hydraulic gradient of 0.0014 across the domain. This represents an average value for the transect, while the corresponding thickness of the unsaturated zone, 19.5 – 20m, in the domain is also typical of the situation at TL1. Flux across the upper boundary was specified according to the total annual recharge, estimated to be 120mm/yr based on the 50 year average data for the area. Constant recharge was assumed in the simulations based on one-dimensional models for the site, which showed that the thickness of the unsaturated zone is sufficient to effectively damp the effects of seasonal variations (Miles, 2003). Boundary conditions for reactive transport were fixed concentration (Dirichlet) for the upper and upstream boundary, with concentrations of 1×10^{-10} mg/l for all species, and a free exit condition (Neumann) for the downstream boundary.

Table 3.1 General parameter values used in the model

General parameters		
Domain dimensions	370m × 30m	
Simulation time, Δt_{max}, Δt_{min}	18,250 days, 30 days, 1×10^{-10} days	
Aqueous diffusion coefficient, D_{aq} [m^2s^{-1}]	5.9×10^{-10} (1)	
Gaseous diffusion coefficient, D_g [m^2s^{-1}]	3.1×10^{-6} (1)	
Dispersivity (longitudinal/transverse) [m]	0.1 / 0.01 (3)	
Soil type specific parameters		
	Sand	Silt
θ_r [-]	0.133 (2)	0.146 (2)
α [1/m]	9.29 (2)	0.34 (2)
n [-]	2.81 (2)	3.62 (2)
m (1-1/n)	0.64	0.72
Air entry pressure [atm]	0	0
Porosity [-]	0.38 (2)	0.45 (2)
Hydraulic conductivity K_{xx}, K_{zz} [m/s]	1.6×10^{-4}	6.9×10^{-7}
Specific storage coefficient [-]	1×10^{-5} (3)	1×10^{-5} (3)

(1) MIN3P allows for only one diffusion coefficient in each phase. Values used are mole fraction weighted averages
(2) Average values for samples from site. Porosity determined experimentally, other values estimated using SOILPROP
(3) Assumed value

The finite volume grid for the model domain consisted of 15,600 cells (150 cells horizontally by 104 cells vertically), with local refinement horizontally in the source zone area and vertically over the source zone area and capillary fringe to cope with steep concentration and saturation gradients. Simulations were run for a period of 50 years (18,250 days), this being a reasonable length of time both with regard to the history of the site and being sufficient to observe emission behaviour and plume development. Execution time on a 2.4GHz Pentium IV PC was in the order of 12 hours.General parameters used in the model are summarized in Table 3.1.

3.4.2. Representation of the kerosene mixture and source zone

The kerosene mixture represented in the model was based on the analysis of a kerosene sample taken from borehole TL1-1. The analysis identifies 24 compounds constituting 32% of the total mixture (see Appendix). A constituent averaging technique was applied to create a number of composite components to simulate the average behaviours of groups of individual compounds (Gaganis et al., 2002; Miles, 2003). In applying this technique, components are grouped together using a physico-chemical property as grouping criteria and bulk properties are then calculated for the composite as mass fraction weighted averages of the individual components. This reduces the complexity and computational demands of the modelling task while retaining the multi-component properties of the mixture. Aqueous solubility was used as the grouping criteria, which is suggested by Gaganis et al. (2002) as being the best parameter to use in order to minimise errors arising from changes in the average properties of the composite as the mole fractions of its constituents change over time. To represent the large undefined fraction of the kerosene, an additional component was created with physical properties assigned as the mole fraction weighted average of the defined compounds. The composition of the simplified kerosene mixture is given in Table 3.2. Compounds that were to be treated as degradable in the simulations were defined as individual components in the mixture.

Theoretical vertical distributions of LNAPL in the pore volume of the source zone were calculated using the method described by Huntley & Beckett (Huntley and Beckett, 2002). Assuming a vertical equilibrium, an extension of the van Genuchten soil capillarity equations (Van Genuchten, 1980) is used to combine the observed NAPL phase thickness in a monitoring well with the physical properties of the NAPL and soil capillary properties in the adjacent porous media in order to calculate the NAPL distribution in the formation (see also Section 2.1). The thickness of the NAPL phase measured in monitoring wells at the site

Table 3.2 Composition and physico-chemical properties for the simulated kerosene mixture

Composite components		Mole fraction in kerosene [-]	Solubility [mol/l]	Henry constant K_H [-]
Group1	n-Pentadecane n-Tetradecane n-Dodecane n-Tridecane n-Undecane	0.095	3.4×10^{-8}	1.5×10^{2}
Group2	n-Decane n-Nonane n-Octane	0.132	8.9×10^{-7}	1.7×10^{2}
Group3	Methylnaphthalene Naphthalene n-Propylbenzene 2-Ethyltoluene 3/4-Ethyltoluene	0.032	5.4×10^{-4}	2.0×10^{-1}
Group4	1,3,5-TMB 1,2,3-TMB 1,2,4,5-TMB	0.017	4.2×10^{-4}	2.8×10^{-1}
Unknown	Undefined fraction	0.684	5.6×10^{-4}	1.2×10^{2}
Individual components				
Isopropylbenzene		0.002	4.2×10^{-4}	4.6×10^{-1}
1,2,4-TMB		0.02	4.7×10^{-4}	2.8×10^{-1}
Ethylbenzene		0.004	1.4×10^{-3}	2.7×10^{-1}
m/p-Xylene		0.01	1.5×10^{-3}	2.6×10^{-1}
o-Xylene		0.004	2.1×10^{-3}	1.6×10^{-1}
Toluene		0.00013	6.0×10^{-3}	2.4×10^{-1}

in March 2003 and the estimated physical properties for the medium sand found in the source zone were used in the calculation. In attempting to reproduce the distribution in the model domain, it was found that to have different NAPL saturations in adjacent modelcells led to numerical difficulties, and so an average and saturation over the thickness of the source zone was used. In fact this is a reasonable assumption, as the above-mentioned method of Huntley and Beckett assumes a stable vertical equilibrium in the capillary fringe, whereas it is likely in reality that the source zone has been “smeared” by water table fluctuations (Huntley and Beckett, 2002). From the average observed thickness of free phase NAPL in monitoring wells at TL1 of 0.17m, and the estimated soil parameters for the medium sand in the NAPL contaminated area, a thickness of 0.2 m was used for the source zone with a residual NAPL saturation in the pore volume of 0.1. The lower boundary of the source zone is positioned at $z = 10.5m$, just at the top of the capillary fringe. Based on the estimated extent of the kerosene distribution in the unsaturated zone along the transect (see Figure 3.3(a)), the source zone in the model domain is 130m in length, from $x = 35m$ to $x = 165m$.

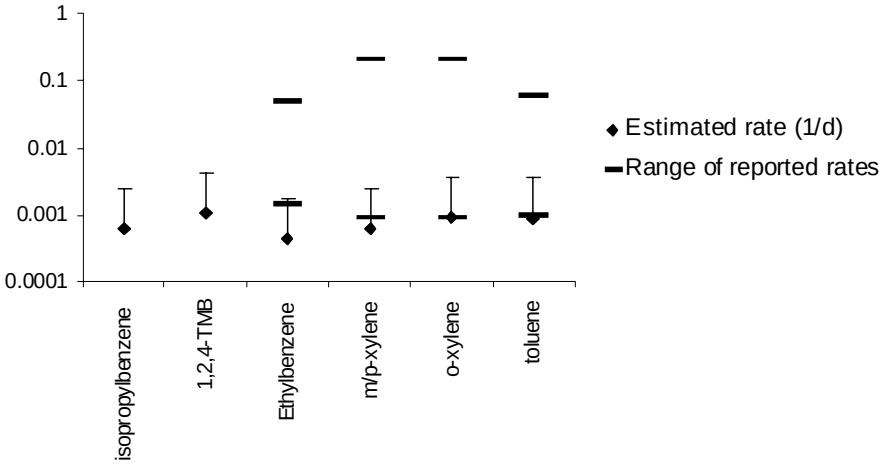

Figure 3.4 Estimated first order degradation rates for TL1 with reported literature rates (Rifai et al. 1995; Aronson and Howard, 1997)

Instantaneous equilibrium was assumed for the LNAPL dissolution, an assumption that is generally considered valid for low groundwater flow velocities such as those at TL1. This assumption is discussed by Kachikian and Harmon (Khachikian and Harmon, 2000), who summarise the work of a number of other authors, while based on experimental data, Seagren and Moore (Seagren and Moore, 2003) concluded that the local equilibrium assumption is reasonable at pore water velocities of less than 10m/day, which is the case at TL1.

Biodegradation in the model was represented by first order degradation kinetics (see section 2.6.3.1). Degradation rates for components of the kerosene mixture were estimated using two different methods; the approach proposed by Wiedemeier et al. (Wiedemeier et al., 1996), whereby the decrease in concentration of a compound measured along the plume is compared to that of a compound assumed to be recalcitrant to biodegradation, for which they suggest 1,2,3- or 1,3,5-TMB, and that of Buscheck and Alcantar (Buscheck and Alcantar, 1995) in which a regression method is applied to derive a first order degradation rate. Degradation rates calculated in this way represent an overall estimate for aerobic and anaerobic conditions, and generally have an advantage over laboratory determined data in that they incorporate the site specific environmental conditions (Wiedemeier et al., 1999). Rates were calculated using both methods for BTEX compounds and alkylbenzenes for which concentration data were available. The average of the two calculated rates for each compound was then used in the model. The estimated rates are shown in Figure 3.4, with error bars covering the range of possible values for the site based on the uncertainty in the estimated flow velocity. As first order kinetics is a commonly used approach in modelling

biodegradation, there are a large number of published studies reporting estimated degradation rates for the major BTEX compounds (Rifai et al., 1995; Wiedemeier et al., 1999). Maximum and minimum overall rates (aerobic and anaerobic) from field and microcosm studies in the literature, reported by Rifai et al. are also shown in Figure 3.4. The rates estimated for TL1 are generally low compared to the typical reported rates, which vary over two to three orders of magnitude.

3.4.3. Development of scenarios

A number of variations on the basic model were simulated to test the effects different parameters of interest. In each case the parameter in question was varied while keeping all other factors unchanged as far as possible. The tested parameters fall broadly into two categories; source zone parameters (dimensions and degree of NAPL saturation), and environmental parameters (recharge, flow velocity and degradation rates). For each parameter maximum and minimum values were determined based on an uncertainty attached to the value used in the base scenario and possible values for the site, or a wider range in order to establish the nature of the relationship between parameter and model outcome. The parameter values used in the base scenario and the ranges considered are summarized in Table 3.3.

Recharge; 60 – 180 mm/yr

One-dimensional simulations for TL1 showed recharge to be an important parameter in terms of the LNAPL dissolution and mass transfer to the aqueous phase. As effectively no hydrological data are available for the site, the estimated value for recharge of 120mm/yr used in the base scenario is taken from the 50 year average value, for which an uncertainty of +/- 50% was assumed.

Flow velocity; 3 – 40 m/yr

Flow velocity would be expected to be an important parameter both for development of the aqueous phase contaminant plume and the emission from the source zone (Wiedemeier 1999). The order of magnitude range of possible flow velocities considered for TL1 reflects maximum and minimum velocities calculated between different monitoring wells at the site. As there is little uncertainty involved in the measurement of hydraulic heads and distances between monitoring wells, uncertainty in the velocities arises mainly from the uncertainty in the hydraulic conductivity and porosity values for the site. As previously mentioned, the

Table 3.3 Parameter values for the base scenario and ranges tested

Parameter		Value in base scenario	Range (min - max)
Recharge		120 mm/a	60 - 180 mm/a
Flow velocity		10 m/a	3 - 40 m/a
LNAPL saturation, S_n		0.1	0.01 - 0.25
Source zone thickness		0.2 m	0.1 - 0.7 m
Source zone length		130 m	30 - 140 m
Degradation rates	Isopropyl-benzene	7.2×10^{-9} s^{-1}	2.19×10^{-9} - 2.94×10^{-8} s^{-1}
	1,2,4-TMB	1.2×10^{-8} s^{-1}	3.69×10^{-9} - 4.96×10^{-8} s^{-1}
	Ethyl-benzene	5.2×10^{-9} s^{-1}	1.57×10^{-9} - 2.10×10^{-8} s^{-1}
	m/p-xylene	7.3×10^{-9} s^{-1}	2.22×10^{-9} - 2.98×10^{-8} s^{-1}
	o-xylene	1.1×10^{-8} s^{-1}	3.21×10^{-9} - $4.30e \times 10^{-8}$ s^{-1}
	Toluene	1.0×10^{-8} s^{-1}	3.14×10^{-9} - 4.21×10^{-8} s^{-1}

simulated flow velocities refer to the average velocity in the model domain. The most effective method of accurately controlling the steady state average flow velocity without affecting any other factors was found to be by changing the hydraulic conductivity in the x-direction, k_x. This introduced a degree of isotropy to the simulations, in the case of the minimum flow velocity resulting in a situation whereby k_x was less than k_z. Comparison with scenarios where k_z was also varied to maintain isotropy however showed no discernible differences in terms of emissions and plume development. Presumably the vertical flow component in the model is sufficiently small that minor isotropy in the hydraulic conductivities is relatively unimportant.

Source zone NAPL saturation; 0.07 – 0.25

The analytically calculated degree of NAPL saturation in the source zone is dependent on soil hydraulic properties (Huntley and Beckett, 2002), for which the values used in the model are average values determined from grain size distributions. The range of potential average saturations for the soil from the estimated hydraulic function parameters was determined using the previously described analytical method.

Source zone thickness; 0.1 – 0.7m

The maximum observed phase thickness in monitoring wells at TL1 is 0.6m, which corresponds to an estimated thickness of about 0.7m in the unsaturated zone. The minimum

value of 0.1m is the minimum that could be assigned in the model due to the grid discretisation.

Source zone length; 30 – 140m

The length of the source zone would be expected to be a parameter of importance both for the source lifetime, as it affects the overall NAPL mass, as well as the emission, affecting the surface area exposed to recharge and the groundwater/NAPL interface area. The upper limit is based on the estimated extent of the kerosene in the unsaturated zone at TL1. The lower limit does not represent the situation at the site, but was included for the investigation of the relationship between source zone length and emission / NA processes.

Degradation rates

The estimation methods used to determine the first order degradation rates for the model depend primarily on groundwater flow velocities and measured concentrations of the compounds in question, with the calculated rate being most sensitive to changes in the flow velocity. The maximum and minimum rates used in the model for each compound were those estimated using the maximum and minimum flow velocities estimated for the site.

3.5.Results and discussion

The results of the simulations are presented in the following sections. A detailed discussion of the results for the base scenario in Section 3.5.1 is followed by the results of the parameter sensitivity analyses in Section 3.5.2.

3.5.1. Base Scenario

Source zone aqueous phase concentrations

The aqueous phase concentrations in the source zone for the simulated components (with the exception of the composite component group1, made up of $C_{13} – C_{15}$ aliphatic alkanes and effectively insoluble), together with concentrations measured in laboratory column elution experiments carried out with aquifer material from the NAPL source zone at points S16 and S34 are shown in Figure 3.5. There is generally a good agreement between the concentrations in the modelled source zone and those measured in the laboratory, suggesting that, at least in terms of aqueous concentrations, the modelled source zone is a reasonable representation of the actual source zone.

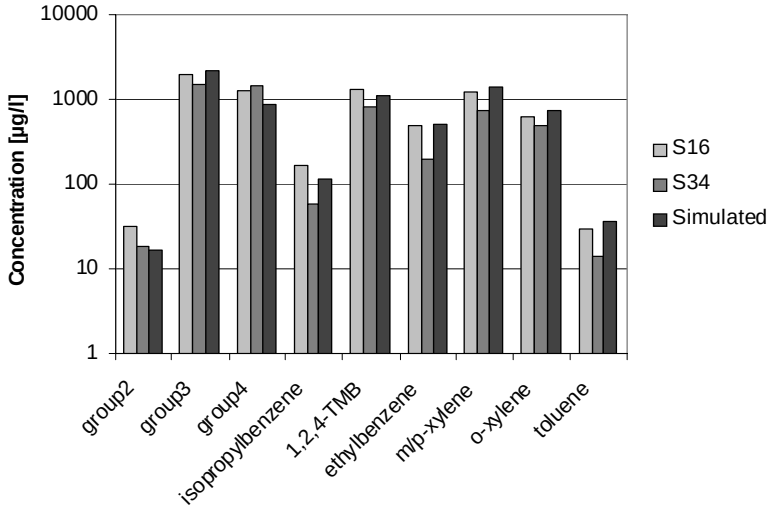

Figure 3.5 Average concentrations observed in column experiments with samples from 2 locations in the NAPL source zone at TL1 (S16 and S34) and in the source zone region of the model domain at T = 12 yrs. The composite component group1 is not included as not all of its component compounds were included in the laboratory analysis.

Mass fluxes

The release of contaminants from the NAPL source zone is an important factor to consider for the implementation of MNA at a site, being one of the principal factors determining how quickly a source will attenuate (Wiedemeier et al., 1999), as well as being important in terms of risk to receptors in the environment. In quantifying the emission from a NAPL mixture in the subsurface, as well as the total emission of different compounds of concern from the source zone, the way in which this emission is divided between the aqueous and gaseous phases is of interest, as this in turn has implications for the fate of the various compounds. Plots of the simulated mass fluxes and mass fractions for the modelled kerosene components in the base scenario are shown in Figure 3.6. In all cases the mass fluxes are high initially and drop sharply within the first half-year of the simulation, a result of the instantaneous source emplacement which results in very high concentration gradients within and around the source zone at the beginning of the simulation. Mass fluxes to the aqueous phase for the components of the kerosene mixture range over six orders of magnitude, between 10^{-1} and 10^{-7} moles/day. For the non-degrading composite components they are more or less constant after the initial high flux, as they constitute the bulk of the NAPL mass present and their mole fractions in the mixture do not change significantly during the simulation. The non-composite components (toluene, o/m/p-xylenes, ethylbenzene, 1,2,4-TMB and isopropylbenzene), which constitute only small fractions of the NAPL tend to show a decrease in flux over time as they become depleted in the mixture.

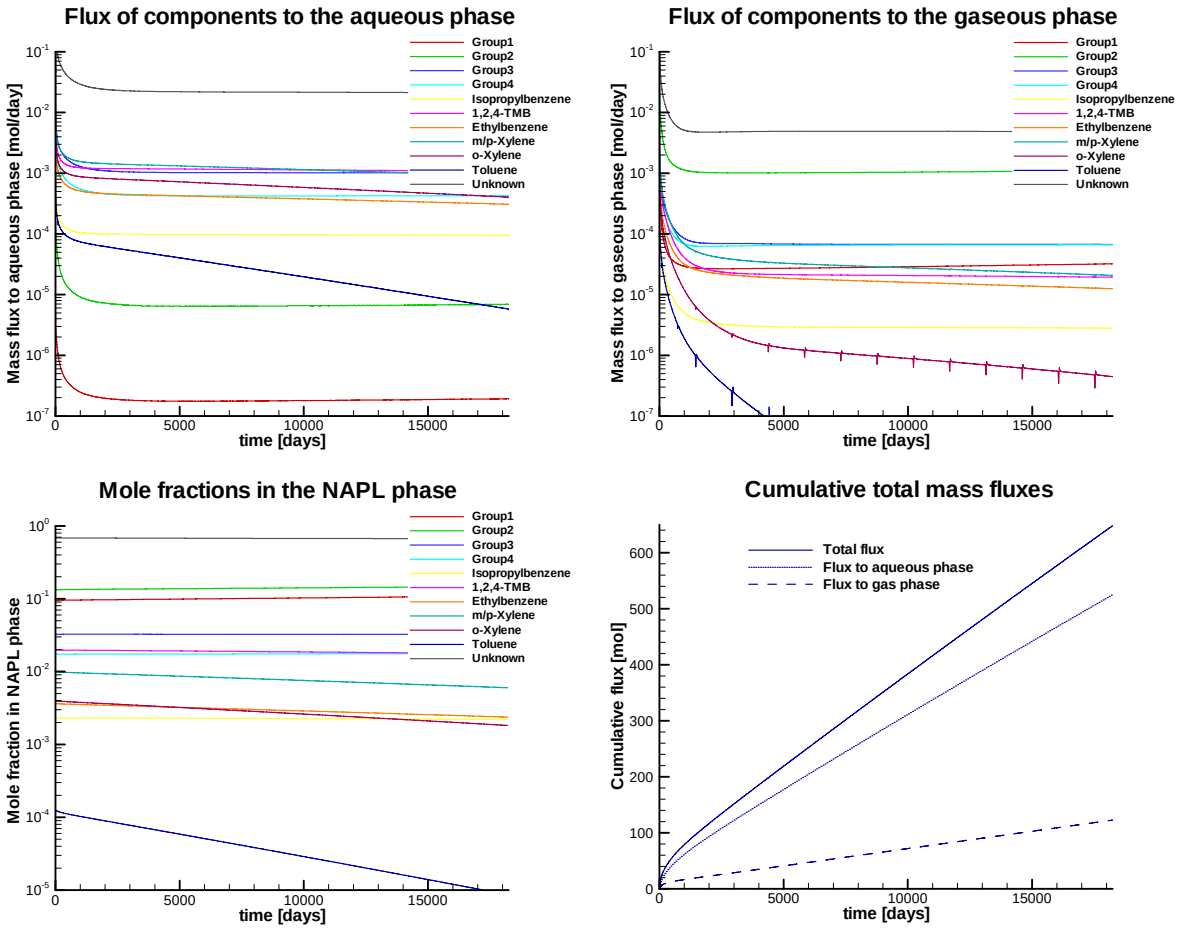

Figure 3.6 Mass fluxes to the aqueous and gaseous phases and mole fractions in the NAPL phase for the base scenario.

This is especially the case for toluene, which with a very high solubility but very low mole fraction in the mixture is rapidly depleted. The relative magnitudes of the component fluxes are much as one would expect according to Raoult's law, being influenced both by solubility and mole fraction in the mixture. The unknown fraction, with a mole fraction of 0.684 in the initial mixture and a relatively high solubility of 100 mg/l dominates the overallsituation, with a flux of approximately 0.15 mole/day, while group1, representing the $C_{11} - C_{15}$ aliphatic alkanes and as such barely soluble and representing a small fraction of the mixture (mole fraction 0.095, solubility 0.006 mg/l), the flux to the aqueous phase of 10^{-7} moles/day is almost 2 orders of magnitude lower than for any other component. Of the remaining components, most have fluxes in the range $10^{-3} – 10^{-4}$ mole/day. An exception is the composite component group2 ($C_8 – C_{10}$ aliphatic alkanes) with a flux of 10^{-5} mole/day, which having a relatively high mole fraction (0.132) might be expected to have a higher flux than, for example group3 (mole fraction 0.032). Its solubility, however, is around 500 times lower than that of group3 (0.12 mg/l cf. 66.5 mg/l) severely limiting its dissolution.

Fluxes to the gas phase show a similar pattern, dominated by the unknown fraction of the mixture and remaining fairly constant for most components after the initial period. The magnitudes of the mass fluxes to the gas phase depend on a complex interplay between a number of factors, mainly the Henry constant, K_H and mole fractions in the NAPL, as well as solubility and degradation in the aqueous phase. The composite components group1 and group2 have much higher fluxes to the gaseous than the aqueous phase, which can be explained by their high Henry constants (145 and 165 respectively). For most of the components the fluxes fall in the range $10^{-4} – 10^{-5}$ mole/day. The flux of isopropylbenzene is lower, following the pattern of its aqueous flux. Generally the decrease in fluxes that is seen during the simulations for non-composite components in the aqueous phase is likewise seen in the gas phase. The relative magnitudes of the fluxes are, however different for the two phases. Whereas in the aqueous phase the fluxes for the xylenes and ethylbenzene are similar, in the flux to the gas phase of o-xylene is more than one order of magnitude lower than that of m/p-xylene or ethylbenzene. As this difference cannot be due only to the differences in K_H (0.161 for o-xylene, 0.269 and 0.28 for m/p-xylene and ethylbenzene respectively), it would appear that the degradation of these components in the aqueous phase is also an important factor; the degradation rate applied in the simulation for o-xylene (1.1×10^{-8} s^{-1}) is higher than those of m/p-xylene and ethylbenzene (7.3×10^{-9} s^{-1} and 5.2×10^{-9} s^{-1} respectively). Toluene behaves rather anomalously in terms of its flux to the gas phase. Following the initial high flux, the flux decreases rapidly and becomes negative, i.e. from the gaseous to the aqueous phase. This behaviour seems unusual as it results in a net flux from the gas phase to the aqueous phase for the remainder of the simulation, but it has also been observed previously in one-dimensional models (Miles, 2003), with the suggested explanation that it is linked to groundwater recharge. Re-partitioning takes place from the gas phase to the infiltrating uncontaminated recharge, with the net effect being a slight reduction of the mass in the gas phase. In the case of toluene the driving force for this behaviour is the high solubility (556 mg/l), the low overall flux and the degradation in the aqueous phase.

The cumulative total mass fluxes for the simulation show that after the initial period in which the concentration gradients are established, the total mass fluxes from the NAPL to the aqueous and gaseous phases are effectively constant over the 50 years of the simulation. Of the total flux from the NAPL, about 20% is to the gas phase, 80% to the aqueous phase.

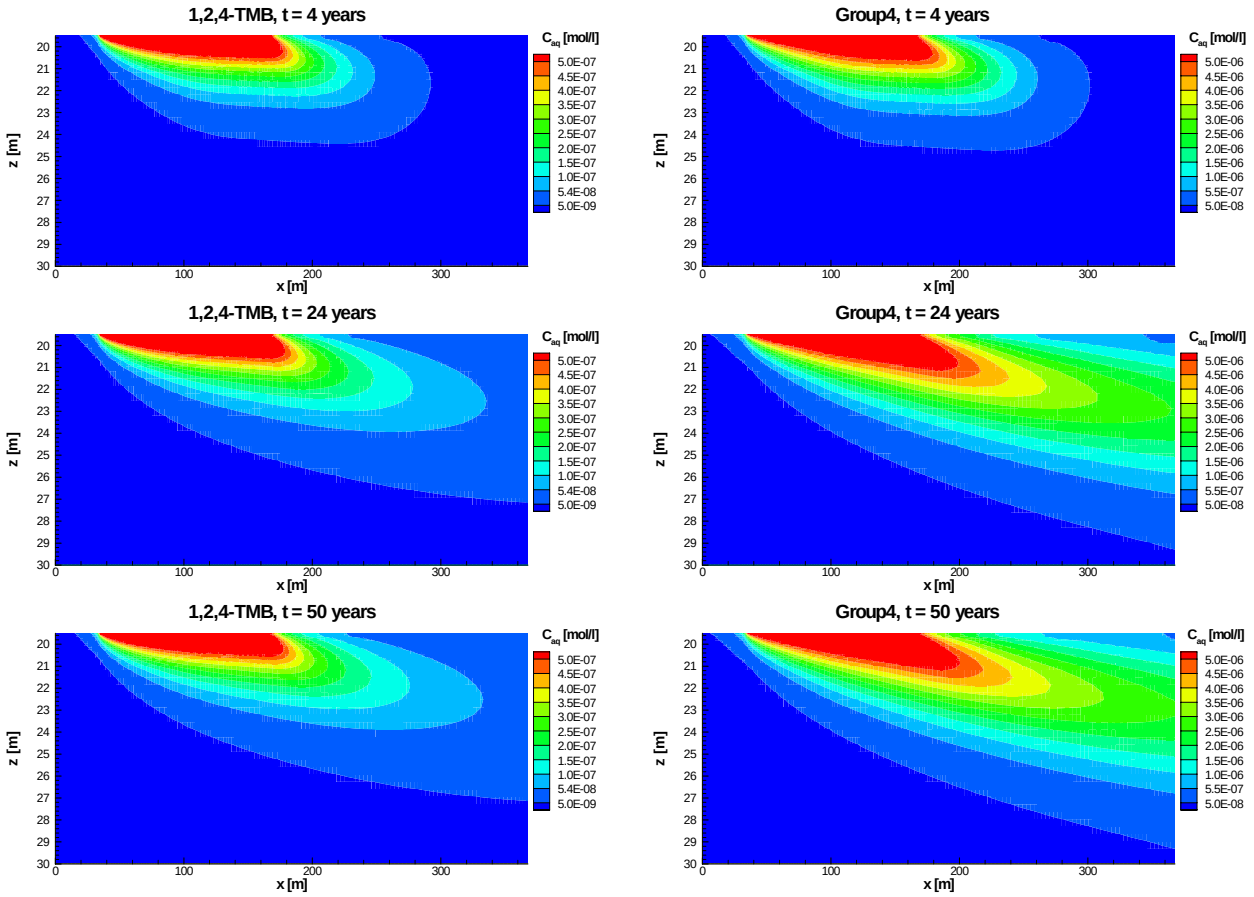

Figure 3.7 Aqueous phase plume development for 1,2,4-TMB and Group4, TL1 base scenario. Concentration levels used for generating the contours in the plots are different for the two components, being one order of magnitude higher for Group4 than for 1,2,4-TMB

The minor numerical problem seen in the model output for some fluxes to the gas phase arises from timestep changes that are forced at specified data output times in the simulation. These fluctuations are however insignificant in the overall mass balance.

Plume development

The evolution of contaminant plumes is a major consideration in assessing the suitability of MNA as a remediation alternative at a contaminated site. As environmental risk is typically defined at specific receptors and is a function of concentration and duration of a contaminant, certain questions should be addressed with respect to contaminant plumes. In particular the questions of the maximum likely plume length, the lifetime of the contamination and the status of the currently observed plume (expanding, steady-state or shrinking) need to be considered.

The development of the aqueous phase plume downstream of a contaminant source is influenced by a number of factors. The rate of growth of the plume and the maximum length that it attains depend on the emission from the source zone and the rate of advective

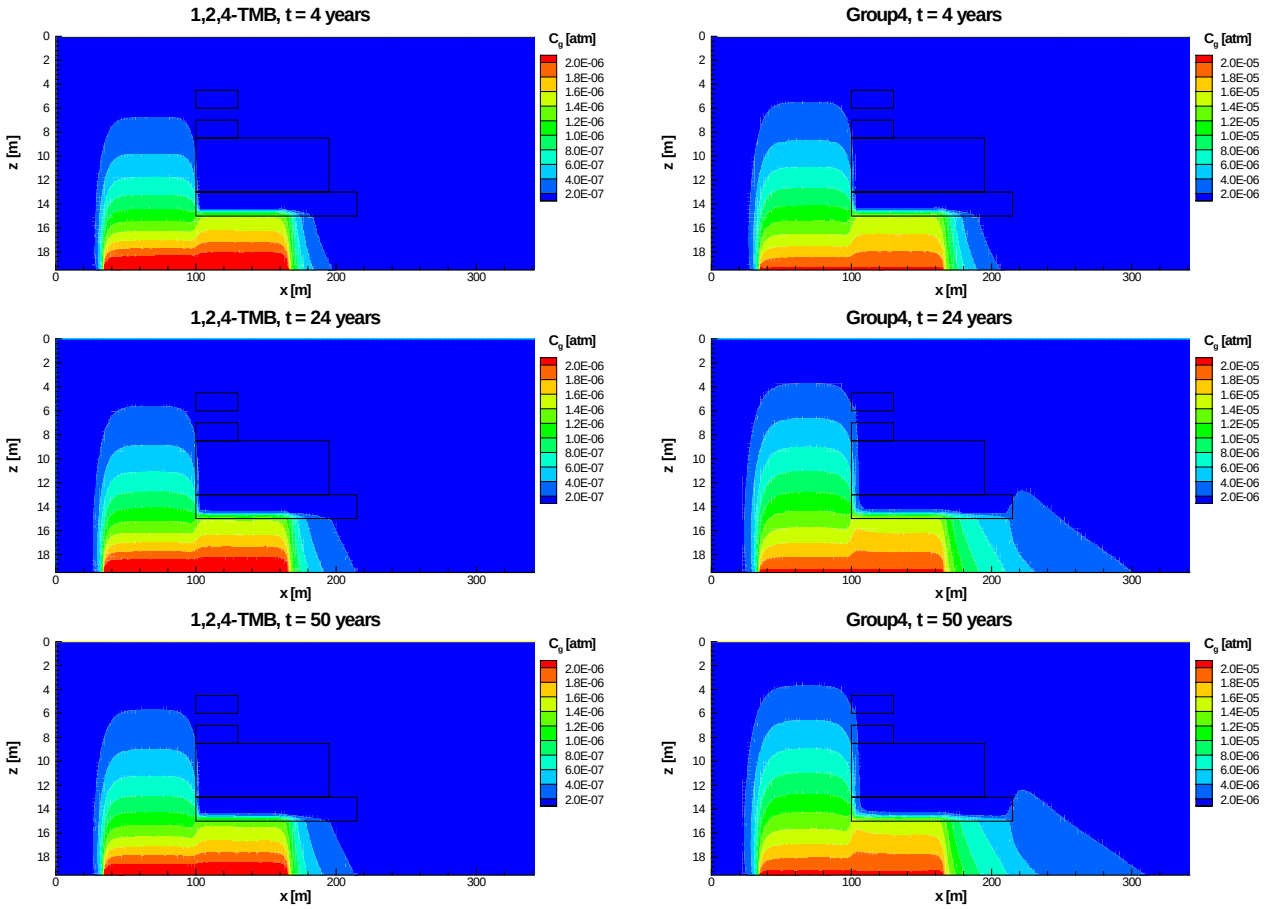

Figure 3.8 Gas phase plume development for 1,2,4-TMB and Group4, TL1 base scenario. Black rectangles show the positions of silt layers in the domain. Concentration levels used for generating the contours in the plots are different for the two components, being one order of magnitude higher for Group4 than for 1,2,4-TMB.

transport, which cause the plume to grow, as well as the opposing degradative, sorptive and dispersive (volatilisation, dilution) processes. Although dispersive processes themselves do not result in a reduction of contaminant mass, since contaminant plumes are typically defined spatially by a threshold concentration level they can contribute to a steady state. In looking at the simulated development of the contaminant plumes for the base scenario, intended to represent the "actual" situation at TL1, it is useful to consider two of the modelled kerosene components in order to compare the behaviours of a degrading and a non-degrading component. In this respect 1,2,4-TMB and the composite compound Group4 (which represents 1,2,4,5-Tetramethylbenzene, 1,2,3- and 1,3,5-TMB) are a sensible choice for comparison, as they have almost identical physico-chemical properties and similar mole fractions in the kerosene mixture and thus should be comparable in terms of emission.

and Figure 3.8 show the development of the aqueous and gaseous phase plumes for these components. Figure 3.9 shows the maximum downstream plume lengths during the simulation for different threshold concentrations.

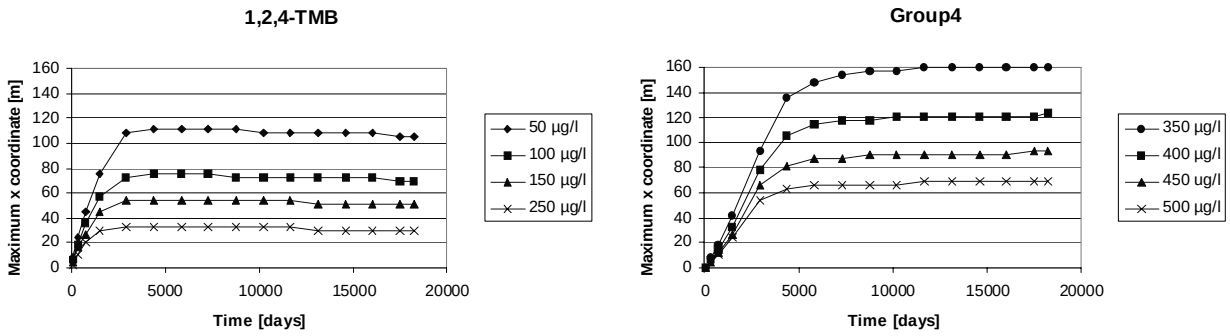

Figure 3.9 Maximum distance from the downstream boundary of the source zone of different concentration isolines for 1,2,4-TMB and the composite component group4 during the simulation.

In the aqueous phase, in both cases the plumes develop downstream from the source zone with the depth of the plume front increasing with distance due to the vertical flow component from groundwater recharge. The 1,2,4-TMB plume is much smaller than that of group4, the difference being due to the degradation of 1,2,4-TMB. Figure 3.9 shows that for 1,2,4-TMB the maximum plume length for a threshold concentration of 50 µg/l is about 110m and is reached after 4380 days (12 years). This period of growth is followed by a steady-state situation with no plume growth, after which a slight shrinkage of the plume is seen towards the end of the simulation. A similar pattern of growth is seen for the other threshold concentrations. Indeed, in

it can be seen that there is no discernible difference between the plumes at 24 years and 50 years. The simulated behaviour of the 1,2,4-TMB plume is consistent with BTEX plume behaviour reported in the literature. Based on studies using analytical models, Huntley and Beckett (Huntley and Beckett, 2002) report that the length of time for which plumes are expanding is short compared to the lifetime of the contamination. Wiedemeier et al. (1999) summarise and combine the results of a number of statistical studies of petroleum hydrocarbon plumes. Based on a 50 µg/l limit, 72% of plumes in the studies were less than 60m in length, while 93% were less than 150m in length. Additionally, one of the studies reported that 59% of the plumes were stable (steady state), 33% were shrinking and 8% were growing (Rice et al., 1995). Figure 3.10shows the maximum extensions of the 50 µg/l isoline downstream from the source zone for the simulated BTEX components. The maximum plume lengths generally fall in the upper range of reported lengths, which is reasonable as the estimated first order degradation rates applied in the scenario are comparable to the lower values of the range reported in the literature. The times taken for the plumes to reach steady state are relatively short, in all cases less than 5000 days (15 years), which is generally consistent with reported data.

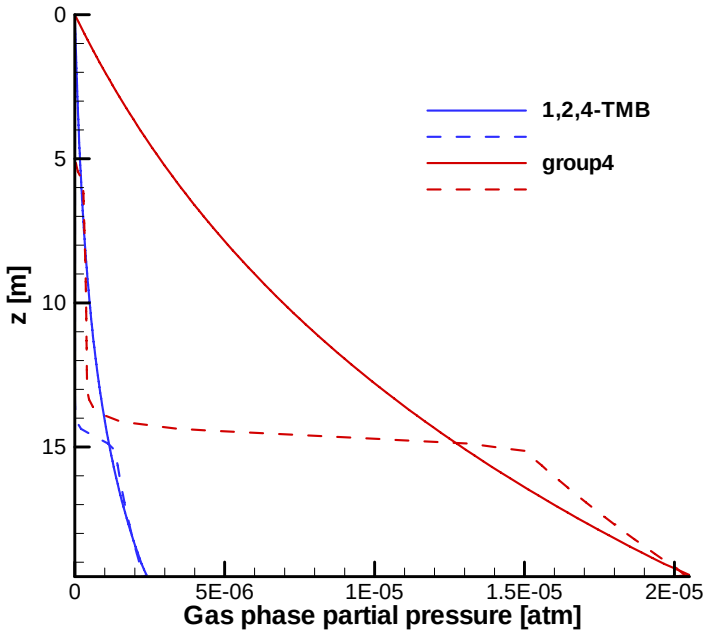

Figure 3.10 Maximum extension of 50µg/l isolines for degrading components. m/p xylene is not included as the 50 µg/l isoline extends beyond the limits of the model domain.

The non-degrading Group4 behaves in a comparable way to 1,2,4-TMB, although the plume rapidly extends beyond the downstream limit of the model domain (x = 370m). In comparing the group4 aqueous phase plumes at 24 years and 50 years, it appears as though a steady state is reached. In Figure 3.9 it can be seen that for the higher concentration isolines that remain entirely within the model domain (C_{aq} > 300µg/l), within about 10,000 days (27 years) the plume ceases to grow. Whether or not this is also the case for the lower concentration isolines could be confirmed by re-running the scenario with an extended

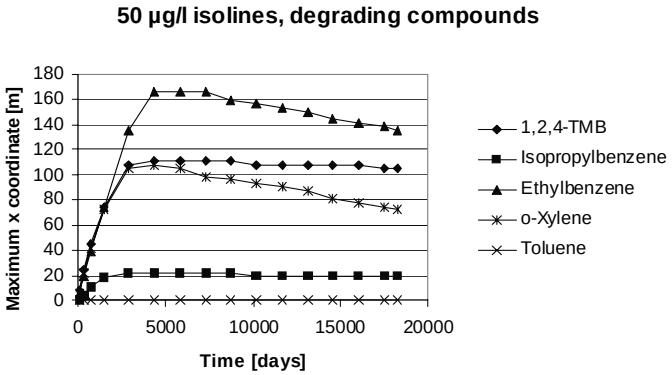

Figure 3.11 Vertical gas phase concentration profiles for 1,2,4-TMB and composite compound group4 at T = 24 years in the basic scenario. Profiles are shown at 2 positions in the model domain; x = 70m, where there are no silt layers (solid lines) and x = 115m, in the area of the thickest silt layers (dashed lines).

domain. A steady state reached for a non-degrading component such as Group4 is due only to dispersion and dilution to below concentration threshold limits and does not involve a reduction in contaminant mass.

In the gas phase, for both components the effect of the silt layers in the unsaturated zone is clear to see in Figure 3.8, acting as a barrier to gas phase diffusive transport. As was the case for the aqueous phase plume below the groundwater table, due to degradation applied in the simulation the gas phase plume that develops in the unsaturated zone has lower concentrations for 1,2,4-TMB than for the non-degrading Group4. Although the degradation in the model is a purely aqueous phase process, the partitioning and equilibration of components between the aqueous and gaseous phases in the unsaturated zone means that degradation can effectively limit the gas phase concentrations and diffusive transport of components. Figure 3.11 shows the vertical gas phase concentration profiles for both components at T = 24 years in the simulation at 2 positions in the model domain; x = 70m, where there are no silt layers and x = 115m, in the area of the thickest silt layers. The gas phase concentrations in the first few meters above the capillary fringe (z > 17m) the gas phase concentrations are very similar at both positions in the domain. However, whereas in the first case, without the overlying silt layers, there is a smooth concentration gradient between the capillary fringe and the surface, in the second position the gas phase concentrations drop sharply at the lower boundary of the silt layers (z = 15m). For both 1,2,4-TMB and Group4 the gas phase plumes quickly reach a steady state in the model, with no observable differences between the situations at 24 years and 50 years in Figure 3.8. The extension of the Group4 gas phase plume further downstream beyond the overlying silt layers demonstrates that the development of the gas phase plume is linked to that of the aqueous phase plume. As the aqueous phase plume develops downstream from the source zone, there is partitioning to the gaseous phase from the upper region of the plume close to the capillary fringe. In this way the gas phase contaminant plume can extend further than would be the case for only gas phase diffusive transport from the source zone.

Figure 3.12 shows vertical profiles of the simulated aqueous phase concentrations after 12 years together with concentrations from December 2003 and May 2004 measured in monitoring wells on and adjacent to the modelled transect. Profiles are shown for three compounds, ethylbenzene, toluene and 1,2,4-TMB. Generally there is poor consistency and agreement between the two sets of measured data. This indicates that there is some degree of uncertainty associated with the measured concentrations arising from the sampling or analysis. While there is no clear pattern to differences between the two data sets, seasonal

variations cannot be ruled out. Furthermore, in comparing the modelled and measured concentrations there is some inherent uncertainty arising from comparing profiles referring to depths in the model domain with the screened depths below the groundwater table of the multilevel sampling points. Bearing this in mind, the modelled concentration profiles compare reasonably well with measured data, generally being in the same order of magnitude. The best agreements between modelled and measured concentrations are seen at B16 and B33, which are located in the most heavily contaminated part of TL1. The measured concentrations at B17, with the exception of toluene, are significantly lower than the simulated. One possible reason for the differences would be the assumption used in the model is that the NAPL source zone is continuous and homogeneous, which in reality is unlikely to be the case. At point B20, located approximately 10m downstream from the end of the source zone in the model domain, and hence with high simulated concentrations, the total concentration of aromatic hydrocarbons detected in samples is less than 10 µg/l, although there is free phase NAPL present in borehole TL1-10, about 15 m away. If the groundwater flow direction is in reality not parallel to the transect or the local flow situation is more complex than assumed, it may be the case that aqueous phase contaminant plume bypasses B20. Since significant dissolved concentrations are measured at points B23 and B24, both located to the east of what is estimated to be the extent of the NAPL contaminated zone, it could be that the flow direction is in a somewhat more easterly direction than previously thought.

PID (Photo Ionisation Detector) measurements of volatile organic compounds in the gas phase were carried out at the site during the direct push survey. Figure 3.13 shows PID profiles at 5 different sampling locations; S15, S16, S22 and S23 are located in the middle of the site, an area with sand only in the unsaturated zone, while S18 is located further to the north-east with thick silt layers in the unsaturated zone. S15 and S16 are in the most heavily contaminated part of the site, where the fuel storage tanks were originally located. While the measurements cannot be directly compared with the model output as they represent only a measure of total volatile organics in the soil gas, the general trend of changing concentration with depth should be comparable. Generally the measured gas phase concentrations drop rapidly in the first 1 to 2 meters above the capillary fringe. With the exception of S23 there are virtually no volatile compounds detected above 16 m. The reason for the anomalous result at S23 is not clear. There is not an identifiable difference between the profiles in areas with and without significant silt layers in the unsaturated zone. The higher gas phase concentrations at S15 and S16 are probably a result of their location in what is thought to be

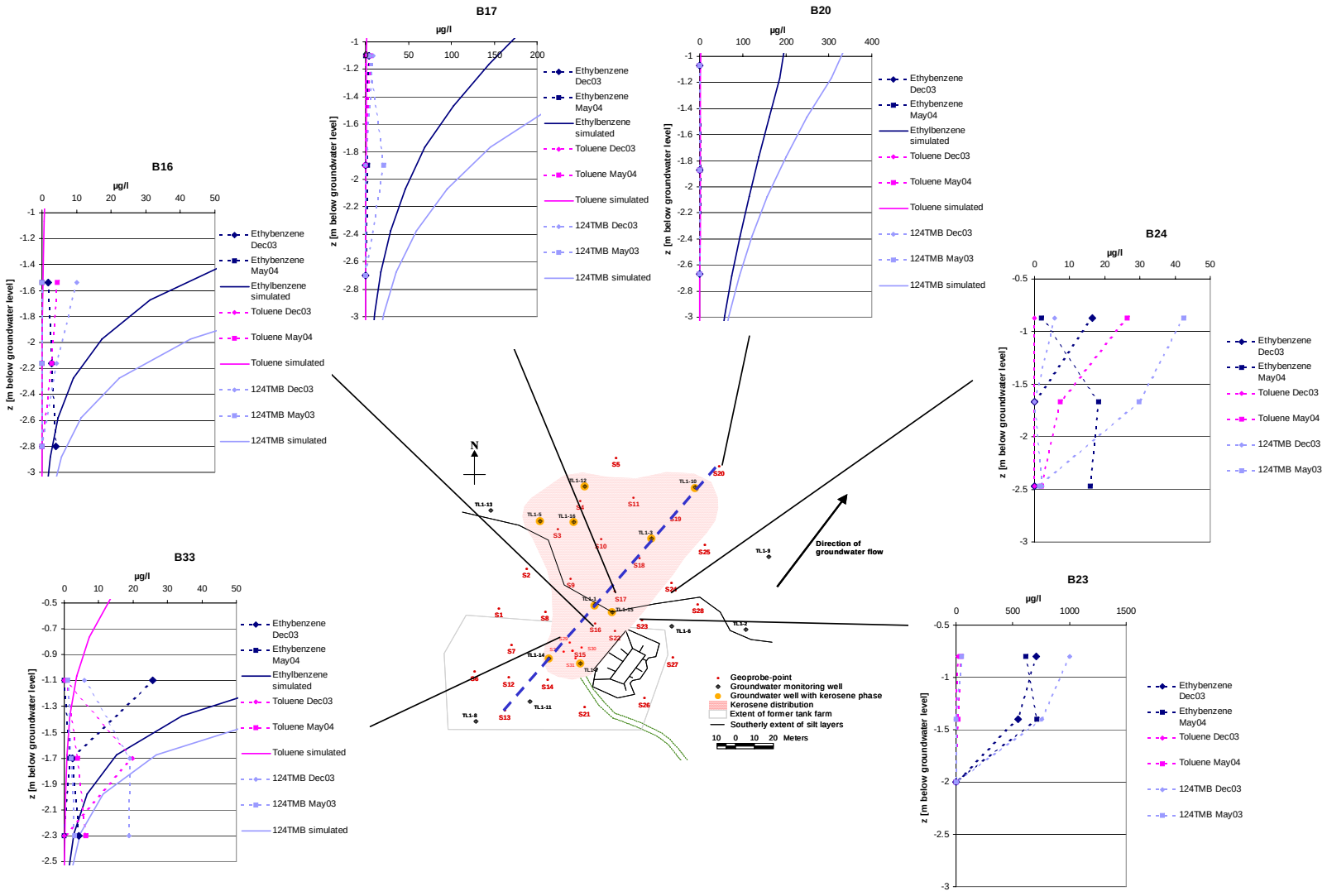

Figure 3.12 Measured aqueous phase concentrations from December 2003 and May 2004 shown with simulated concentrations along the model transect.

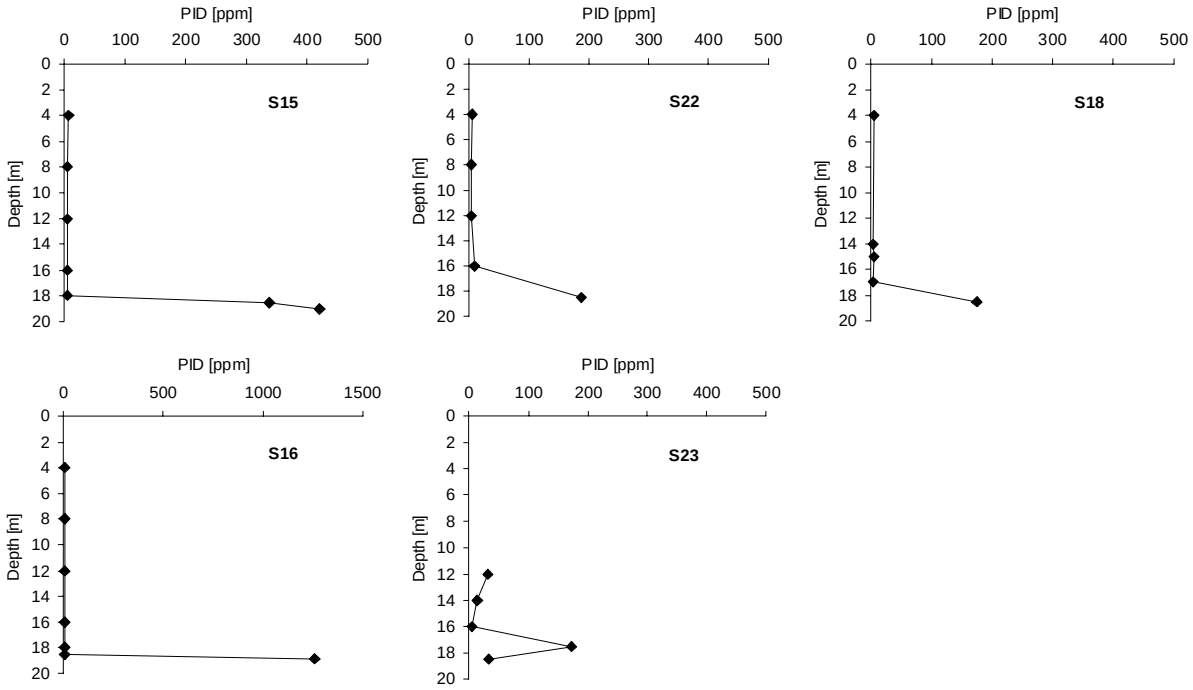

Figure 3.13 Vertical PID profiles of gas phase concentrations of volatile organic compounds in different parts of TL1. S15, S16, S22 and S23 are located in the middle of the site, an area with sand only in the unsaturated zone, while S18 is located further to the north-east with thick silt layers in the unsaturated zone.

the most heavily contaminated part of the site. The type of concentration profiles predicted by the model and shown in Figure 3.11 are not observed in the field. This may be due to a number of reasons. The assumption made in the model of ideally packed homogeneous sand, which provides ideal conditions for gas phase diffusion, is unlikely to be the case in the field. In reality diffusion is likely to be hindered by small scale heterogeneities in the aquifer. Additionally biodegradation may be more significant in the unsaturated zone in reality than in the modelled situation. More detailed analyses of soil gas samples taken in the first meter above the capillary fringe carried out in conjunction with a bioventing experiment at position S15 show no BTEX or other mono-aromatic compounds present in the soil gas. The organic components in the gas phase are mainly $C_1 – C_6$ aliphatic hydrocarbons and a mixture of aldehydes, alcohols, naptha compounds and amines. The absence of BTEX compounds and presence in the soil gas of oxidation intermediates suggests that oxidation of the organic compounds is taking place. Such rapid decreases in gas phase hydrocarbon concentrations due to biodegradation within 1 or 2 meters above the capillary fringe are well documented at LNAPL contaminated sites (Lahvis and Baehr, 1996; Lahvis et al., 1999; Ostendorf and Kampbell, 1991). The implication for the situation at TL1 would be that while volatile compounds are being released to the gas phase from the

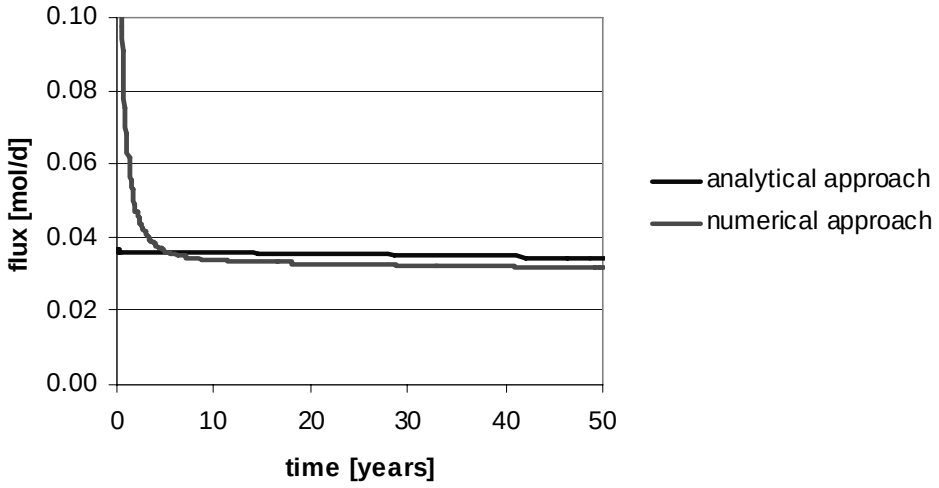

Figure 3.14 Total emission from the source zone for the basic scenario and corresponding analytical solution.

source zone, the spreading of contaminants in the gas phase is probably much more limited at the site than is suggested by the model.

Source zone lifetime

As the numerical approach proved to be impractical for the estimation of source lifetimes due to the execution times involved, the lifetime of the NAPL source zone was estimated using the analytical approach suggested by Huntley and Beckett (2002), with the lifetime of the source defined as the time required for the sum of the aqueous concentrations of the NAPL components in the source zone to fall below 0.1 mg/l. Input parameters for soil, NAPL and groundwater flow were the same as in the basic model scenario. Degradation rates are not included in the analytical approach. Figure 3.14 shows the total emission from the source zone in moles/day for both the numerical and analytical approaches over 50 years. The total emission is very similar in both cases, indicating that the analytical approach should provide a reasonable estimate of the source lifetime. The lifetime of the source zone estimated using this approach was a little over 1700 years based on a 30m × 130m area of NAPL contamination with a thickness of 0.2m.

3.5.2. Sensitivity analyses for estimated parameters

The sensitivity of the numerical model with regard to estimated parameters used in the scenarios is discussed in the following sections. The parameters are discussed first in terms of their effects on contaminant emission and source lifetime (Section 3.5.2.1), and then in terms of the effects the effects on the aqueous plume development (Section 3.5.2.2).

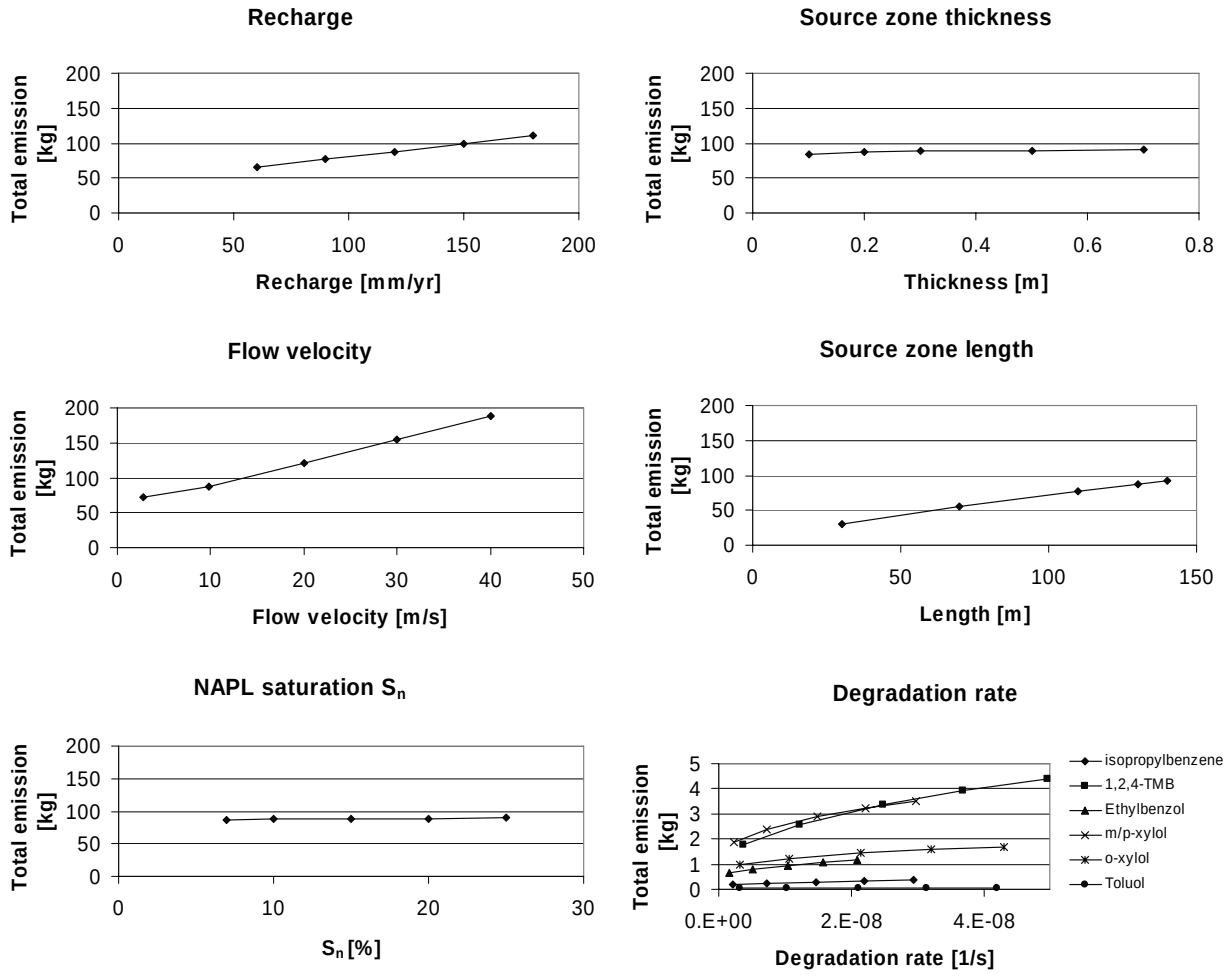

Figure 3.15 Effects of different parameters on the cumulative emission to the aqueous phase after 50 years. In each case the total emission of all components is shown. For degradation rates the individual emissions of the degraded components are shown.

3.5.2.1.Emission and source lifetime

As analysis of the basic scenario showed, the total rate of emission from the NAPL in the model is effectively constant during the 50 years of the simulation. Thus in looking at the sensitivity of the system to changes in different parameters in terms of emissions from the NAPL, it is reasonable to look at total cumulative mass fluxes during the simulation. Figure 3.15 shows the effects of different parameters on total emission to the aqueous phase after 50 years (18,250 days) while Figure 3.16 shows the effects on emission to the gas phase. Results for the lifetime of the source in terms of the time taken for the total aqueous concentration of modelled components in the source zone to fall below 0.1 mg/l are shown in Figure 3.17.

Recharge

Emission to the aqueous phase increases linearly with increasing recharge, as vertically infiltrating recharge passing through the unsaturated zone and source zone results in

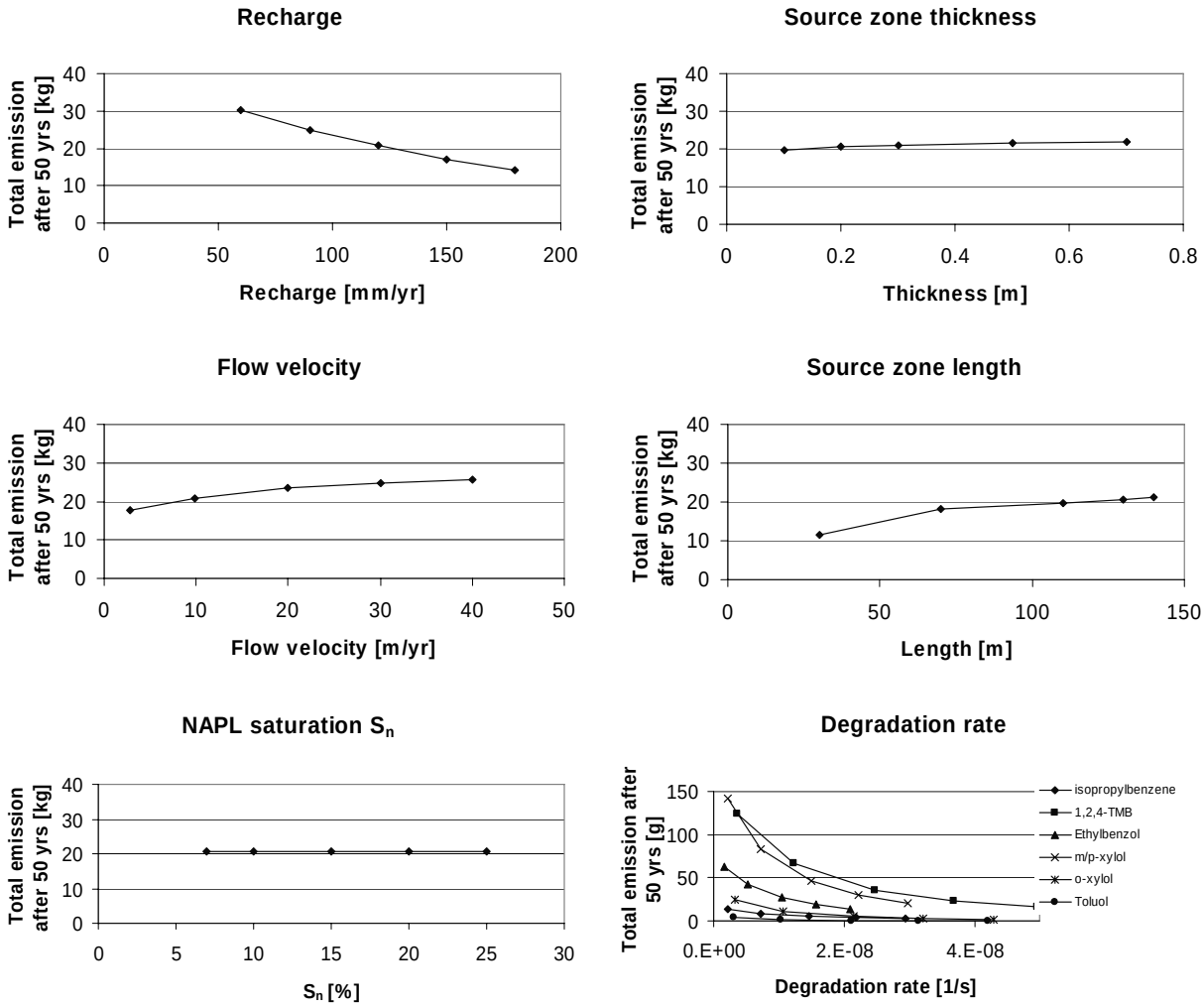

Figure 3.16 Effects of different parameters on the cumulative emission to the gas phase after 50 years. In each case the total emission of all components is shown. For degradation rates the individual emissions of the degraded components are shown.

advective transport of the NAPL components across the capillary fringe. The vertically flowing water reaches saturation concentration for all NAPL components both through partitioning from the gas phase in the unsaturated zone and dissolution of the NAPL in the source zone. Thus the mass of NAPL transferred to the aqueous phase is proportional to the volume of water available for transport. Extrapolation of the linear relationship suggests that in the absence of groundwater recharge there would still be a significant emission to the aqueous phase, which would be due to concentration gradient driven diffusive flux from the source zone across the capillary fringe.

Total emission to the gas phase, shown in Figure 3.16, decreases in a slightly non-linear way as recharge increases, with a threefold increase in annual recharge from 60mm/yr to 180mm/yr resulting in a 50% decrease in emission over 50 years. An increase in recharge represents an increased supply of uncontaminated water in the unsaturated zone, which

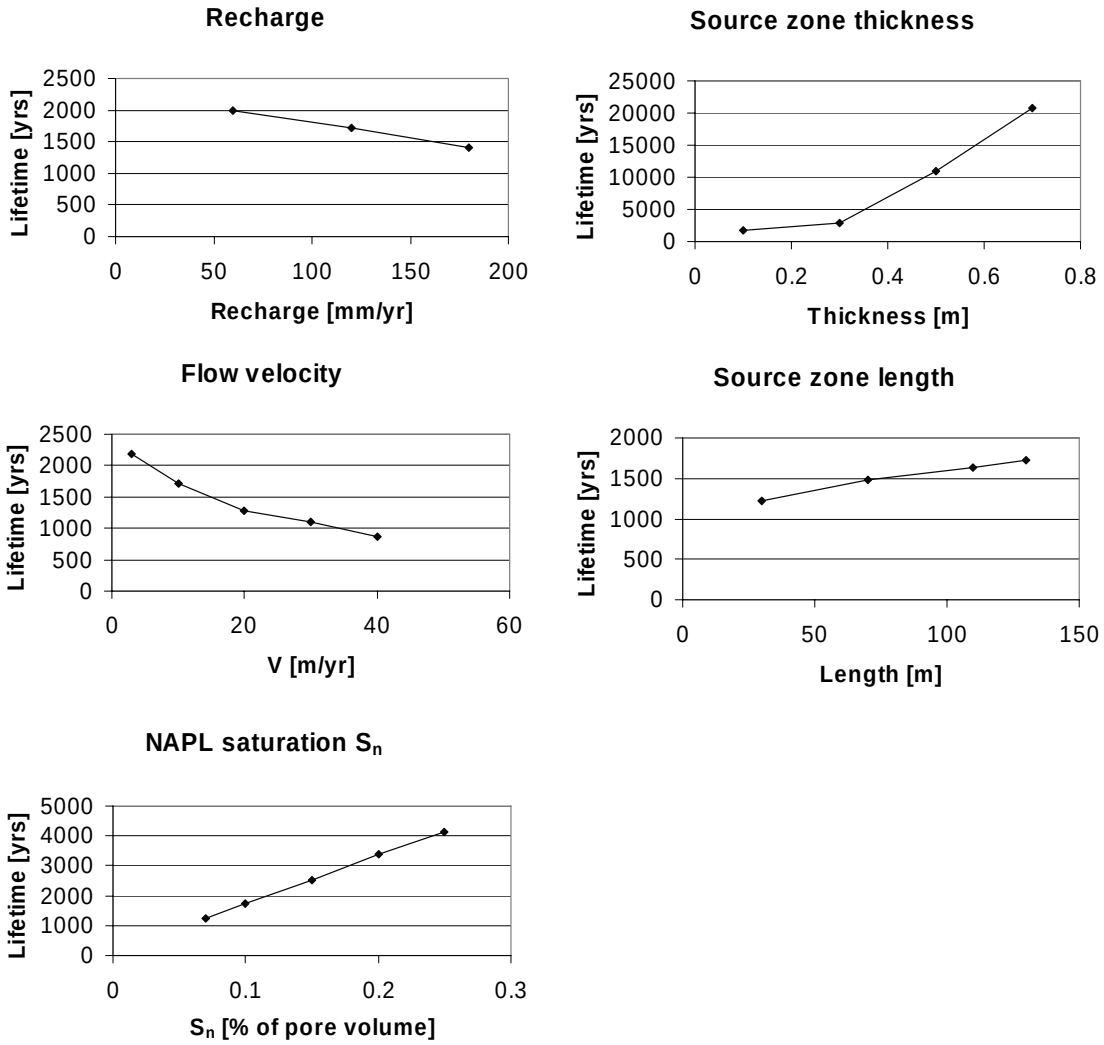

Figure 3.17 Sensitivity of source lifetime to different parameters

means that there is an increased capacity for components to partition from the gas phase to the aqueous phase.

The net effect of increasing recharge is an increase in total emission, which in turn results in an inverse linear relationship between groundwater recharge and the expected source lifetime.

Flow velocity

Ground water flow velocity has a significant influence on the emission to the aqueous phase in the scenarios, with emission increasing with increasing flow velocity. Over the range of velocities modelled (3 m/yr to 40 m/yr) the total emission to the aqueous phase over 50 years is almost three times greater at 40 m/yr than at 3 m/yr. The reason for this is well illustrated by the vertical concentration gradients that develop below the source zone, which control the diffusive transport of components out of the source zone, and in turn the rate of

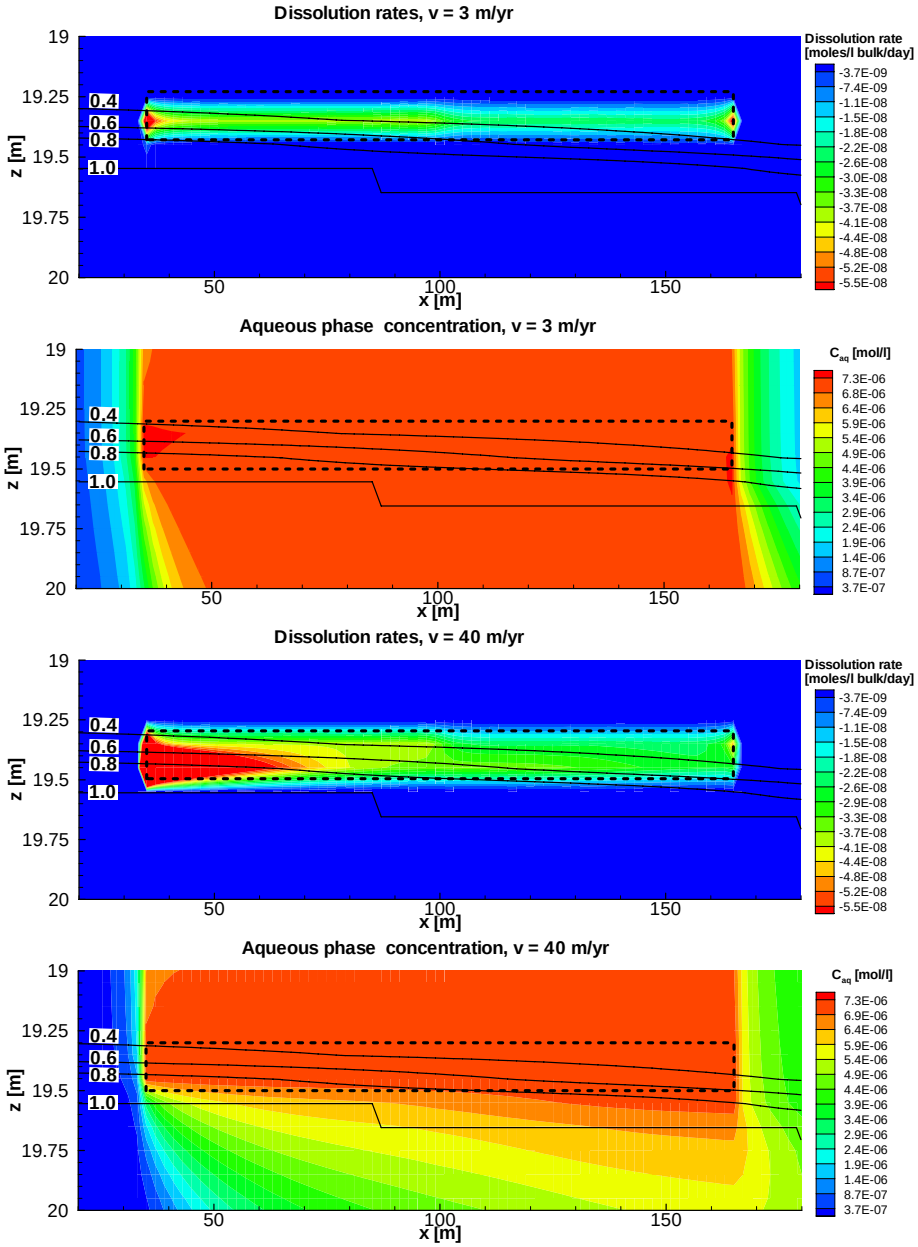

Figure 3.18 Source zone dissolution rates and aqueous phase concentrations for NAPL composite component group4 at t = 4 years with groundwater flow velocities of 3 m/yr and 40 m/yr. The dashed rectangular outline shows the approximate position of the source zone in the model domain. The black contour lines refer to the degree of aqueous saturation, with the 1.0 line showing the position of the groundwater table

dissolution from the NAPL. Figure 3.18 shows the source zone dissolution rates, (the values are negative as they are generated with respect to the solid phase), and aqueous phase concentrations in surrounding the source zone at t = 4 years for groundwater flow velocities of 3 m/yr and 40 m/yr. The figure shows data for the composite component group4, which has a fairly representative and stable emission (see Figure 3.6) and is non-degrading in the simulations.

The pattern of dissolution rates in the source zone for the lower limit flow velocity of 3 m/yr has a number of interesting features. In general the dissolution is limited to the upper portion of the source zone, where two processes dominate. Volatilisation from the aqueous phase, which in turn is a driving force for dissolution from the NAPL phase, takes place predominantly in the upper part of the NAPL layer as it relies on a concentration gradient maintained by gas phase diffusive transport away from the source zone. At the same time, vertically flowing recharge water becomes saturated with the dissolved NAPL components within the first few centimetres of the NAPL layer. The dissolution rates are observably lower in the portion of the source zone overlain by the silt layers ($x > 100$m). The reason for this is the overlying silt layers limiting gas phase transport (see Figure 3.8 and Figure 3.11). The reduced concentration gradient in the gas phase above the source zone limits volatilisation from the aqueous phase, and hence dissolution from the NAPL phase. Meanwhile, the vertically flowing recharge water is closer to saturation concentration due to gas/aqueous phase partitioning by the time it reaches the source zone and hence has less capacity for dissolution of the NAPL directly in the source zone than is the case where there are no overlying silt layers. The dissolution “hotspots” at either end of the source zone are due to the higher concentration gradients in found in those areas, which can be seen in the plot of aqueous phase concentration. At the downstream (right hand) end of the source zone there is a horizontal concentration gradient away from the source zone boundary. At the upstream (left hand) end there is both a horizontal gradient as well as a slight vertical gradient due to the groundwater flow from left to right beneath the source zone, which results in a slightly greater dissolution at the upstream than the downstream end. These features, although less visible, are likewise present at the higher flow velocity of 40 m/yr. Similar behaviour, with elevated dissolution at the edges of a NAPL body in a modelled system is reported by Essaid et al. (2003).

From the aqueous phase concentrations and source zone dissolution rates for 40 m/yr flow velocity, it can be seen that the increase in flow velocity, and hence volume of water per unit time passing beneath the source zone results in increased vertical concentration gradients below the source zone, especially towards the upstream end, and corresponding increases in the NAPL dissolution rates. A secondary and fairly minor effect of the increased flow velocity is seen in the horizontal concentration gradients at either end of the source zone. At the upstream end the gradient, and hence dissolution, from the end of the source zone is increased, while the development of the aqueous phase plume downstream

from the source zone results in a reduced horizontal concentration gradient and hence slightly reduced dissolution.

It has previously been suggested that for large contaminant areas with low horizontal concentration gradients one-dimensional diffusion models are sufficient to describe transport of volatile organic compounds in the unsaturated zone when groundwater velocities are low (McCarthy and Johnson, 1993), and one-dimensional modelling at TL1 was carried out on this basis (Miles, 2003). The two-dimensional results suggest that while this assumption might be valid for the lower limit flow velocity estimate for the site of 3 m/yr, for velocities above this, i.e. those likely to be valid for TL1, the velocity plays an important role in determining diffusive transport from the source zone.

In contrast, the effect of flow velocity on the overall flux to the gas phase is fairly minor, as might be expected since the flux to the gas phase mainly takes place in the unsaturated zone around the NAPL source. Generally the relationship is non-linear, with an increase in velocity leading to an increase in flux, with the effect decreasing with higher velocities. The reason for this is the increase in partitioning to the gaseous phase across the capillary fringe from the upper parts of the aqueous phase plume as the increased velocity causes the plume to extend beyond the overlying silt layers. Once the velocity is sufficient for the plume to extend beyond the silt layers, further increases have little effect.

Corresponding to the increase in emission from the source zone, increasing groundwater flow velocity leads to a decrease in the lifetime of the source, with the lifetime for a flow velocity of 40 m/yr of around 800 years compared to 2200 years at a flow velocity of 3 m/yr.

NAPL saturation

Changes in NAPL saturation in the source zone within the range of values modelled had no effect on the total mass flux of NAPL components to the aqueous or gaseous phases, as the emission depends on the rate of dissolution and transport of components away from the source and saturation concentrations in the aqueous phase are reached regardless of the NAPL saturation in the pore volume. At the lower saturations the total fluxes of some individual components such as toluene, with low mole fractions in the kerosene mixture were lower after 50 years as they became depleted in the source zone, with reduced mole fractions leading to correspondingly reduced aqueous phase equilibrium concentrations. The degree of saturation in the source zone does however have a significant effect on the source

lifetime, as the overall mass of NAPL constituting the source increases with increasing saturation, which results in a linear increase of source lifetime with saturation.

Source zone thickness

Similarly to the degree of NAPL saturation, the thickness of the source zone does not affect the emissions in the simulations, and for the same reason, i.e. that saturation concentrations are reached even for a very thin source zone, and it is the rate of transport out of the source zone that controls the emission. As was also the case for low NAPL saturations, with a thin source zone after 50 years a reduction in the emission of some individual components after 50 years was seen as they became depleted in the source.

The effect on the source lifetime resulting from varying the source zone thickness in the analytical approach is however significant, with the lifetime increasing non-linearly with thickness. An increase in thickness from 0.1 to 0.7m leads to an increase in lifetime from 1,600 to 21,000 years. The analytical approach assumes vertical equilibrium distribution of NAPL in the capillary fringe, the total mass of NAPL increases non-linearly with the thickness of the NAPL layer, while the flux of water through the source does not change significantly.

Source zone length

The length of the source zone (i.e. the lateral area) affects emissions to both the aqueous and gaseous phases. For emission to the aqueous phase there is a linear increase of total emission with source zone length, indicating a constant emission per unit area. This is reasonable, as the emission is to a large extent a result of the advective flux due to recharge, which is evenly distributed in the model domain and diffusive flux out of the source zone, which occurs mainly at the upper and lower surfaces.

The flux to the gas phase shows a similarly linear relationship, depending as it does mainly on vertical diffusive transport, but with a change in gradient as the source zone reaches 70m in length. The reason for this change in gradient is that the first 60m of the source zone are overlain by sand only in the unsaturated zone. Further extending the source zone takes it beneath the overlying silt layers, which, as has already been seen, act as a barrier to gas phase diffusive transport in the model and limit emission to the gas phase.

The lifetime of the source zone also follows a linear relationship, increasing with the source zone length and overall NAPL mass. The increase in the lifetime is however mitigated to some extent by the simultaneous increase in the emission as the length increases.

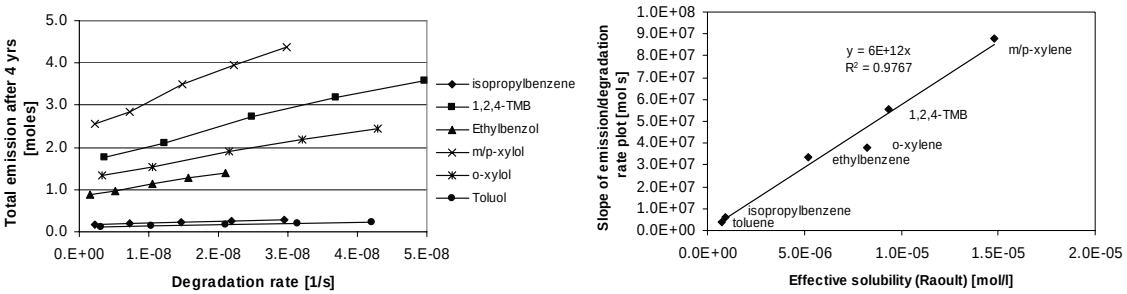

Figure 3.19 Relationship between effective aqueous solubility from the initial kerosene mixture according to Raoult's law and the slope of the cumulative emission vs. degradation rate plot at t = 4 years in the simulation

Degradation rate

The relationships between degradation rates and total emission rates to the aqueous and gaseous phases are shown for each of the components subject to degradation in the simulations. In the aqueous phase, in all cases increasing degradation rates cause an increase in emission from the NAPL. The flattening of the curves at higher degradation rates for some compounds reflects the depletion in the source zone, and hence reduced emission, during the simulation. The degree to which the emission of a particular component is affected by an increase in degradation rate can be linked to its effective solubility. Figure 3.19 shows the relationship between effective aqueous solubility from the initial kerosenemixture according to Raoult's law and the slope of the cumulative emission vs. degradation rate plot at t = 4 years in the simulation – before depletion of the components in the NAPL begins to affect their emission. The points plotted in Figure 3.19 are thus a representation of the sensitivity of the emission of a component to increasing degradation rate against the effective solubility. The increase of emission of a component with degradation rate is a linear function of its effective solubility. This can be explained by considering that in the source zone all of the components are at saturation concentration in the aqueous phase. The mass of a component removed by degradation in a model cell in a particular timestep is a function of its aqueous phase concentration, and mass removed from the aqueous phase is replaced by dissolution from the NAPL phase. Thus if two components had identical degradation rates, the mass flux from the NAPL to replace degraded mass in the aqueous phase would be higher for the component with the higher aqueous solubility. Likewise for a given increase in degradation rate, the resulting increase in mass flux will be higher for components with higher aqueous solubilities. Similar behaviour has been reported

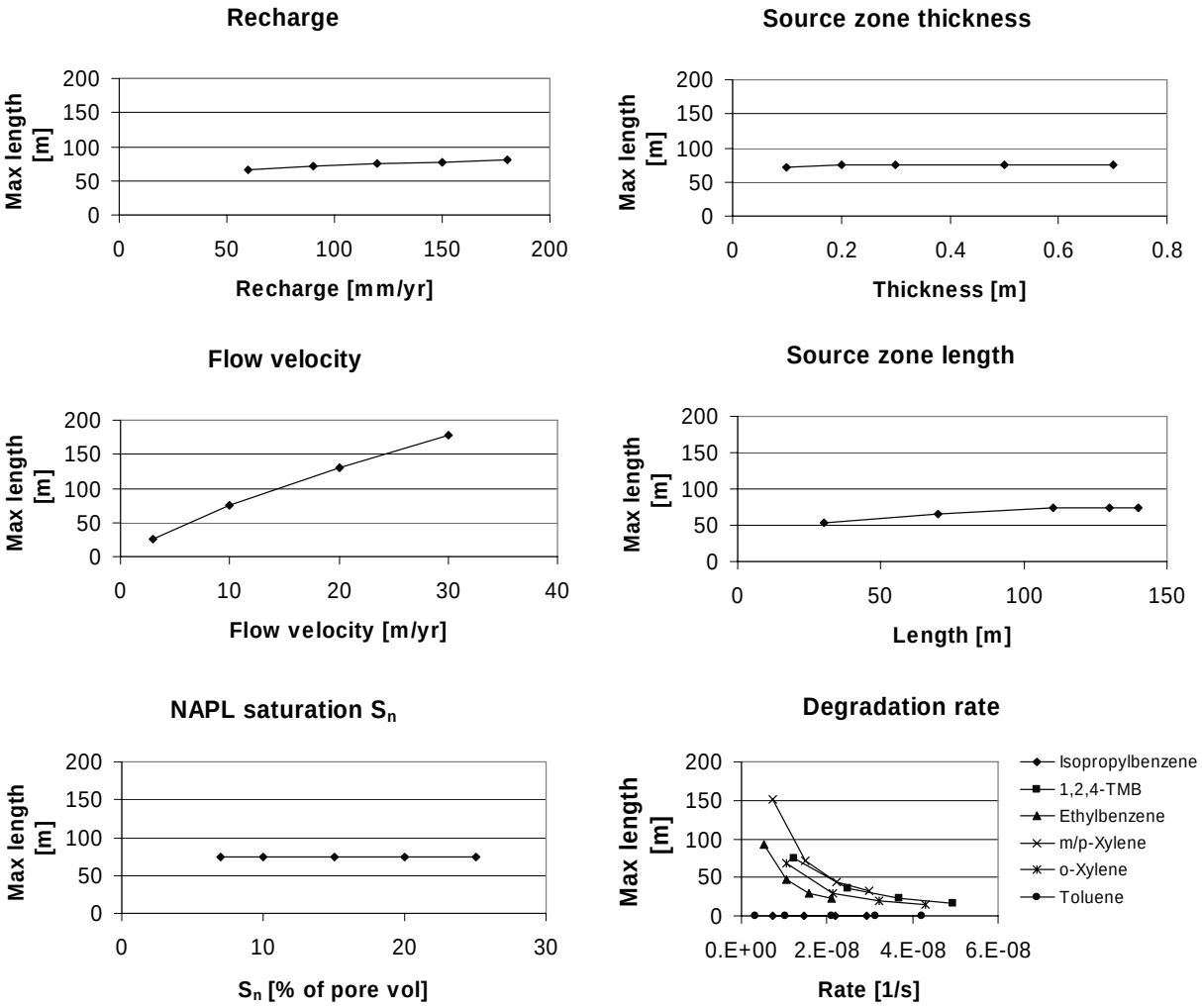

Figure 3.20 Sensitivity of maximum plume length (maximum x- coordinate of the isoline) in the simulation to changes in parameters for the 1,2,4-TMB 100 µg/l isoline

for simulations of contaminant emission and degradation using a more complex aerobic/anaerobic representation of biodegradation (Essaid et al., 2003). Essaid et al. observed that biodegradation enhanced dissolution by 260% for benzene, 850% for toluene, 320% for ethylbenzene, 430% for m/p-xylene, and 810% for o-xylene compared to a model without biodegradation. They similarly attribute the increase to biodegradation lowering concentrations in the aqueous phase, thus providing a driving force for increased dissolution. Whether this phenomenon occurs in reality is debatable, and for this reason degradation rates are omitted from the analytical approach used to estimate the source lifetime (Huntley and Beckett, 2002).

Mass fluxes to the gas phase decrease in response to increasing degradation rates as the flux to the gas phase is an equilibrium process that depends on aqueous phase concentrations. The degree to which the individual components are affected depending on their aqueous phase saturation concentrations in the same way as for the aqueous phase.

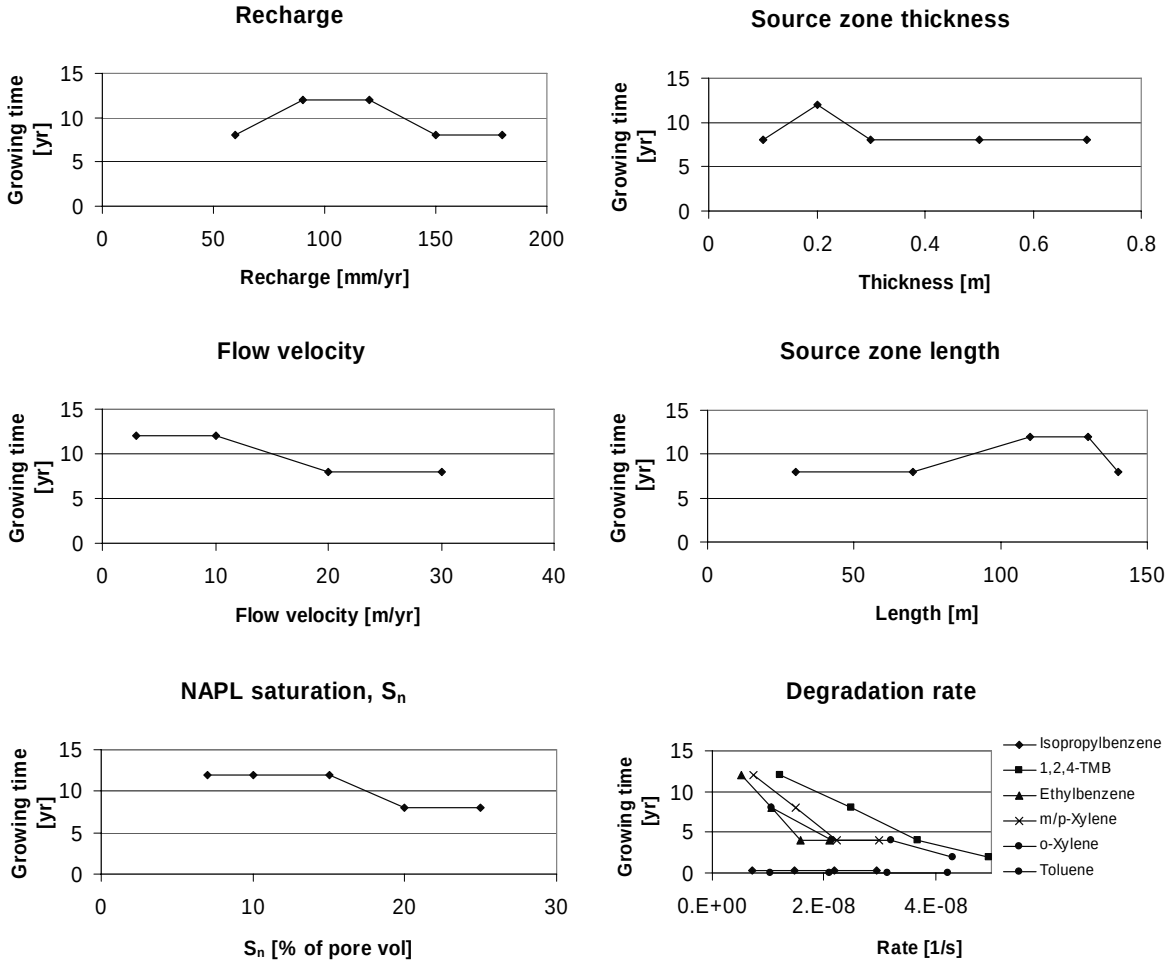

Figure 3.21 Sensitivity of plume growing time (time taken for the isoline to reach its maximum x-coordinate in the simulation) to changes in parameters for the 1,2,4-TMB 100 µg/l isoline

3.5.2.2.Plume development

The sensitivity of the maximum plume lengths and plume growing times for the 1,2,4-TMB 100 µg/l isoline to the various parameters are shown in Figure 3.20 and Figure 3.21 respectively. The other compounds behave in a similar manner to 1,2,4-TMB.

Recharge

Recharge has only a minor effect on the maximum plume length in the simulations, with an increase in recharge from 30 mm/yr to 180 mm/yr resulting in an increase from 60 m to 80 m in the maximum extension of the 100 µg/l isoline for 1,2,4-TMB. The increase can be attributed to the increase in emission rate to the aqueous phase caused by the increase in recharge. There is, however, no effect on the time taken for the isoline to reach this maximum extension, between 4 and 8 years.

Flow velocity

As might be expected, flow velocity has a significant effect on the maximum extension of the plume as it affects both emission rates from the NAPL and advective transport. An increase in velocity from 3m/yr to 30m/yr causes an increase in maximum length from 20m to 168m for the 100µg/l isoline. For the upper limit flow velocity in the simulations, 40m/yr, this isoline extends more than 205m from the source zone, beyond the downstream boundary of the model domain. The time taken to reach maximum length is, however, apparently not dependent on the flow velocity, being between 4 and 8 years. The apparently longer growing times for 3 and 10m/yr are probably not of significance, the difference between the maximum isoline extension at 8 years and 12 years being 2 meters, or 1 model cell.

NAPL saturation

The degree of NAPL saturation in the source zone within the range simulated has no effect on the maximum plume length. There is no clear influence on the time for which the plume is growing; the decrease in growing time from 12 years to 8 years that is seen for $S_n > 15\%$ arises from a difference of 3m, or 1 model cell, in the overall plume length at these times.

Source zone thickness

Similarly to the degree of NAPL saturation, the source zone thickness, has no effect on the maximum plume length. The plume growing time appears likewise to be independent of the NAPL layer thickness.

Source zone length

The length of the NAPL source zone, which as previously seen causes a linear increase in the rate of emission to the aqueous phase, has a non-linear effect on the maximum plume length from the downstream end of the source zone. This is because although the emission to the aqueous phase is increasing as the length of the source zone increases, the plume passing beneath the source zone is also subject to degradation over an increasing distance. The length of the source zone has no effect on the growing time for the downstream plume

Degradation rates

As would be expected, degradation rates have a significant effect on the maximum downstream plume lengths, with the maximum length decreasing non-linearly with increasing degradation rate. Isopropylbenzene and toluene, having very low rates of

emission compared to the other components, are not found at concentrations greater than 100µg/l downstream of the source zone. For the remaining degrading components, the decrease in the maximum plume length corresponds to the increase in degradation rate. Plume growing times are also affected by degradation rates. As degradation rate increases, the time taken for the plume to reach maximum length also decreases. Allowing for the coarseness of the data, it appears that the effect on the plume growing time of increasing degradation rates by a given factor is the same for all of the degrading compounds, i.e. independent of emission rates.

3.6. Summary and conclusions

A two-dimensional multiphase variably saturated flow and transport model was used to assess contaminant emission and transport at a contaminated site with an immobile LNAPL source zone in the capillary fringe. The kerosene source was simplified using a constituent averaging technique to create composite compounds, with dissolution to equilibrium concentrations according to Raoult's law. Biodegradation of aqueous phase contaminants was simulated using a first-order kinetic model. Multiple scenarios were simulated to evaluate the influence of various parameters on the source zone emission and contaminant fate.

The multi-component representation of the source zone showed that while the rates of emission for different contaminants cover several orders of magnitude depending on their solubilities and mole fractions in the mixtures, for most components of the LNAPL mixture they remain effectively constant over the timescale of the simulations. Significant changes in emission during the 50 year simulation time are only seen for the most soluble or volatile components with low mole fractions. Of the total contaminant emission, roughly 80% was to the aqueous phase, 20% to the gas phase.

In the base scenario, a steady-state or maximum aqueous phase plume length was observed within 20 years for all degradable compounds. The maximum plume lengths were different for the different compounds due to their different emission and degradation rates. Shrinking plumes were observed for compounds that became depleted in the source during the simulation. Steady state plumes were also observed for compounds treated as non-degrading in the simulations, however this was due to dispersive processes only.

The development of the gas phase plumes in the simulations showed that the silt layers in the unsaturated zone hinder the diffusive transport of contaminants in the gas phase due to

the water retention characteristics of the silt. Significant gas phase concentrations of organic contaminants have not been measured in the field, whereas degradation intermediates have been detected in the immediate vicinity of the capillary fringe, suggesting a rapid degradation of volatilised contaminants, possibly due to a more aerobic environment in the unsaturated zone. However the simple first-order degradation model applied here, whereby the degradation rate is simply a function of aqueous phase substrate concentration and electron acceptors are not considered, cannot account for this.

Overall, the sensitivity of the source zone emission, plume development and contamination lifetime to the parameters tested was broadly consistent with findings in other work related to LNAPL contaminated sites, both in modelled systems (Huntley and Beckett, 2002) and in the field (Rice et al., 1995). Emission from the source zone was found to be largely insensitive to the LNAPL saturation and vertical extent of the source zone, but the lateral extent of the contaminated area did have an effect on emission, mainly through increased exposure of the source zone to vertically infiltrating groundwater recharge. These source zone parameters were however of importance for the lifetime of the contamination. The hydrogeological and hydrological conditions (groundwater flow velocity and recharge rates) were important for both contaminant emission and source lifetime. With regard to plume development, the maximum downgradient extent of the aqueous phase contaminant plume was not related to the mass of NAPL present in the source zone, instead being mainly dependent on the groundwater flow velocity and biodegradation rates. The time taken for aqueous phase plumes to reach their maximum lengths was affected only by the biodegradation rate.

Applying these findings to the situation at TL1, where MNA is under consideration as a remediation alternative, two main factors come into consideration; risk to receptors in the environment and the likely duration of the contamination. In the first instance, the model indicates that the contaminant plume will reach steady state at the site assuming that the electron acceptor supply and conditions supporting biodegradation remain stable. A better knowledge of the hydrogeological situation at the site and additional estimates of biodegradation rates would enable an improved estimation of the likely steady-state extent of the contamination. The short plume growing times for the modelled scenarios, which concur with statistical works on fuel hydrocarbon contaminated sites, anecdotal evidence and other modelling work (Huntley and Beckett, 2002; Rice et al., 1995; Wiedemeier et al., 1999), indicate that, given the known history of the site, the situation may be in or approaching a steady state. The uncertainty in the distribution and continuity of the LNAPL

in the source zone is of little importance for the plume development, and hence risk to potential receptors but has implications for the second factor, the probable lifetime of the contamination, which is strongly dependent on the quantity and distribution of the NAPL in the source zone. This is also important if considering the potential benefits of source zone removal or reduction at the site. The modelling indicates that, if effective, removal of NAPL from the source zone might result in a reduction in the source lifetime but would not have an impact on the maximum plume length, i.e. risk to receptors would only be reduced in terms of a possible reduction in the exposure duration.

4. Case Study 2: Niedergörsdorf Tanklager 2

4.1. Introduction

Niedergörsdorf Tanklager 2 (TL2) is considered as an example of the Type 2 LNAPL contamination defined in Section 1, where LNAPL is present at a high saturation in the unsaturated zone and forms mobile floating pools at the groundwater surface. The aim of the modelling study at TL2 was to examine how such a complex source geometry affects the emission of contaminants to the aqueous phase, the estimation of which is important for MNA both as a comparison for measured down-gradient mass fluxes in order to estimate fractional mass flux reduction, and hence the amount of biodegradation, as well as for estimating the lifetime of the source.

One approach to quantifying emission from an LNAPL source is to apply analytical methods to calculate the LNAPL distribution in the source zone and to quantify the contaminant emission. Huntley and Beckett (2002) proposed such an analytical solution to estimate emission, in which they used the soil capillarity equations of van Genuchten (1980) to calculate the vertical saturation profiles for the LNAPL/water/air system across the capillary fringe. They then estimated the groundwater flux through the source zone based on the relative permeabilities as influenced by the phase saturations. Emissions to the aqueous phase were calculated as the sum of two mass fluxes: advective transport due to groundwater flux through the source zone and vertical diffusive transport to the groundwater zone below the LNAPL source zone. Peter et al. (submitted) presented a similar analytical approach, modified to account for the advective mass flux due to groundwater recharge flowing vertically through the source zone. Such analytical approaches, while offering the advantage of being relatively simple and easily implemented for multiple component LNAPLs in spreadsheet form, are limited in that they can only be applied to LNAPL bodies of regular geometry in a homogeneous porous medium, and they also rely on the assumption of static equilibrium conditions. The distribution of LNAPLs in the pore space of natural sediments, which might be expected to influence their dissolution behaviour (Mayer and Miller, 1996; Zhu and Sykes, 2000) is, however, highly spatially variable. Numerous studies have demonstrated the influence of heterogeneities on multiphase fluid migration and redistribution in the subsurface (Essaid et al., 1993; Huntley et al., 1994; Kueper et al., 1989; Sleep and Sykes, 1993); moreover, for LNAPLs under transient groundwater flow conditions, temporal fluctuations of the groundwater table lead

to NAPL redistribution and “smearing” of the LNAPL source zone across the capillary fringe.

An alternative to the analytical approach is to use a numerical, multiphase, compositional model to simulate the LNAPL distribution and resulting contaminant emissions, whereby the geologic heterogeneity, transient flow conditions and non-equilibrium dissolution factors can be explicitly considered. However, the sensitivity of such models to the spatial distribution of the controlling parameters in heterogeneous aquifers limits their use for deterministic applications unless extensive field data are available. In two-dimensional cross-sectional multiphase modeling studies carried out at the site of a crude oil spill, Essaid et al. (1993) and Dillard et al. (1997) were able to reproduce general large-scale features of the observed oil body, but they had only limited success in reproducing local oil saturations and highlighted the importance of accounting for the uncertainty in the hydrogeological parameter values. In most cases, the necessary degree of site characterization and model grid resolution required to adequately resolve the details of the temporal and spatial variability of multiphase flow processes would render the deterministic approach problematic. Essaid and Hess (1993), on the other hand, presented a stochastic modelling study of oil infiltration into a hypothetical glacial outwash aquifer by performing a series of Monte Carlo simulations with different spatial permeability distributions in a two-dimensional cross section. Their results showed that while the use of mean hydraulic properties reproduced the ensemble mean oil saturations, the saturation patterns between the individual realizations varied considerably from the mean, with localized oil saturations being considerably higher than those obtained using uniform mean properties as input. Kueper and Gerhard (1995) modelled DNAPL infiltration in a two-dimensional two-phase flow system for multiple realizations of a spatially-variable permeability field, and similarly observed large variations in the resulting DNAPL distribution between the different realizations. In a numerical study examining the effects of porous medium heterogeneity on NAPL dissolution, Mayer and Miller (1996) demonstrated that the physical aquifer heterogeneity and the spatial distribution of the residual NAPL are important factors affecting the NAPL dissolution process. They concluded that, while equilibrium dissolution predominates in relatively homogeneous porous media, kinetically controlled dissolution may be more important in heterogeneous aquifers.

For a typical case involving an LNAPL spill in a sand or gravel aquifer, of which TL2 is an example, the lateral extent of the LNAPL body in the subsurface at the site can be delineated in a straightforward manner and with reasonable accuracy, either from the

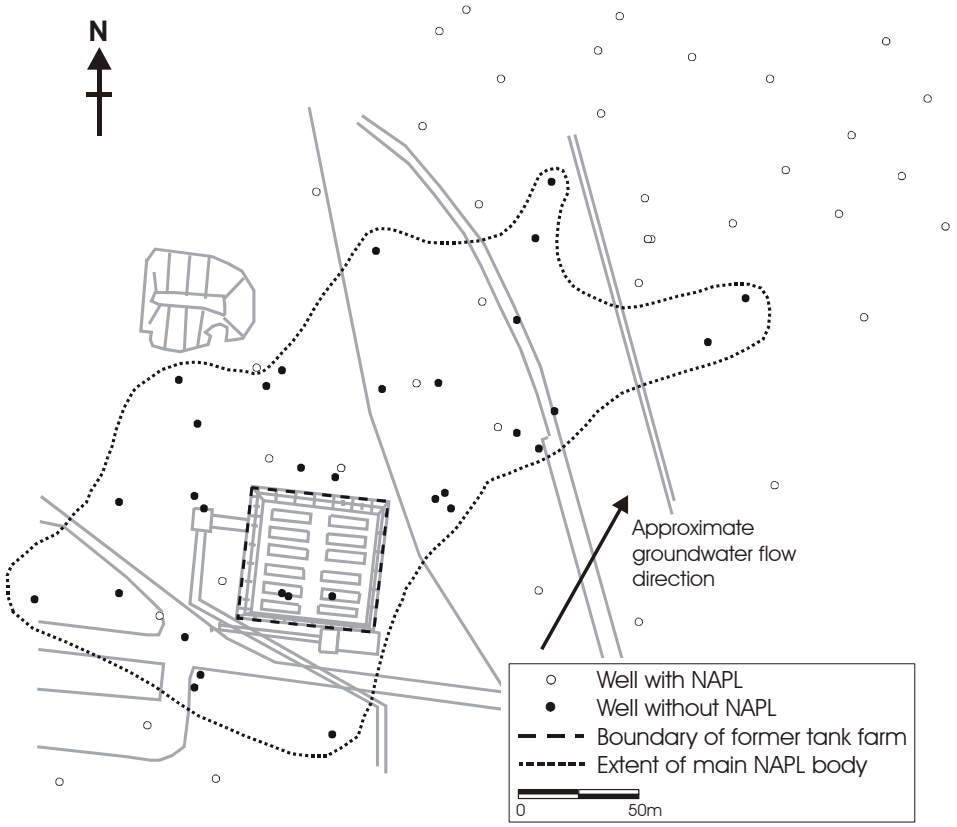

Figure 4.1 Field site Tanklager 2, Flughafen Niedergoersdorf (TL2), showing groundwater monitoring wells, the location of the former tankfarm and the assumed extent of NAPL phase in the subsurface.

presence of LNAPL phase in wells screened across the capillary fringe or by using technologies such as ROST© (Rapid Optical Screening Tool) (USEPA, 1997). The distribution of the LNAPL in terms of actual saturation values in the pore space is, however, much more difficult to determine directly. Thus determining a relationship between the extent of the LNAPL body and the contaminant emission, and furthermore identifying the salient parameters controlling the relationship, represents a useful step in developing a simple, practicable method for the estimation of contaminant emission. A three-dimensional, multiphase modelling approach is used at TL2 to simulate LNAPL infiltration and spreading in the capillary fringe and the resulting contaminant emission. The numerical model simulations allow for multiphase flow, kinetically-controlled LNAPL dissolution and aqueous-phase transport. Multiple realisations of heterogeneous permeability and porosity distributions, as well as the effect of fluctuating watertable levels, are considered in the analysis.

4.2. Site description

TL2, shown in Figure 4.1 is the second of the two former tankfarm study sites at Flughafen Niedergörsdorf (see section 3.2), and lies at the eastern end of the main runway. In total, the site represents an area of approximately 4 hectares. The tankfarm itself consisted of a number of above-ground storage tanks on an unsealed sandy surface. The subsurface at TL2 is heavily contaminated with the kerosene that was stored there, and while little is known about the historical circumstances of the contamination, it is thought to have occurred over a number of years within the area of the tankfarm itself or adjacent fuel transfer points. The approximate extent of the main LNAPL body, which based on occurrence of kerosene in monitoring wells at the site covers about 3 hectares, is shown in Figure 4.1.

The depth to the water table at the site is approximately 15 meters. The general groundwater flow direction is from south-west to north-east with the average linear groundwater velocity being in the order of 10 m/yr. Hydraulic conductivities are in the region of 10^{-5} m/s, with the hydraulic gradient being about 0.005.

4.3. Model description and governing equations

Following the work of Unger et al. (1998) and Forsyth et al. (1998), the three-dimensional, three-phase compositional model CompFlow is applied to simulate LNAPL distributions and contaminant emissions to the aqueous phase for multiple realisations of heterogeneous parameter distributions at the field site. A number of experimental and numerical studies have been reported on in the literature regarding the formulation of mass transfer mechanisms describing kinetic NAPL dissolution in groundwater (Berglund, 1997; Frind et al., 1999; Mayer and Miller, 1996; Unger et al., 1998). The governing equations describing multiphase flow and aqueous-phase transport, which are described comprehensively in the aforementioned publications, are covered briefly here. It should be noted that while the general form of the CompFlow model considers three actively flowing phases with component partitioning between all phases, here only two active flowing phases (i.e., aqueous and non-aqueous) will be considered because the gas phase is assumed to be passive; contaminant diffusion in the gas phase is similarly neglected in this case. The contaminant, kerosene, is considered as a single LNAPL component.

For a multiphase compositional model, the water conservation equation is as follows:

$$\frac{\partial}{\partial t}\left[\phi S_q M_q X_{wq}\right] = \nabla \cdot \left(M_q X_{wq} V_q\right) + q_w \tag{4.1}$$

while for the case of coupled multiphase flow and kinetic dissolution of a NAPL, contaminant conservation requires separate equations describing the moles of contaminant in the aqueous and non-aqueous phases as follows:

$$\frac{\partial}{\partial t}\left[\phi S_q M_q X_{cq}\right] = R_{c_{nq}} - A_c - \nabla \cdot \left(M_q X_{cq} V_q\right) + \nabla \cdot \left(\phi S_q D_{cq} M_q \nabla X_{cq}\right) + q_{cq} \tag{4.2}$$

$$\frac{\partial}{\partial t}\left[\phi S_n M_n\right] = -R_{c_{nq}} - \nabla \cdot \left(M_n V_n\right) + q_{cn} \tag{4.3}$$

where Φ is the porosity, S_q and S_n are respectively the saturations of the aqueous and NAPL phases in the pore volume, M_q and M_n are the molar densities of the aqueous and NAPL phases (mol m^{-3}), X_{wq} and X_{cq} are the mole fractions of water and contaminant in the aqueous phase, V_q and V_n are the Darcy fluxes of the aqueous and NAPL phases (m s^{-1}), D_{cq} is the aqueous phase hydrodynamic dispersion coefficient for the contaminant (m^2 s^{-1}) and q_w, q_{cq} and q_{cn} source/sink terms for water and contaminant in the respective phases. A_c is a reaction rate term representing sorption/desorption of the contaminant onto the solid phase, given by:

$$A_c = \lambda_A \left(\rho_b K_d M_q X_{cq} - A_c\right) \tag{4.4}$$

while $R_{c_{nq}}$ is the dissolution rate for the contaminant from the non-aqueous into the aqueous-phase (see equations 2.9 and 2.10).

A control volume finite element (CVFE) discretisation is employed in the numerical solution of Equations (4.1) to (4.3), together with fully-implicit temporal weighting. The details of the numerical formulation including mesh generation, use of a MUSCL-type flux limiter to control numerical dispersion and primary-variable switching to enhance nonlinear iteration convergence can be found in Forsyth et al. (1998). The large, sparse Jacobian matrix is solved using ILU factorisation after linearization by Newton-Raphson iteration (Unger et al., 1996). A more detailed description of the numerical solution of the compositional multiphase flow equations are discussed in Unger et al. (1996; 1998) and Forsyth et al. (1998).

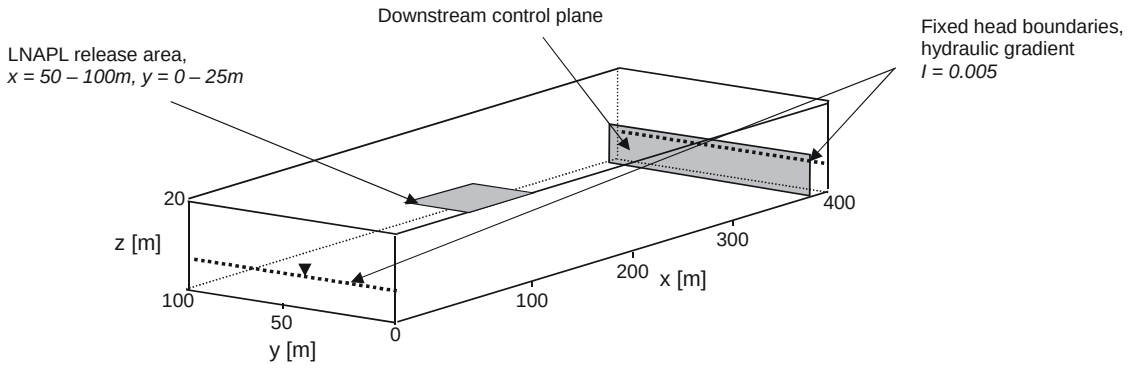

Figure 4.2 Three-dimensional computational domain for the unsaturated and saturated zone. Groundwater flow is in the x-direction.

4.4.Model setup

Figure 4.2 shows the three-dimensional model domain based on the situation at TL2. The domain is oriented with the x-axis coincident with the groundwater flow direction and the z-axis vertically. To reduce computational demands, a symmetry boundary is assumed and a 400m × 100m × 20m domain representing one half of the site is used, with the plane $y = 0.0m$ bisecting the site and the tankfarm area. Hydrostatic head conditions are used for the upstream and downstream boundaries to produce an unsaturated zone thickness of about 15 m and horizontal hydraulic gradient of 0.005 along the domain in the x-direction, values representative for the site. The planes located at $y = 0.0m$ and $y = 100.0m$ as well as the lower surface are considered to be no-flow boundaries. A constant aqueous-phase flux is applied to the upper surface of the domain to simulate infiltration. A vertical control plane is assigned adjacent to the downstream boundary, perpendicular to the flow direction. The grid used for the model domain contains 40 × 20 × 77 nodes (in the *x-, y-* and *z-* directions, respectively, for a total of 61,600 nodes), with constant spacing in the *x-* and *y-* directions and variable node spacing in the *z-* direction, whereby the z-cell size was reduced by a factor of 10 from 0.5m to 0.05m over a 2m region in order to achieve an accurate definition of the capillary fringe where large changes in capillary pressures and phase saturations occur over a small vertical interval. While the vertical refinement was found to be necessary to prevent numerical problems in the simulations, it was found that a relatively large lateral node spacing in the *x-* and *y-*dimensions produced acceptable results. Although the NAPL spreading is sensitive to the lateral node spacing, with an increased spreading for smaller node spacing, the dissolution components of the COMPFLOW code are less sensitive (Unger et al., 1998). Thus for the approach used here, where emission to the aqueous phase

Table 4.1 Summary of simulation scenarios.

Section / Parameter	4.5.1.1		4.5.1.2		4.5.2		4.5.2	
Hydraulic conditions	Steady state		Groundwater fluctuation, $\Delta h = 0.5m$		Steady state		Steady state	
Permeability & porosity distribution	Homogeneous		Homogeneous		Heterogeneous		Heterogeneous	
	K	Φ	K	Φ	Mean K	Mean Φ	Mean K	Mean Φ
	5×10^{-12} m^2	0.33	5×10^{-12} m^2	0.33	5×10^{-12} m^2	0.33	1.1×10^{-11} m^2 1.7×10^{-11} m^2	0.33 0.33
Groundwater recharge	120 mm/yr		120 mm/yr		120 mm/yr 180 mm/yr 240 mm/yr		120 mm/yr	

is compared to the lateral area of the NAPL body, a fairly large node spacing could be used, keeping computational demands for the simulations manageable. The suitability of the node spacing was confirmed by including a scenario with an increased grid refinement in the suite of heterogeneous simulations presented in Section 4.5.2. A number of scenarios, summarised in Table 4.1 and described in detail below, were simulated to evaluate the effects of various factors on the LNAPL distribution in the subsurface and the resulting emissions to groundwater. All simulation scenarios begin with an initial spin-up period of 2 years to allow the water table to reach an equilibrium condition. This is followed by a 10-year period of LNAPL injection. Based on the current estimated volume of kerosene in the subsurface, obtained from the observed thickness of kerosene phase in monitoring wells using the SPILLVOL code (ESTI, 1990b), 3000m³ of LNAPL is introduced at a constant rate and evenly distributed over a 50m × 25m area of the upper surface of the domain corresponding to the former tank farm. This is followed by a further period of LNAPL redistribution and, depending on the scenario, a subsequent temporal variation of the groundwater flow boundary conditions. Because the focus of this work is on the LNAPL source-zone distribution and contaminant emissions to the aqueous phase, contaminant partitioning to the gas phase, sorption and biodegradation processes in the aqueous phase are not considered. The various soil and LNAPL properties used in the simulations are given in Table 4.2, while data for the relative permeability-saturation-pressure relationships for the NAPL-water and NAPL-water-gas systems are given in Table 4.3. The soil physical properties used are average values measured on soil samples taken from the site, with the

van Genuchten parameters being estimated from particle size distributions using the SOILPROP code (ESTI, 1990a). Published values for kerosene are used for the interfacial tensions and viscosity in the simulations, while the remaining properties assigned to the single-component LNAPL are mole-fraction-weighted average values for compounds defined in an analysis of a kerosene sample taken from a monitoring well at TL2. The use of composite components with weighted average properties has been shown to be an effective method for simplifying complex LNAPL mixtures for representation in numerical simulations (Gaganis et al., 2002) and is an alternative to the approach used by Kim and Corapcioglu (2002), who in multiphase simulations of LNAPL migration and dissolution considered kerosene as a single component with the properties of the most soluble compound present in the mixture. Reducing the complex LNAPL mixture to a single component neglects the time-varying effective solubility of the individual components and thus the time-varying nature of the averaged effective solubility. Hence the model neglects changes in contaminant emission that are known to arise from the changing composition of a NAPL mixture over time (Eberhardt and Grathwohl, 2002; Frind et al., 1999; Gaganis et al., 2002) and which would lead to an overall decrease in emission over time as the more soluble components of the LNAPL mixture became depleted. However, for a large-scale contamination such as the one considered here, due to the large amount of LNAPL present the change in the composition is likely to be relatively slow. Multi-component simulations of the dissolution and volatilisation of kerosene carried out for TL1 indicate a timescale in the order of decades for significant changes in the molar fractions, and hence effective solubilities, of the most soluble components (TEX, trimethylbenzenes and ethyl-toluenes) (Miles, 2003). These compounds constitute only a small fraction, less than ten percent, of the kerosene mixture, but due to their relatively high solubility are the most significant in terms of the mole-fraction-weighted average solubility. As the approach described here is intended to consider only the current or short-term future emission from the source zone, this simplified representation of the NAPL mixture is considered to be sufficient. The aqueous diffusion coefficient for the dissolved LNAPL was calculated according to the method of Worch (1993) (Equation 2.19), while estimated values were used for the dispersivities.

In the analysis of the simulation results, two quantities are considered. These are the contaminant emission to the aqueous phase and the surface area of the LNAPL body. The emission to the aqueous phase in the scenarios is regarded here as the total mass flux (i.e., advective plus dispersive) of dissolved LNAPL passing the downstream control plane

Table 4.2 Physico-chemical parameters used in the multiphase flow and transport simulations.

Variable and Abbreviation	Parameter value and Unit
LNAPL molar density M_n	5.9×10^3 mole/m³
LNAPL molar mass Wt_n	134.9×10^{-3} kg/mole
Aqueous solubility of NAPL X_n	3.5×10^{-6} mole/mole H_20 (26.4 mg/l)
Viscosity of LNAPL μ_n	1.7 cp
Kinetic dissolution parameters λ, β	2.0 day^{-1}, 0.5[(1)]
Interfacial tension air/water σ_{aw}	75 dynes/cm
Interfacial tension oil/water σ_{ow}	48 dynes/cm[(2)]
Interfacial tension air/oil σ_{ao}	27.5 dynes/cm[(2)]
Permeabilities $k_x = k_y = k_z$	5×10^{-12} m^2
Porosity Φ	0.33
Dispersivity (longitudinal) α_L	1 m
Dispersivity (transverse horizontal) α_{TH}	0.1 m
Dispersivity (transverse vertical) α_{TV}	0.01 m
Aqueous phase diffusion coefficient D_{cq}	4×10^{-6} m^2/day
van Genuchten parameter α	4.28 m^{-1}
van Genuchten parameter n	2.07
Residual water saturation S_w*	0.05

[1] from (Unger et al., 1998), and (Frind et al., 1999). [2] Irwin et al. (1997)

Table 4.3 Relative permeability and capillary pressure-saturation data for the NAPL-water and liquid-(NAPL+water) gas phases. The subscripts *n, q* and *g* refer to NAPL, water and gas respectively.

Oil-water				Liquid-gas				
S_q	K_{rq}	K_{rn}	P_{cnq} (kPa)	S_n+S_q	K_{rg}	K_{rn}	P_{cng} (kPa)	P_{cqg} (kPa)
0.05	0	1	150.0	0.05	0.97	0.000	150.0	150.0
0.1	0.001	0.972	24.1	0.1	0.94	0.000	13.8	37.6
0.2	0.009	0.898	8.5	0.2	0.86	0.000	4.9	13.3
0.3	0.031	0.805	5.2	0.3	0.74	0.001	2.7	7.4
0.4	0.086	0.668	3.4	0.4	0.63	0.004	1.9	5.3
0.5	0.156	0.548	2.6	0.5	0.52	0.012	1.5	4.0
0.6	0.251	0.422	2.0	0.6	0.40	0.029	1.2	3.1
0.7	0.374	0.297	1.6	0.7	0.28	0.064	0.9	2.4
0.8	0.572	0.151	1.1	0.8	0.14	0.156	0.6	1.7
0.9	0.768	0.055	0.7	0.9	0.05	0.322	0.4	1.1

normal to the groundwater flow direction in the model domain. The surface area of the phase body considered here is calculated as the *lateral projected area* (i.e., the surface area as viewed vertically from above or below) of all model cells having an LNAPL saturation, S_n, equal to or greater than a specified value.

4.5. Results and discussion

4.5.1. Homogeneous Aquifer Scenarios

4.5.1.1. Homogeneous Base Case

For the "Base Case" scenario, a homogeneous subsurface is considered, with the initial two-year period of equilibration followed by a 10-year LNAPL release period where a total of 3000m³ of LNAPL is injected, evenly distributed over the 25m × 50m portion of the domain upper surface representing the former tankfarm area, as described earlier. The simulation was then conducted for a further 30 years during which the LNAPL migrates and redistributes. Figure 4.3 a-c show the LNAPL saturation distributions in the model domain at three different times during the simulation. Two different saturation isosurfaces are shown; one for S_n = 0.01, which represents the maximum extent of the LNAPL body, the other for S_n = 0.4, which depicts the core of the LNAPL zone. The temporal evolution of the surface area of the LNAPL body, as defined by a saturation S_n > 0.01, is shown in Figure 4.3(d), along with the calculated aqueous-phase mass flux crossing the downstream control plane (expressed as moles of dissolved LNAPL per day). Following its release at the upper surface of the domain, the LNAPL moves vertically downwards and collects at the capillary fringe, as can be seen from the S_n = 0.4 isosurface. A portion of the NAPL then spreads laterally over the capillary fringe, giving rise to the classic "pancake" shape and reaches its maximum extent about 30 years after the start of the release. It can be clearly seen that the aqueous-phase mass flux crossing the downstream control plane closely follows the temporal development of the lateral extent of the LNAPL body in contact with the capillary fringe. As the LNAPL travels vertically downwards below the injection area, there is effectively no lateral spreading and the LNAPL area is constant and equal to the release-zone area. The emission to the groundwater, however, begins to increase as vertical advective and dispersive transport due to infiltration carries the aqueous-phase contaminant ahead of the advancing LNAPL front. As the LNAPL spreads laterally in the zone of water saturation, the emission clearly increases in proportion with the LNAPL body area, except for the early-time offset due to the combined effect of the initial spreading phase of the LNAPL pancake and the contaminant travel time to the downstream control plane. As the NAPL spreading slows and reaches a maximum, the emission likewise reaches a steady state.

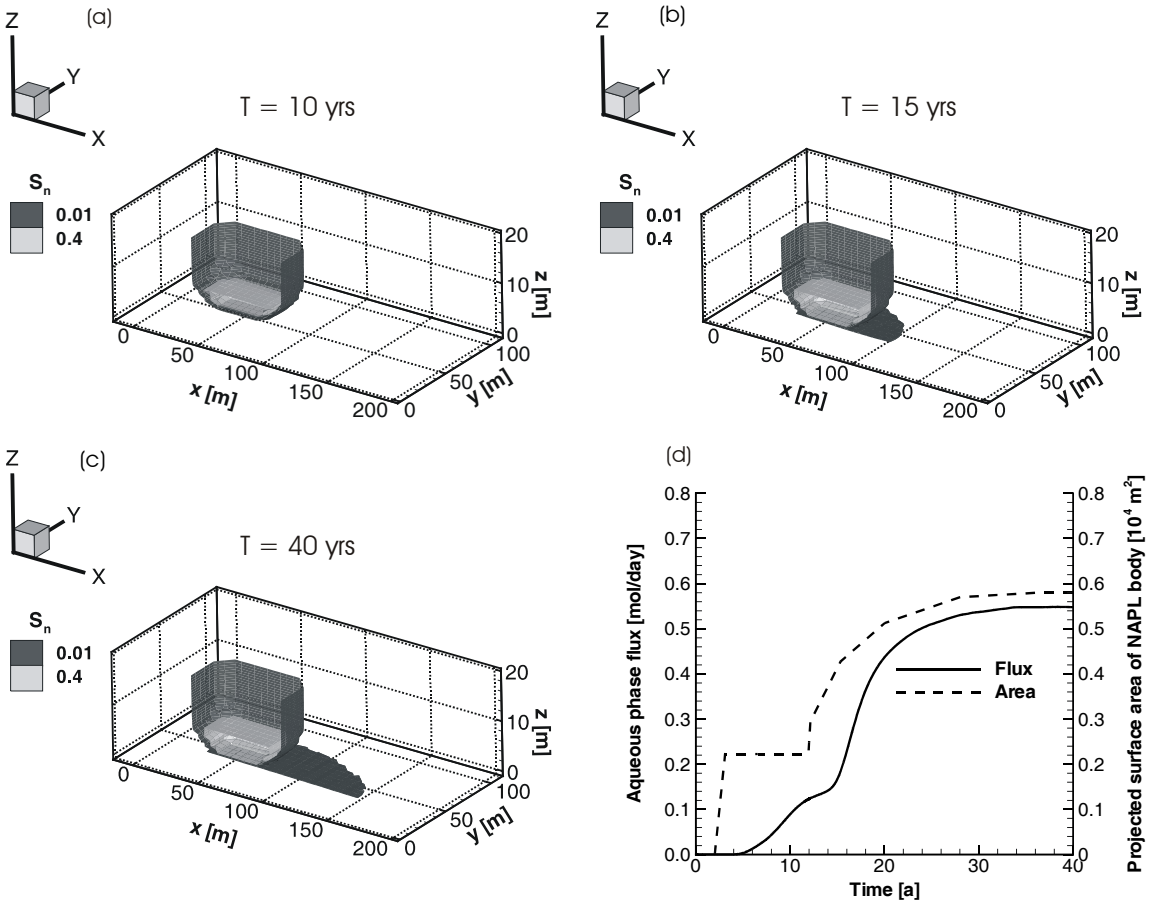

Figure 4.3 (a), (b) and (c): Simulated LNAPL distribution for the homogeneous case shown as isosurfaces for LNAPL saturation, S_n = 0.01 and S_n = 0.4 at different times, (d) projected LNAPL body surface area for S_o > 0.01 and the downstream aqueous-phase mass flux versus time.

4.5.1.2.The Effect of Watertable Fluctuations

To demonstrate the potential effect of fluctuations in the water table elevation on the distribution of the LNAPL saturations and the contaminant emission to the aqueous phase, we begin with the situation after 40 years in the base case simulation, where the LNAPL distribution and the emission is at steady state. The upstream and downstream prescribed head boundary conditions are altered simultaneously, causing the water table to first fall by 0.5m and then rise back to its original position while keeping the average hydraulic gradient across the model domain constant. The boundary heads are changed linearly over a period of 4 years, reflecting the observed medium-term changes in hydraulic conditions at the site. Figure 4.4 shows the effect of this change in the hydraulic conditions on the LNAPL distribution and the downstream mass flux crossing the control plane in the aqueous phase. As the water table moves downwards, the main LNAPL body, represented here by the S_n = 0.4 isosurface, is remobilised by the change in water pressure and follows the water table

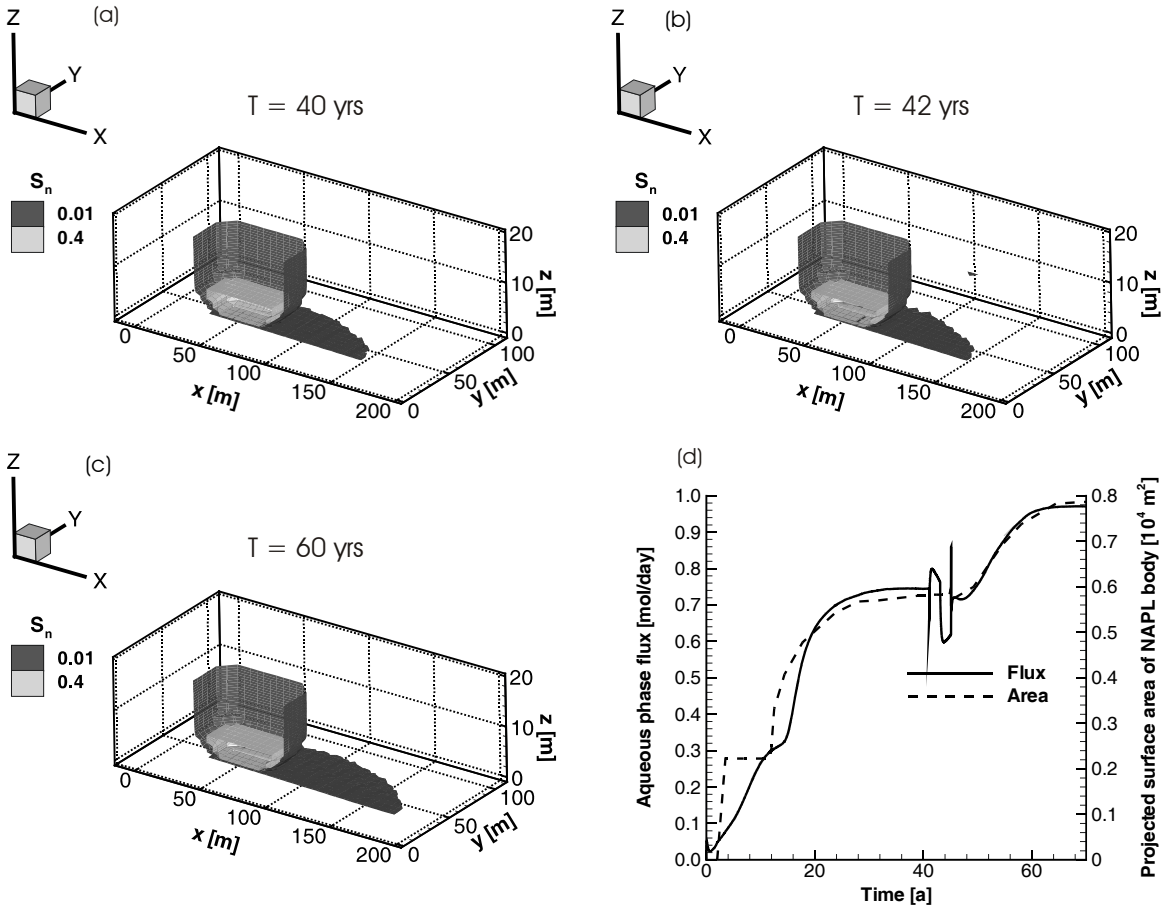

Figure 4.4 The effect of groundwater fluctuations on the steady-state LNAPL distribution for the homogeneous case. The simulated LNAPL distribution is shown as isosurfaces for LNAPL saturation, S_n = 0.01 and S_n = 0.4 at three different times; (a) T = 40 years, initial steady state, (b) T = 42 years with water level dropped by 0.5m over 2 years and (c) T = 60 years with water level returned to original position over a further 2 years and a subsequent redistribution of LNAPL. (d) projected LNAPL body surface area for S_o > 0.01 and the downstream aqueous-phase mass flux versus time.

downwards. As the movement of the groundwater table is reversed and it begins to move upwards to return to its original level, the pressure of the water displaces the LNAPL from this new position, causing a renewed lateral spreading and a corresponding increase in the contaminant emission at the control plane. The rapid fluctuations that occur in the aqueous-phase contaminant flux across the control plane are caused by the sudden changes in the prescribed head at the downstream boundary due to the changes in the local flow system near this boundary, but these have no significant effect on the overall, long-term results. Once again, the changes in the areal extent of the LNAPL body correlate closely with the changes in the aqueous-phase emissions, especially in the long term.

4.5.2. Heterogeneous Aquifer Scenarios

Heterogeneous permeability and porosity distributions were generated using the Fourier transform method described by Robin et al. (1993). The geometric and arithmetic mean permeability and porosity values of the random fields, equal to 5×10^{-12} m^2 and 0.33, respectively, are identical to those values used in the homogeneous "Base Case" scenario. Standard deviations for the input log-permeability and porosity, $\sigma_{lnK} = 0.6$ and $\sigma_{por} = 0.02$, and correlation lengths of 10m, 10m and 1m in the *x*-, *y*- and *z*- directions respectively were estimated for the site. The Leverett J-Function (Leverett, 1941) was applied in the simulations to individually scale the nodal capillary pressure relationships according to the synthetically-generated individual permeability and porosity lenses. The domain node spacing was increased to 10m in the *x*-direction to accommodate an increase in the LNAPL spreading compared to the homogeneous case. The scenarios were otherwise identical to the homogeneous base case. Simulations were initially run for 20 different permeability and porosity realizations, the aim being to quantify the effect of heterogeneity on the LNAPL body size *versus* aqueous-phase emissions at the control plane for a moderate number of realisations. The simulations demonstrate that geologic heterogeneity has a very significant impact on the LNAPL spreading, with the geostatistically equivalent realizations producing widely varying LNAPL distributions and source zone emissions. This can clearly be seen in

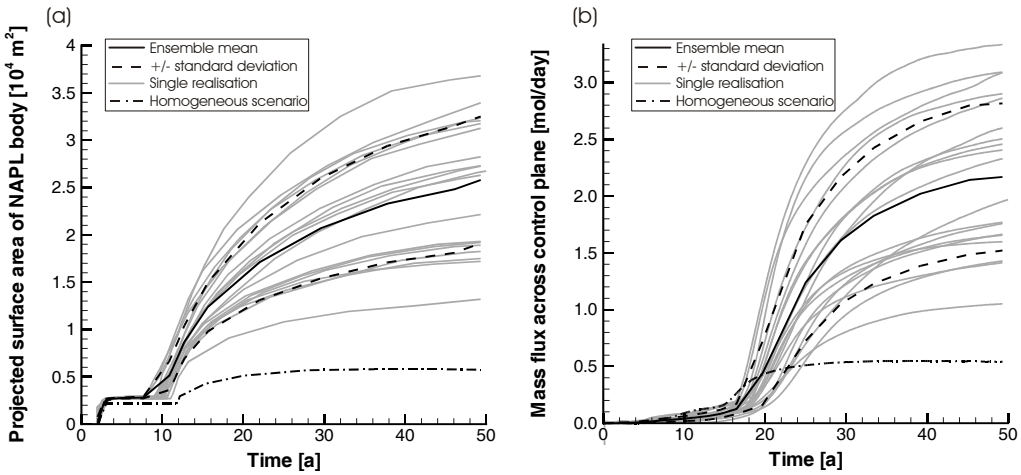

Figure 4.5 (a) LNAPL body surface area for $S_n > 0.01$ and (b) aqueous-phase mass flux crossing the downstream control plane for 20 realizations of heterogeneous permeability and porosity distributions, together with the ensemble means and standard deviations. Results for the homogeneous case are also included.

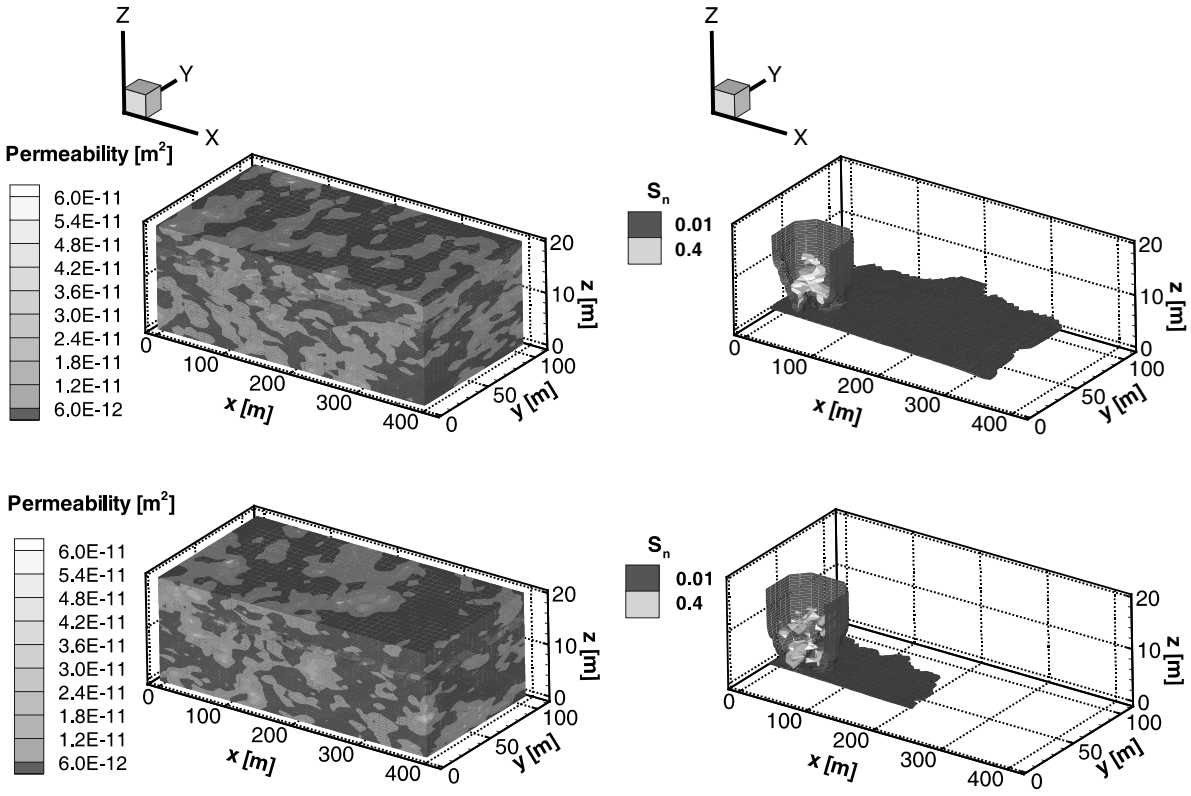

Figure 4.6 Heterogeneous permeability pattern and final distribution of LNAPL as isosurfaces for S_n = 0.01 and S_n = 0.4, for the heterogeneous case producing the minimum and maximum LNAPL spreading.

Figure 4.5, which shows plots of the LNAPL-body surface area for $S_n > 0.01$ and the downstream aqueous-phase mass fluxes for each of the individual realizations, together with the ensemble means and standard deviations in each case (keeping in mind that the standard deviation estimates are based on a limited sample size of 20 realizations). As well as affecting the mobility of the LNAPL, the heterogeneity leads to different volumes being retained in the unsaturated zone as the LNAPL migrates vertically downward to the capillary fringe, which means that the volume of LNAPL reaching the water table, and hence the volume migrating laterally to form the pancake, varies significantly between the realisations, and results in all cases in a larger LNAPL body than in the homogeneous case. This can also be seen in Figure 4.6, which shows the final distribution of LNAPL, once again as isosurfaces for $S_n = 0.01$ and $S_n = 0.4$, for the realizations exhibiting the minimum and maximum LNAPL spreading. This also serves to highlight the impact on the distribution of the LNAPL arising from the heterogeneity.

In order to examine the effect of different groundwater recharge infiltration rates, the scenarios described above were repeated using the same permeability and porosity

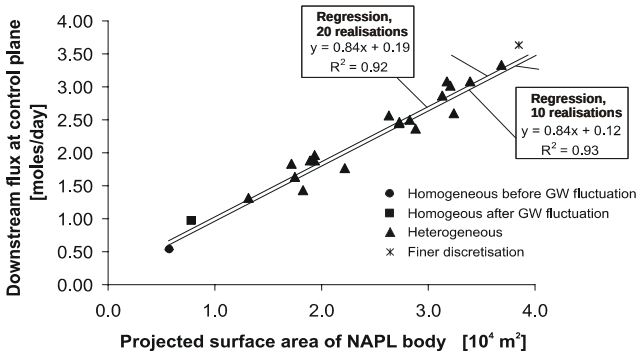

Figure 4.7 Aqueous-phase mass flux crossing the downstream control plane versus LNAPL body surface area ($S_n > 0.01$) at time $T = T_{max}$ for different heterogeneous permeability and porosity distributions, as well as for the homogeneous scenario before and after groundwater fluctuation. Two linear regressions are shown; one for the full dataset of 20 heterogeneous realisations, the other for a subset of 10 realisations.

distributions but with altered infiltration rates, increasing the values from 120 mm/yr to 180 mm/yr and to 240 mm/yr. To illustrate the effect of the different mean permeability values, an additional two sets of heterogeneous permeability and porosity distributions were synthesized using the same geostatistical parameters as before, but with different mean permeabilities given by $K = 1.1 \times 10^{-11}$ and 1.7×10^{-11} m^2, respectively. Although the details of these results will not be presented here, the findings will be incorporated in the derived areal LNAPL-extent *versus* aqueous-phase contaminant emission relationships presented below.

4.5.3. Derived LNAPL-extent Aqueous-phase Mass Flux Relationships

In order to elucidate the relationship between the areal LNAPL distribution and the contaminant emission across the control plane for the different realizations, the downstream aqueous-phase mass flux is plotted as a function of the LNAPL body surface areas (defined as $S_n > 0.01$) in Figure 4.7 for each of the 20 heterogeneous realizations at time $T = T_{max}$ (i.e., when the LNAPL has spread to its maximum extent). The figure demonstrates that a linear relationship clearly exists between the source zone area and the emission, with $R^2 = 0.92$. Included in the diagram are the results for the homogeneous scenario before and after the groundwater table fluctuation, as well as a scenario with an increased grid refinement for one heterogeneous realisation, with node spacing reduced to 5m in x and y. These cases fit comfortably within the linear relationship determined for the 20 heterogeneous realisations, indicating that for the permeability and porosity distributions

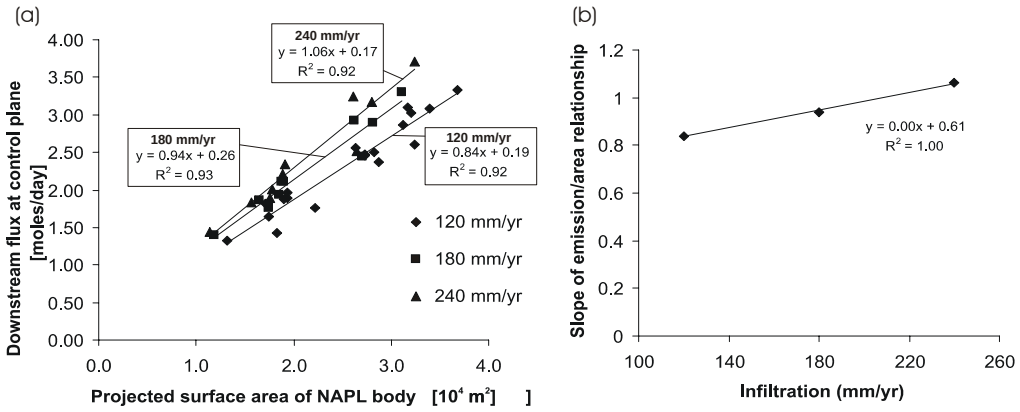

Figure 4.8 (a) Aqueous-phase mass flux across the downstream control plane versus LNAPL body surface area ($S_n > 0.01$) at time $T = T_{max}$ for different heterogeneous permeability and porosity distributions with different rates of infiltration. The homogeneous cases are also included for the 120mm/yr infiltration (b) Relationship between infiltration rate and the slope of the correlation equations in (a).

simulated the relationship is relatively independent of the degree of heterogeneity, and that the lateral grid spacing used in the simulations is adequate for the purpose of deriving the relationship. A second linear fit is shown for a subset of 10 realisations, for which the relationship parameters (slope and intercept) and R^2 are almost identical. On this basis, 10 realisations were used in each case for the derivation of the relationships for different infiltration rates and mean permeabilities. Figure 4.8 shows the results for the different rates of water infiltration for each of the heterogeneous scenarios, once again expressed as aqueous-phase mass flux at the control plane versus lateral areal extent of the LNAPL body at time $T = T_{max}$. In Figure 4.8(a) a linear relationship between the LNAPL-body surface area and the aqueous-phase emission is seen for all three rates of infiltration. In Figure 4.8(b) the slope of the linear relationship is plotted against the infiltration rate, whereby it can be seen that the slope is a linear function of infiltration values ($R^2 = 1.0$).

For the large site-scale LNAPL pools in the simulations, linear relationships could be established between the projected surface area of the NAPL pool and contaminant emission to the aqueous phase, with the parameters of the relationships (slope and intercept) related to the infiltration rates and mean permeabilities in the respective sets of simulations. The non-zero values for the intercepts of the linear relationships, however, imply that for small pool areas the relationship becomes non-linear. If the mass transfer to the aqueous phase from the LNAPL source is considered to essentially arise from three main processes; dissolution due

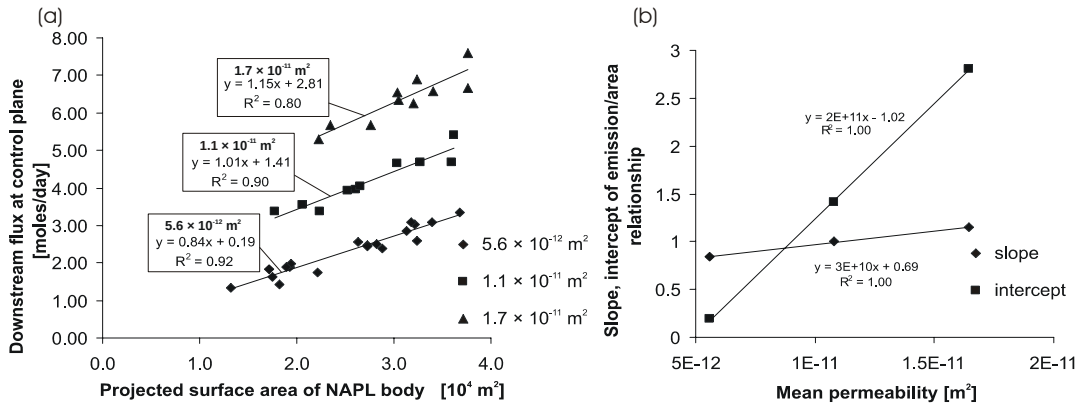

Figure 4.9 (a) Aqueous-phase mass flux crossing the downstream control plane versus LNAPL body surface area ($S_n > 0.01$) at time $T = T_{max}$ for different heterogeneous permeability and porosity distributions with different mean permeabilities. The homogeneous cases are also included with mean permeability = 5.6×10^{-12} (b) Relationship between mean permeability and the slope and intercept of the correlation equations in (a).

to the horizontal flow of groundwater in the saturated zone below the LNAPL body, dissolution due to vertical flow of infiltration water through the source zone and diffusive transfer of the dissolved LNAPL vertically to the groundwater below the LNAPL body, then the relationship between the lateral surface area and the emission can be reasonably explained. For small-scale NAPL pools, Chrysikopoulos et al. (2003) showed that the overall mass flux to the aqueous phase (neglecting groundwater infiltration) for groundwater flowing past a NAPL pool is a function of both the pool length in the direction of groundwater flow and the flow velocity; for a constant pool length there is a more or less linear increase in mass transfer as flow velocity increases, while for a constant flow velocity the mass transfer at first increases as the pool length increases, then tends to a constant value. Uncontaminated water flowing through an LNAPL source zone, on the other hand, will reach the aqueous-phase solubility for dissolved contaminants within a short distance, a length scale which is on the order of a few pore lengths (Grathwohl, 1998). Thus the dissolution and advective mass flux of aqueous-phase contaminants from the source zone for a given flow rate and LNAPL component solubility will be a function of the source zone surface area normal to the flow direction. For groundwater flowing horizontally through the LNAPL source zone, this means that changes in the length of the source zone in the direction of groundwater flow will be of little consequence to the mass transfer rate, as after a relatively short distance the maximum concentration occurring in the groundwater, and hence the maximum emission, will be achieved. Changes in the width perpendicular to the flow direction and thickness of the source zone will, however, have some effect on the mass

transfer, in that an increase in either will lead to a corresponding increase in the surface area of the LNAPL body exposed to the horizontally flowing groundwater. Vertically flowing infiltration, on the other hand, is exposed to a far greater source-zone area and a change in this area will cause a corresponding change in the capacity for dissolution and hence the emission.

Thus for the relationships described here, derived for large LNAPL pools, the dissolution and advective mass flux due to groundwater infiltration is largely responsible for the linear nature of the area-emission relationships, with the infiltration rate affecting the slope of the relationship (Figure 4.8(b)). The value of the intercept reflects the maximum mass transfer coefficient for water flowing past the LNAPL pool, which would be reached at pool sizes well below those considered in the simulations, and is seen in Figure 4.9(b) to be a linear function of the mean permeability (i.e. the horizontal groundwater flow velocity). An additional dependence of the slope of the relationship on the mean permeability is also seen in Figure 4.9(b), probably because an increase in the horizontal flow rate leads to steeper vertical concentration gradients below the source zone, and hence an increase in the diffusive transport between the source zone and the bulk flowing groundwater.

4.6. Summary and Conclusions

The homogeneous case described in Section 4.5.1.1 shows that for this simple case the simulated development of the LNAPL spill follows the expected pattern, with an LNAPL pool developing on the water table, and with more of the spreading occurring in the direction of groundwater flow than laterally. Following the release, the LNAPL body eventually stabilizes provided that the groundwater flow system is steady. It was also demonstrated that the contaminant emission to the aqueous phase is closely linked to the projected lateral surface area of the LNAPL body. A change in the hydraulic conditions in the aquifer, as described in 4.5.1.2, can also lead to a remobilisation and redistribution of the LNAPL, a phenomenon that is known to occur in the field. The redistribution of the LNAPL leads to an increase in the emission to the aqueous phase due to the induced change in the surface area of the LNAPL body. Simulations performed using geostatistically-generated heterogeneous distributions of permeability and porosity, described in section 4.5.2, show a linear relationship between the surface area of the LNAPL body and the emission of contaminants to the aqueous phase, which is independent of the source-zone thickness and the erratic distribution of the LNAPL saturations in the source zone. In all cases the LNAPL spreading was greater in the simulations with heterogeneous parameter distributions than in

the homogeneous base case, principally because less LNAPL was retained in the unsaturated zone during infiltration, causing a greater volume to reach the capillary fringe and spread laterally.

The heterogeneous scenarios described in 4.5.2 demonstrate the sensitivity of the LNAPL spreading to the subsurface heterogeneity and illustrate the problematic nature of applying a multiphase modelling approach to deterministically simulate the observed LNAPL distribution and contaminant emission at a field site, where hydraulic conditions vary over time and data on LNAPL quantities and distributions, soil properties, geology and hydrogeology are generally sparse. In contrast, the derived relationship between the LNAPL surface area and emission to the aqueous phase suggests the applicability of a relatively simple correlation approach. The parameters of the linear relationship are site specific, being dependent primarily on the bulk aquifer permeability and horizontal hydraulic gradients, average infiltration rates and the physico-chemical properties of the contaminants. Once such a relationship has been determined, the aqueous-phase emission from the source zone can be estimated from the known lateral area of the LNAPL body. This type of correlation analysis only requires knowledge of bulk average parameters that can be estimated by means of viable, cost-effective field studies. A further advantage of using the type of relationships developed here is that it is not necessary to know the precise quantity of LNAPL spilled or its spatial distribution in terms of saturation values in order to estimate the contaminant emission.

5. Case Study 3: Flughafen Brand

5.1. Introduction

The former tankfarm at Flughafen Brand is considered as an example of the Type 3 LNAPL contamination defined in Section 1, with a relatively stable floating LNAPL pool spread over a wide area and an extensive and well established contaminant plume. The aim of the modelling study for Brand was a detailed investigation of the degradation processes in the contaminant plume to develop a prognosis for the implementation of MNA. The site is particularly well characterised, with high-resolution data both for the site geology and contaminant distributions obtained from direct-push surveys, and concentration data from multi-level groundwater sampling in a dense network of monitoring wells. With the ongoing development and improvement of geological and hydrogeological investigation methods such high-resolution datasets are becoming increasingly common, calling for an increased level of detail in both conceptual site models and numerical flow and transport models. As the complexity of conceptual and structural models increases, innovative approaches and techniques are required to fully exploit the available data, both in the generation of structural models and particularly in the translation of the conceptual and structural models into effective numerical models. Thus a further aim of the modelling study was to develop tools and methods to incorporate and fully utilize the available data in the models.

Central issues for the implementation of MNA at a contaminated site such as Brand are the questions of contaminant plume length and spatial and temporal stationarity. Key to this are the contaminant degradation processes, which need to be understood and quantified as far as possible. The oxidation of organic contaminants in groundwater leads to changes in redox conditions downstream from the source zone as electron acceptors in the aqueous or solid phase are consumed in the parts of the aquifer affected by the contaminant plume (See sections 2.6). The development of redox zones in response to the transformation or degradation of organic contaminants has been recognised for at least 30 years, and has been described for a large number of field sites (e.g. Christensen et al. 2000). Where the availability of organic substrate and nutrients is not a limiting factor for microbial growth, the utilization of electron acceptors appears to occur sequentially, with the thermodynamically most favourable electron acceptors, or Terminal Electron Accepting Processes (TEAPs) becoming depleted before the less favourable; dissolved oxygen is consumed first, after which nitrate, Fe(III) mineral phases and sulfate are consumed prior to

the onset of methanogenesis (Baedecker et al., 1993). In a contaminated aquifer this translates to a distinct spatial zonation of the redox processes downstream from the contaminant source, with oxygen and nitrate as the dominant TEAPs at the fringes of the contaminant plume, giving way to a zone where Fe(III) reduction dominates followed by sulfate reduction and finally methanogenesis occurring closest to the source zone (see Figure 2.4). While this typical sequential picture of TEAP utilization depicts redox zones as being distinct and clearly defined, overlapping of anaerobic redox zones has been reported at a number of sites, with simultaneous consumption of sulfate and Fe(III) (Postma and Jakobsen, 1996; Vencelides et al., 2007), and Fe(III) consumption and methanogenesis (Chapelle et al., 2002; Cozzarelli et al., 2001).

Solid phase electron acceptors, in particular Fe(III) mineral phases, play an important role both in degradation of contaminants and in the temporal and spatial evolution of redox zonation. It has been shown that as Fe(III) minerals become depleted in the aquifer sediments, redox conditions in the plume change, with Fe(III) reduction giving way to methanogenesis as the dominant TEAP (Chapelle et al., 2002; Cozzarelli et al., 2001). Meanwhile, re-oxidation of reduced iron species may significantly influence the spatial availability of electron acceptors for contaminant degradation (Vencelides et al., 2007).

The supply of electron acceptors to the contaminant plume, and hence the redox zonation, is also influenced by local hydrogeological and hydrological conditions; Bjerg et al. (1995) reported differences between the observed redox zonation downstream from a landfill for two parallel transects separated by 30 m, attributed in part to an uneven leaching of electron acceptors from the landfill, while Scholl et al. (2006) showed that the TEAP distribution in a contaminant plume can be influenced by the supply of electron acceptors from vertically infiltrating groundwater recharge.

As organic hydrocarbons degrade at different rates depending on the dominant TEAP (Aronson and Howard, 1997), the spatial and temporal evolution of the redox zonation has significant implications for contaminant transport and should be considered when implementing a long-term remediation strategy such as MNA. For example, increases in plume length have been reported for benzene and ethyl-benzene, which generally degrade more rapidly under Fe reducing than methanogenic conditions, at sites where local depletion of Fe(III) minerals is driving a change in the redox conditions from Fe(III) reducing to methanogenic (Chapelle et al., 2002; Cozzarelli et al., 2001).

In the development of MNA concepts numerical models are frequently used to understand and quantify contaminant emission and degradation processes and to predict the likely future extent of contaminant plumes. It is clearly desirable that the factors discussed above should be included in such models. Various aspects of redox zonation and its role in biodegradation have been considered in numerical modelling studies for different types of contaminated sites, and are widely reported in the literature. Essaid et al. (2003) simulated BTEX degradation with temporally and spatially constant aerobic and anaerobic first-order degradation rates for the oil spill site where Cozzarelli et al. (2001) reported a growth in the benzene and ethyl-benzene plumes as a result of Fe(III) depletion. When they included a finite quantity of Fe(III) as an electron acceptor in the simulations they observed an increase in the benzene plume length as the Fe(III) became depleted. Brun et al. (2002) simulated the development of redox zones downstream from a landfill site for a single contaminant, dissolved organic carbon, with multiple TEAPs, using Monod kinetics with inhibition constants controlling switching between the different TEAPs. They could show that Fe(III) reduction played a major role in the attenuation of DOC at the site, and found that the inhibition constants were very important for matching the observed redox zonation, in particular for the SO_4^{2-} -reduction system. Lønborg et al. (2006) simulated the degradation of six mono-aromatic hydrocarbons downstream from a landfill site using a steady-state redox zone approach in which they applied different degradation rates for compounds in predefined redox zones. They determined first-order degradation rates for the different compounds in the different zones; however their approach relied on the assumption of steady-state redox conditions with limited overlap of the TEAPs.

Schreiber et al. (2004) used a sequential electron acceptor model with first-order kinetics to simulate degradation of BTEX compounds. They observed an increase in methanogenesis as Fe(III) was depleted, but the sequential model was unable to reproduce overlapping TEAPs observed in the field. Prommer et al. (1999) determined the relative importance of iron and sulfate reduction at a BTEX contaminated site by simulating the degradation of toluene in an approach considering multiple electron acceptors and including secondary reactions of reduced iron species. The effect of iron cycling reactions on electron acceptor availability was studied by Vencelides et al.(2007), who simulated the temporal evolution of redox zonation at a BTEX contaminated site and showed that secondary reactions of reduced iron species can be a significant sink for electron acceptors.

The numerical modelling approach for Brand consisted of two stages. In the first stage, the GeoSys/RockFlow finite element model code (Kolditz et al., 2006) was used to develop a

detailed three-dimensional groundwater flow model for the site from a GIS-based geological model in an innovative approach using geometrical entities to map the structural model and boundary conditions and source terms for the conceptual hydrogeological model onto a finite element mesh (Miles et al., 2007). The resulting steady-state flow model was calibrated to the measured hydraulic heads at the site using the automated calibration software PEST (Doherty, 2004), whereby values for groundwater recharge rates and hydraulic conductivity were identified. The calibrated flow model then served as a basis for subsequent two-dimensional reactive transport models.

The reactive transport simulations, developed using the multi-phase, multi-component reactive transport code MIN3P (Mayer et al., 2002), consider Monod and first-order kinetic degradation of multiple contaminants with multiple electron acceptors and secondary reactions of reduced iron species. Inhibition terms are used to control the transitions between the different TEAPs. The transient evolution of redox zones and contaminant plumes is simulated for two separate transects of the site, which have different geology and groundwater recharge distributions and where quite different downstream contaminant and TEAP distributions are observed. A reaction system calibrated to measured concentrations along one transect is used for both cases. In this way the second transect acts as a validation for the reaction parameters calibrated for the first transect. It is then possible to compare and contrast the contributions of the different TEAPs to the overall degradation, the evolution of the TEAP utilisation and the development of the contaminant plumes in the two different hydrological and hydrogeological settings and determine whether this can account for observed differences in TEAP distributions and contaminant plume lengths in different parts of the site.

5.2. Site description

Flughafen Brand is a disused military airfield located approximately 60km south of Berlin, Germany. The airfield was in operation from the late 1950's until the early 1990's, during which time massive contamination of the subsurface beneath the fuel transfer and storage facilities occurred (Figure 5.1). The fuel was stored in above-ground tanks in the south-eastern corner, just below the adjacent railhead used for fuel deliveries, which crosses the site from west to east. In the centre of the site is a large area of open ground covered in parts with construction waste, and to the north-west an unsealed landfill containing construction waste and general detritus. The remainder of the site is covered by mixed forest interspersed with derelict infrastructure. An area of approximately 110 ha is contaminated with an

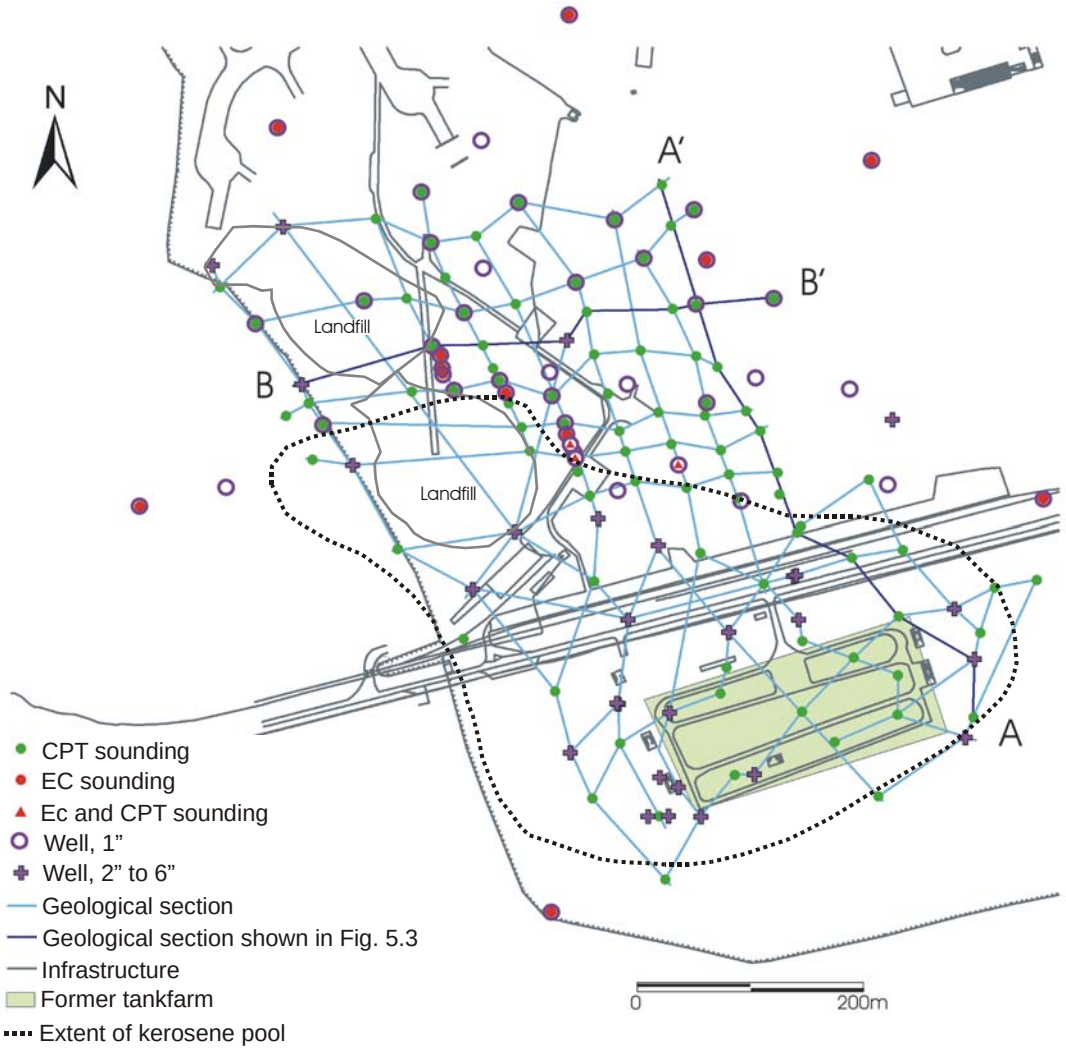

Figure 5.1 Site map of the former tankfarm at Flughafen Brand showing the extent of the kerosene body in the unsaturated zone, locations of monitoring wells, geophysical sounding points and geological profiles used in the development of the structural model.

estimated 500 m³ of kerosene jet fuel, present as mobile and immobile non-aqueous phase in the capillary fringe and unsaturated zone (see Figure 5.1).

The site lies in a topographically flat region of Pleistocene glacial sediments, with a local elevation of around 60 meters above sea level. Hydrologically, the site is located in the Spree river catchment, a small creek approximately 2.5km to the West being the nearest surface water feature. The geology at the site consists of quaternary sediments of up to 100 meters in thickness with principal units of medium, coarse and fine sand. The stratigraphy is complex, forming a hydraulically connected system of aquifers extending to the base of the sediments. Intermediate discontinuous layering of silt and clay is found in the parts of the uppermost aquifer and unsaturated zone. The silt layers are in places glacially deformed with highly variable topography and in parts of the site form the aquitard of a perched

aquifer. The unsaturated zone at the site is approximately 13m in thickness, with the groundwater table typically around 48m above sea level.

A number of investigations have been carried out at the site since the transfer of ownership to the state of Brandenburg in 1992. For the hydrogeological characterisation and groundwater sampling a total of 37 conventionally bored groundwater monitoring wells and 50 1" direct push multi-level monitoring wells are available. The geological survey of the site consists of the drilling records for the conventional wells, as well as 93 cone penetrometer (CPT) soundings and 15 electrical conductivity soundings. The locations of sounding points and monitoring wells are shown in Figure 5.1. Additionally, a total of eleven samples of aquifer material have been taken at ten different locations. These were used both to support the interpretation of data from the direct-push soundings, as well as for the determination of porosity and the estimation of hydraulic conductivities based on particle size distributions. In conjunction with the CPT survey, ROST© (Rapid Optical Sensing Technique) soundings (USEPA, 1997) were carried out at 10 m intervals to accurately delineate the downstream extent of the kerosene phase.

5.3. Model description and governing equations

Two different model codes were used for the three-dimensional hydrogeological model and the two-dimensional reactive transport modeling. For the hydrogeological model the GeoSys/ RockFlow finite element model code (Kolditz et al., 2006) was used, while the reactive transport modelling was carried out using the MIN3P code (Mayer et al., 2002). The following section describes the GeoSys/RockFlow code, while a description of MIN3P is provided in Section 3.3.

The hydrogeological model for Brand considers steady-state groundwater flow in an unconfined aquifer, which is a non-linear problem using hydraulic head *h* as the primary variable. In the unconfined flow approach, a capillary fringe is not considered and the water table defines the boundary between the unsaturated and saturated zones. Unconfined flow is treated as a free surface problem, with the water table defined as a surface where the liquid pressure is assumed to be equal to the atmospheric air pressure. To model unconfined flow a moving mesh technique is used (Beinhorn, 2005). According to Bear (1972) the mass balance equation for a fluid phase (i.e. groundwater) is given by

$$S_0 \frac{\partial h}{\partial t} + \nabla \cdot \mathbf{q} = Q_\rho \qquad (5.1)$$

with the specific storativity of the porous medium S_0, the Darcy flux **q** and a source term for fluid mass Q_ρ. Unconfined flow conditions are mimicked by a kinematic boundary condition at the groundwater table surface;

$$h = z \big| \text{ groundwater table} \tag{5.2}$$

with the elevation of the groundwater table z. Darcy's equation is given by

$$\mathbf{q} = -\mathbf{K}\left(\frac{\nabla h - \rho - \rho_0}{\rho_0} \frac{g}{g} \right) \tag{5.3}$$

with the hydraulic conductivity tensor **K**, the fluid density ρ and a corresponding reference value ρ_0, the gravity vector g and the value of gravity acceleration g = 9.81 ms^{-2}.

The method of weighted residuals is applied to derive the weak formulation of the fluid mass balance equation (1). Assume that $V_n \subset H_1\Gamma(\Omega)_n$ is the test function space. For all $\omega \subset V_1$, we have the weak form of the mass balance equation (1) as

$$\int_\Omega \omega \left(S_0 \frac{\partial \hat{h}}{\partial t} + \nabla \cdot \mathbf{q} - Q_\rho \right) d\Omega = 0 \tag{5.4}$$

with the finite element domain Ω, the test functions ω, the hydraulic head approximation $\hat{h}$. Applying integration by parts, equation (4) can be rewritten as

$$\int_\Omega \omega \left(S_0 \frac{\partial \hat{h}}{\partial t} \right) d\Omega + \int_\Omega \omega (\nabla \omega \cdot \mathbf{q}) d\Omega - \int_\Omega \omega Q_\rho d\Omega = -\int_\Gamma \omega (\mathbf{q} \cdot \mathbf{n}) d\Gamma \tag{5.5}$$

with the domain border for Neumann type boundary conditions Γ. We use the Galerkin finite element method to solve the weak forms of fluid mass balance equation (5), i.e. test functions and element shape functions are set identically. The hydraulic head variable is approximated by admissible finite element functions.

$$\hat{h} = \sum_i^n h_i(t) N_i(\mathbf{x}) \tag{5.6}$$

with element node index i, number of nodes per element n, nodal head values h_i which are time dependent and nodal shape functions N_i which are space dependent. As a result of the finite element procedure an algebraic equation system is derived.

$$\mathbf{A}\mathbf{h}^{n+1} = \mathbf{b} \tag{5.7}$$

with the global system matrix **A**, the nodal hydraulic head vector **h** at new time level *n+1*, and the right-hand-side vector **b**. Local element matrices and vectors are calculated and then assembled from all elements e to the global system matrix,

$$\mathbf{A} = \frac{1}{\Delta t}\sum_e \int_{\Omega^e} N S_0 N^T d\Omega^e + \theta \sum_e \int_{\Omega^e} \nabla N \mathbf{K} \nabla N^T d\Omega^e \tag{5.8}$$

as well as the global right-hand-side vector

$$\mathbf{b} = \frac{1}{\Delta t}\left(\sum_e \int_{\Omega^e} N S_0 N^T d\Omega^e\right)\mathbf{h}^n - (1-\theta)\left(\sum_e \int_{\Omega^e} \nabla N \mathbf{K} \nabla N^T d\Omega^e\right)\mathbf{h}^n + \sum_e \int_{\Omega^e} N Q_\rho d\Omega^e - \sum_e \int_{\Gamma} N(\mathbf{q}\cdot\mathbf{n}) d\Gamma \tag{5.9}$$

with the time step increment ∆t, old time level *n*, and collocation factor θ.

In the framework of the object-oriented FEM, instances of a general finite element class CFiniteElement for parabolic PDE types deal with all related FE operations such as element matrix calculations and global assembly for arbitrary geometric element types (Wang and Kolditz 2006).

5.4. Geological model

The following section describes the development of the geological model for the saturated zone at the site. The interpretation of the geological data and creation of GIS-based two-dimensional geological profiles is described in Section 5.4.1 and the three-dimensional model is presented in Section 5.4.2.

5.4.1. Interpretation of geological data

Geological data for the site were available in a number of forms, both from samples of aquifer material and drilling logs from the installation of conventional monitoring wells, as well as from direct push cone penetrometer (CPT) and electrical conductivity (EC) soundings.

The following section will briefly summarise the information available from the various methods, and describe the combination of the various data in the structural model for the site. Soil cores and drilling logs provide direct geological information, however – unless a continuous core sample is taken, which is generally an expensive exercise – with poor vertical resolution. Smaller scale hydrostratigraphic features, which can be of particular

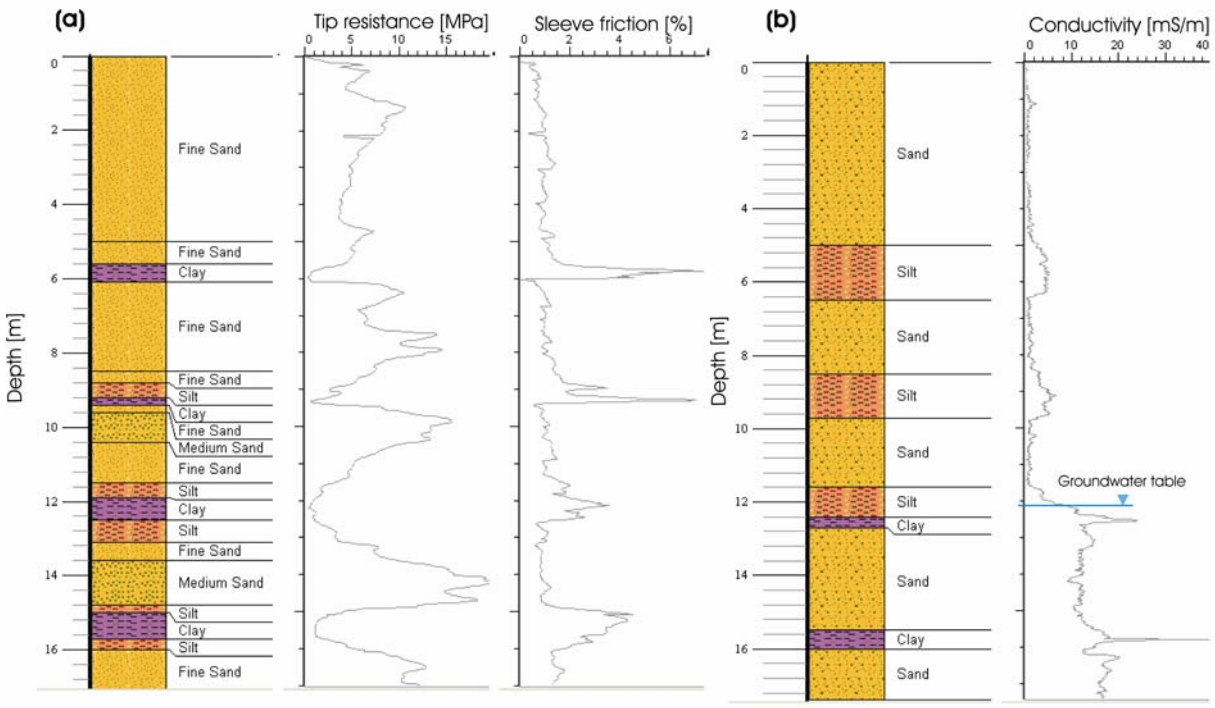

Figure 5.2 Geological profiles (a) from interpretation of CPT data (b) from interpretation of EC data at the same location. Adapted from Miles et al. (2007)

interest and importance with relation to contaminant transport, generally cannot be delineated. Direct push methods, whereby a probe is driven or hammered into the subsurface, generally deliver data at a higher vertical resolution. Additionally they are typically faster, and hence cheaper, than conventional drilling methods, thus a higher density of sampling locations is possible in a site investigation.

The cone penetrometer test is probably the most well established of all direct-push sounding methods, and dates back to the 1920's. The penetrometer itself essentially consists of a cone shaped probe at the end of a steel shaft. Sensors in the probe measure the mechanical resistance at the tip and sleeve friction along the shaft as the probe is driven into the subsurface at a constant rate. From the tip resistance and sleeve friction the sediment type can be inferred (Robertson, 1990). Sand, for example, typically has a high tip resistance and low sleeve friction, while a till has a low tip resistance and high sleeve friction (Robertson and Campanella, 1983a; 1983b). The data from a CPT sounding can thus be interpreted to provide a profile of the sediment progression with a vertical resolution in the order of 0.02m. Such an interpretation is shown in Figure 5.2(a), whereby the relationship between tip resistance, sleeve friction and the inferred material type can be clearly seen. At locations where 1.2m length soil cores corresponding with the CPT soundings were available, a good agreement was found between the CPT interpretation and the material in the core.

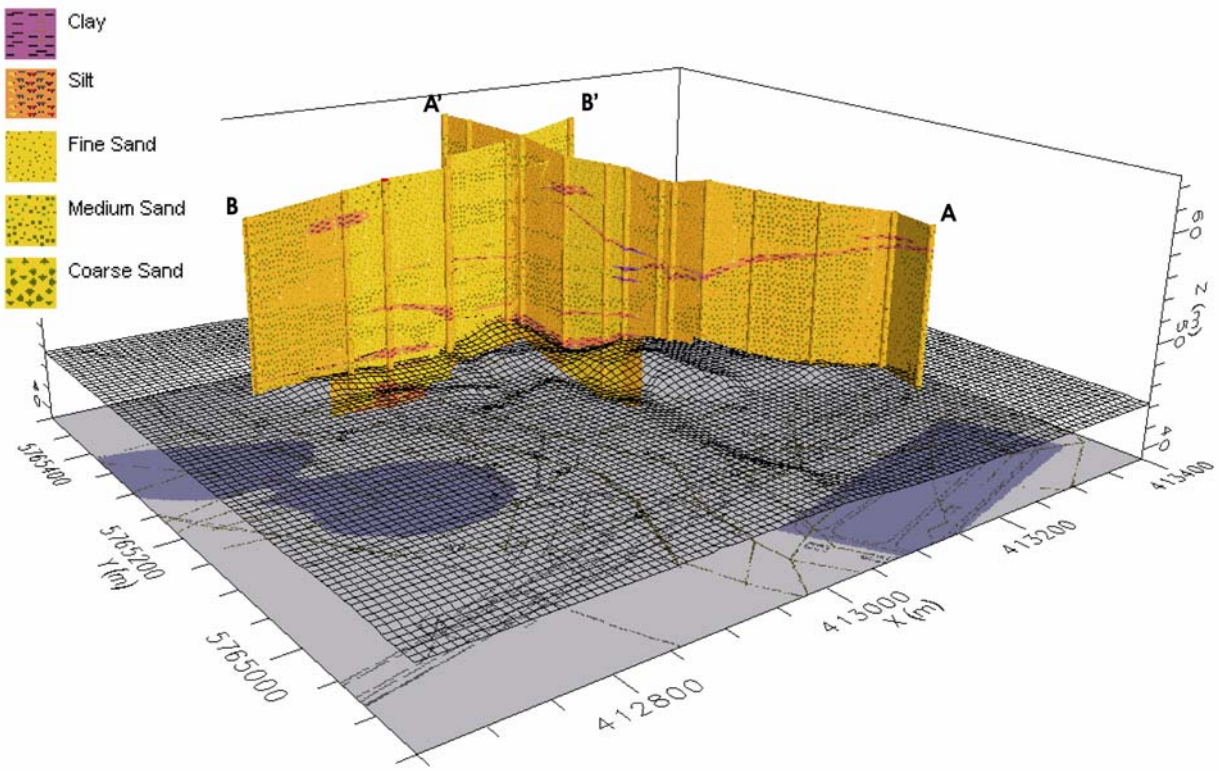

Figure 5.3 Intersecting two-dimensional geological profiles (see Figure 5.1 for the profile locations). The wire mesh surface shows a laterally interpolated layer. Adapted from Miles et al. (2007).

In a direct push EC sounding a conductivity probe is driven into the subsurface, while the apparent electrical conductivity of the sediments is calculated from an imposed electrical current (Dietrich and Leven 2005). The probe itself typically has four electrodes in a Wenner array, whereby the electrodes are arranged in a line; a current is driven through the soil between the two outer electrodes and a voltage measured across the inner electrode. The electrical conductivity of sediments in the saturated zone of an aquifer where variations in groundwater chemistry are small is principally controlled by particle size and mineral type, with clay minerals having a higher conductivity than sands. Thus zones of low hydraulic permeability can be identified in the vertical profile (Schulmeister et al., 2003). For sediments with a low electrical conductivity, such as sands, an increase in conductivity is generally observed at the groundwater table, the magnitude of the increase being a site-specific parameter dependent on groundwater chemistry. The vertical resolution of the data collection depends on the spacing of the electrodes in the probe; using a Geoprobe® direct push unit and conductivity probe, data were recorded with a vertical resolution in the order of 0.02m. A typical profile obtained for the site is shown in Figure 5.2(b).Comparing the geological interpretations for the CPT and EC soundings in Figure 5.2 it can be seen that there is a good agreement between the two methods in terms of defining the positions of the low permeability units. There are, however some discrepancies in the interpretation of the

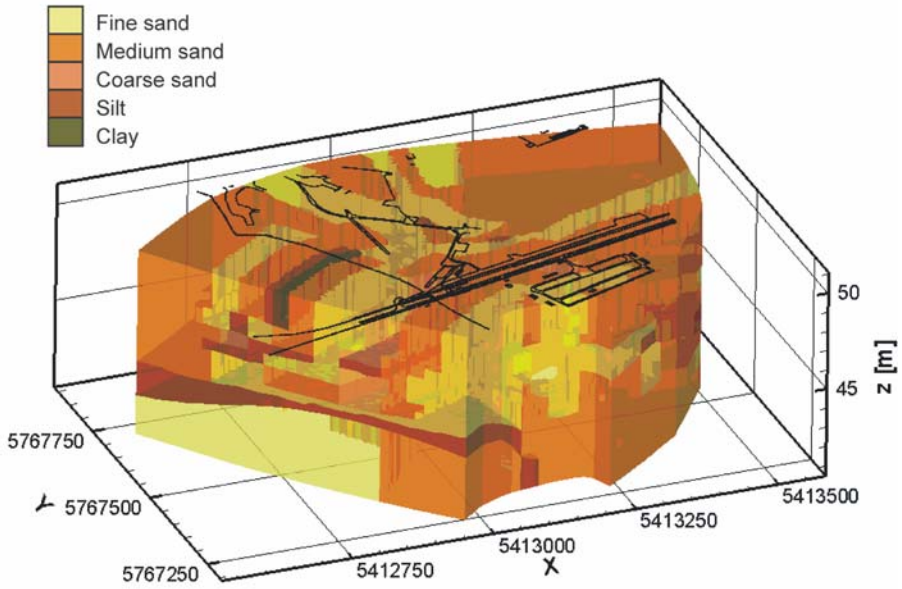

Figure 5.4 Three-dimensional geological model for the saturated zone

material type of these units; where the CPT interpretation indicates clay, the EC interpretation is silt and vice-versa. This is because the interpretations for both methods are based principally on empirical relationships, and are to some extent subject to the influence of site-specific factors. The overall increase in conductivity at the groundwater table can clearly be seen in the EC profile between 11.5 and 12m below the surface.

The combined data from the drilling logs, CPT and EC soundings, which were also compared with undisturbed soil samples where available, were used to prepare 24 intersecting two-dimensional geological profiles for the site in a GIS-based environment. Five material classes were used in the geological interpretation; fine, medium and coarse sand, silt and clay, to which hydrogeological parameters were also assigned. The locations of the profiles can be seen in Figure 5.1, and an example of two intersecting profiles is shown in Figure 5.3.

5.4.2. Development of the 3D geological model for the saturated zone

The 2D geological profiles were divided into layers, with top of the uppermost layer at approximately 50m above sea level, slightly above the average groundwater level for the site. Where possible, the layers were arranged such that the typically discontinuous patches of different sand types and discrete units such as silt lenses were defined within a single layer. This resulted in nine layers of varying thickness over a total depth of approximately eleven meters. Three dimensional surfaces were then created by interpolating the layer elevations between the two dimensional profiles (see Figure 5.3). The geological

information at each layer interface in the 2D profiles was then interpolated laterally between the profiles, creating maps of the distribution of different material types within each of the layers. These material distribution maps were then imposed on the layer elevation surfaces to create three dimensional volumes delineating the material types using methods described by Miles et al. (2007). The resulting three-dimensional model of the saturated zone is shown in Figure 5.4

5.5.Hydrogeological model

The following section describes the development and calibration of the three-dimensional hydrogeological model for Brand. Section 5.5.1 describes the development of the conceptual model from the geological model, while the calibration of the model is described in Section 5.5.2.

5.5.1. Conceptual hydrogeological model

Hydraulic head data recorded at monthly intervals at the site shows only minor fluctuations in the local flow field in the short to medium term. On this basis, a steady-state flow model for the site was developed. For the development and calibration of the model the most recent, and in terms observation density most comprehensive, set of measurements, namely from December 2005 were used. Figure 5.5(a) shows the hydraulic situation and the model domain. The groundwater flow at the site is from South to North, and generally divergent. As the divergent flow pattern in the area cannot be directly attributed to local topographical or hydrological features, it is thought that it may be due to secondary perched aquifer systems collecting infiltrating water and focussing it in small areas where there is communication with the main aquifer, causing localised changes in the hydraulic gradient. This explanation was subsequently supported by the hydrogeological model. The domain covers an area significantly larger than that of interest for later reactive transport modelling in order to minimise boundary effects. As the area lacks geological, hydrogeological and hydrological features that might lend themselves to the definition of model boundaries, these were based on interpolated hydraulic head isolines. At the upstream and downstream boundaries (here corresponding to South and North, respectively) a fixed head condition is applied. The upstream boundary was assigned a value of 50.38m along its entire length. For the downstream boundary, which spans a much greater length, the fixed head value was varied between 49.65m and 49.75m along the boundary, following the trend of the

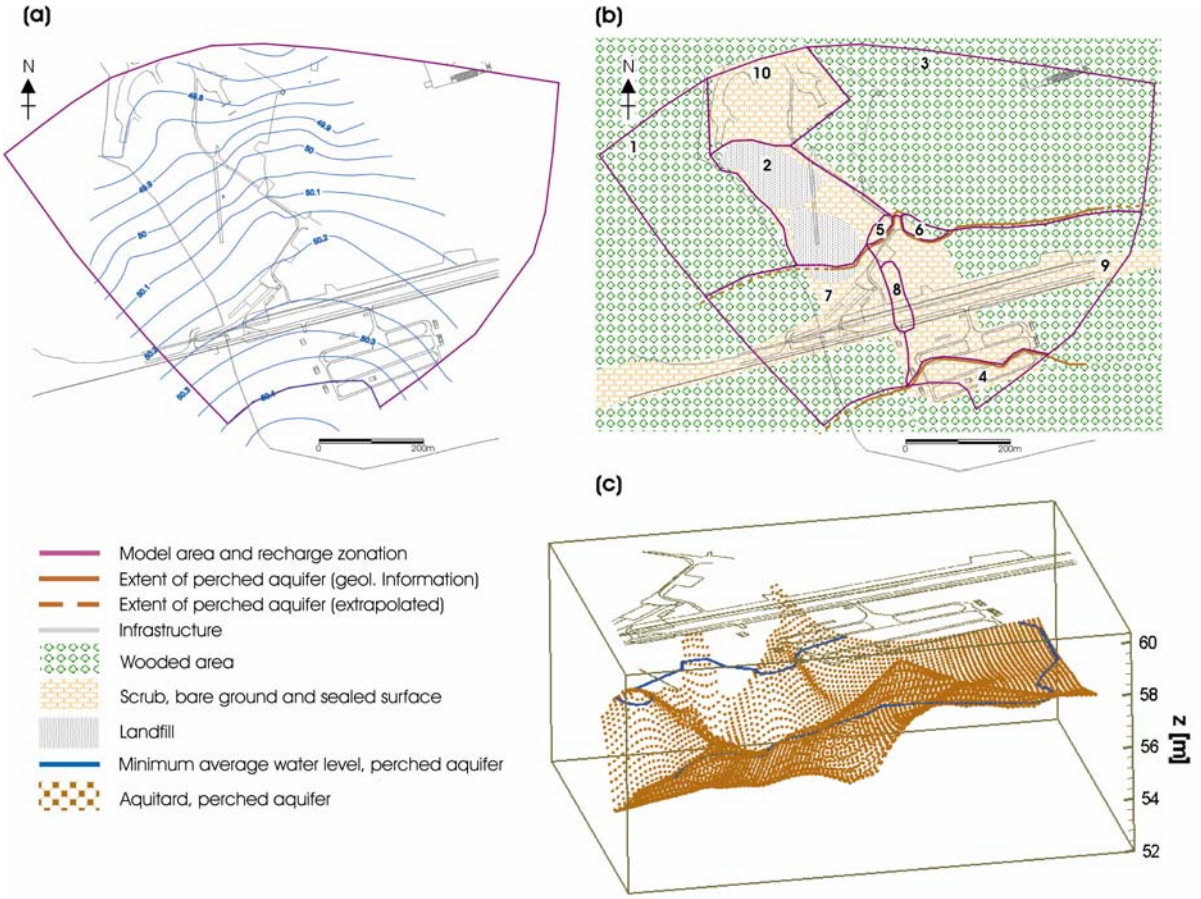

Figure 5.5 (a) Model area based on measured head values, (b) Numbered recharge zones with approximate ground cover distribution and the extent of the perched aquifer in the southern half of the site, (c) Three-dimensional visualisation of the perched aquifer, showing the basin form of the aquitard and the minimum water level. Adapted from Miles et al. (2007).

northernmost isolines. The no-flow boundaries to the East and West are normal to the head isolines at the points where they intersect.

The zonation of groundwater recharge in the model domain into ten zones, shown in Figure 5.5b, was based on a combination of the geological situation and the surface ground cover. The ground cover at the site, which directly affects local groundwater recharge through its influence on infiltration and evaporation, can be seen in Figure 5.5b. The cover can be classified as areas of mixed forest, sealed surfaces related to the former military infrastructure, bare ground, sparse scrub and brush. Additionally there is a large unsealed landfill, about which little is known. In the southern half of the site a basin shaped silt structure in the unsaturated zone forms the aquitard of a perched aquifer. The extent of this feature, delineated from the available geological information, can be seen in Figure 5.5b, while a three-dimensional visualisation of the structure is shown in Figure 5.5(c). The assumed flow direction for water in this structure is from East to West. At two points along

the northern boundary of the perched aquifer, the edge of the silt aquitard is at a lower elevation than the minimum measured groundwater level in the upper aquifer, and it is thought that at these points there may be an overflow to the lower aquifer. In the central region of the basin structure, discontinuities in the silt layers are thought to act as windows, communicating to some extent with the lower aquifer. The perched aquifer is thought to significantly influence the distribution of groundwater recharge at the site by intercepting and gathering recharge across a large area in the southern part of the site and focussing it to some extent at these points. The selection of parameter values for the hydrogeological conceptual model is discussed in Section 5.5.2.2.

The conceptual model was applied to a finite element mesh created for the model area shown in Figure 5.5(a). An unstructured two-dimensional triangular mesh was first generated for the model area using a mesh generator based on an unstructured 2D Delauney algorithm (Shewchuk, 1996) implemented in the GMSH code (http://www.geuz.org/gmsh). A mesh density distribution size of 10 m was used in the central region of the model domain, and a size of 15 m in the outer regions. The resulting smaller element size in the centre of the domain was intended to take into account the higher density of geological data available, and hence greater level of detail in the geological model in this region. The two-dimensional mesh was then used as a basis to generate a three-dimensional prismatic mesh, whereby the two-dimensional mesh was duplicated at multiple elevations to create prismatic layers. The resulting mesh for the numerical model consisted of 52,330 nodes connected by 92,727 elements. Using an innovative mapping procedure the prismatic mesh layers were mapped to the interpolated layer elevations generated for the geological model, while material type attributes were mapped to the mesh elements from the three-dimensional volumes of the geological model. Thus the complex three-dimensional structure of the geological model was preserved and resulting numerical model domain was an exact analogue of the geological model. The same procedure was used to assign boundary conditions and source terms to the appropriate mesh nodes. A comprehensive description of the mapping procedure and assignment of node and element properties can be found in Miles et al. (2007).

5.5.2. Inverse modelling approach and parameter identification

The application of automated model calibration tools for parameter estimation in inverse models and the advantages of such an approach have been described in numerous publications (Carrera and Neuman, 1986; Hill, 1992; Hill, 1998; Poeter and Hill, 1997).

Briefly, the main benefit of such an approach is its ability to optimise the base model, determining parameter values that provide a quantified best fit between simulated model output and measured data. The parameters optimised were hydraulic conductivities and recharge rates, using measured head values from December 2005 as the calibration target.

5.5.2.1. Implementation of the PEST parameter estimation tool

The parameter estimation software, PEST (Doherty, 2004) was chosen for the model calibration and parameter identification. The latest version of the software, v10.0.2, October 2005, was used. The estimation technique adopted by PEST has been tested on a wide range of problems and is considered to be quite robust (Doherty, 2004). The software could be directly applied to the GeoSys/RockFlow model code by preparing template files corresponding to the model's text format input and output files, using the methods described in the PEST software documentation (Doherty, 2004).

The goal of any model calibration is to minimise the difference between a set of observed values and values generated by a model. The PEST code computes values for a set of parameters that minimise the objective function, Φ, which is essentially the sum of the squared differences between modelled and observed values. The software iteratively analyses the influence on the objective function for changes in each of the parameters to be optimised and then adjusts the parameters to achieve a maximum reduction in Φ. The mathematics of the PEST algorithm are comprehensively described in the software documentation (Doherty, 2004). Briefly, the basis for the non-linear parameter estimation is the assumption that the modelled system can be represented by a continuously differentiable function, M, which maps n-dimensional parameter space into m-dimensional observation space, described by:

$$h_o = M(\boldsymbol{p_o}) \tag{5.10}$$

where $\boldsymbol{p_o}$ is the vector representing the set of parameters and h_o the set of model calculated observations. A further set of model calculated observations can be calculated using a set of parameters, $\boldsymbol{p}$ that are close to, but not identical to $\boldsymbol{p_o}$:

$$h = h_o + \boldsymbol{J}(\boldsymbol{p} - \boldsymbol{p_o}) \tag{5.11}$$

where $\boldsymbol{J}$ is a jacobian matrix of m rows of observations and n columns of derivatives of each observation with respect to each of the parameters, with the derivatives calculated using the finite difference method. The objective function, Φ, is then defined by:

$$\phi = (h - h_o - \boldsymbol{J}(\boldsymbol{p} - \boldsymbol{p_o}))^T (h - h_o - \boldsymbol{J}(\boldsymbol{p} - \boldsymbol{p_o})) \quad (5.12)$$

where T represents matrix transposition.

The model was calibrated using 47 hydraulic head measurements for the objective function, the positions of which can be seen in Figure 5.6(a). Corresponding calculated head values were obtained from the model nodes located closest to the position of the centre of the well screen in the model domain. The calibration was considered complete when the reduction in Φ was less than 0.005 over four consecutive calibration iterations.

5.5.2.2. Calibration parameter ranges

The various parameter ranges used for the calibration, shown in Table 5.1, were determined as follows. Hydraulic conductivity values for the five material types were estimated from particle size distribution curves for samples of aquifer material from the site using the Hazen method (Hazen, 1911). For all material types a range of +/- 50% of the estimated value was used in the calibration.

To estimate groundwater recharge rates for the site, it was assumed that for the sandy topsoil and flat topography found at Brand, the surface runoff of precipitation could be considered to be negligible, and infiltration at the site could be assumed to be equal to the difference between the precipitation and the actual evapotranspiration. The actual evapotranspiration was calculated using the method described by Bagrov (Bagrov, 1953), which has been shown to be applicable to Germany (Glugla and Müller, 1997). The Bagrov relationship combines mean annual values for corrected precipitation P_{corr}, maximum evapotranspiration based on land use ET_{max} and actual evapotranspiration ET_a, where

$$\frac{dET_a}{dP_{corr}} = 1 - \left(\frac{ET_a}{ET_{max}} \right)^n \quad (5.13)$$

The Bagrov parameter, n, which was determined from extensive lysimeter evaluations, describes the water storage characteristics of a soil as a function of the ground cover; for example, coniferous forest, for which evapotranspiration is relatively high, has values of n between around 2.0 and 4.0, while for sandy bare ground, where little evapotranspiration occurs, n has a value of 0.53. Data for precipitation and maximum evapotranspiration from a nearby weather station and the appropriate n values for the ground cover types were used to calculate the potential range of groundwater recharge rates for each of the recharge zones. For zones 7 and 9, where it is thought that the presence of the hanging aquifer significantly

reduces recharge to the main aquifer, as discussed in Section 5.5.1, a very low maximum recharge was assumed. As zero values are best avoided in the PEST calibration process (Doherty, 2004), for zones where the lower limit of the potential recharge range was zero a minimal value of 10mm/a was used. For zones 5, 6 and 8, where it is thought that recharge from a large area may be focussed by discontinuities in the aquitard of the hanging aquifer (see 5.5.1), a high maximum recharge was assumed. The upper limit for this was calculated from the volume of recharge intercepted by the hanging aquifer in zone 9 and the ratio of the area of zone 9 to that of zones 5, 6 and 8.

5.5.3. Results and discussion (hydrogeological model)

The optimised parameter set resulting from the calibration process is shown in Table 1. For the hydraulic conductivities, the optimised parameter values for medium sand, coarse sand and clay lie around the middle of the range used for the calibration, while those for fine sand and silt are at the maximum of their allowed ranges. The values for fine and medium sand, which constitute the bulk of the aquifer sediments, compare well with hydraulic conductivities determined from slug tests carried out subsequent to the modelling at various locations where corresponding geological data were available. For fine sand an average value of 1.1×10^{-4} +/- 1.4×10^{-4} m/s was determined from slug tests, while the model calibrated value was 1.2×10^{-4} m/s. The slug test determined value for medium sand was 3.0×10^{-4} +/- 1.0×10^{-4} m/s, which was the lower limit of the range used for the model calibration. The hydraulic conductivity for medium sand determined in the model calibration was 7×10^{-4} m/s.

For recharge the values for four of the 10 zones, namely zones 1, 3, 5 and 9, are well within the parameter ranges, while the remainder tend to the maximum or minimum of their respective allowed ranges. The groundwater recharge rates for the wooded areas are lower than those for bare ground, although the allowed ranges overlap, which is consistent with the assumptions regarding the influence of ground cover. The high values for zones 5 and 6 would appear consistent with the idea of an overflow from the hanging aquifer to the main aquifer discussed in Section 5.5.1.

When optimising conductivity and recharge simultaneously, it is necessary to consider the problem of parameter correlation, i.e. that a change in hydraulic conductivity may have an the same effect on modelled head values as a change in recharge, which has obvious implications in terms of the uniqueness of the optimised parameter set (Poeter and Hill, 1997). While it was seen to be the case during the calibration process that some parameters

Table 5.1. Model parameters included in optimization procedure: calibration parameter ranges and optimized parameter values.

Parameter	Category / Zone	Initial range of parameter values: Minimum - Maximum	Optimised parameter value
Hydraulic conductivity [m s^{-1}]	Fine sand	$4.0 \cdot 10^{-5}$ - $1.2 \cdot 10^{-4}$	$1.2 \cdot 10^{-4}$
	Medium sand	$3.0 \cdot 10^{-4}$ - $9.0 \cdot 10^{-4}$	$7.0 \cdot 10^{-4}$
	Coarse sand	$5.0 \cdot 10^{-4}$ - $5.0 \cdot 10^{-3}$	$1.8 \cdot 10^{-3}$
	Silt	$1.0 \cdot 10^{-5}$ - $4.0 \cdot 10^{-5}$	$4 \cdot 10^{-5}$
	Clay	$1.0 \cdot 10^{-6}$ - $4.0 \cdot 10^{-6}$	$3 \cdot 10^{-6}$
Recharge [mm/a]	Zone1 (Mixed woodland)	100 - 250	160
	Zone2 (Landfill)	200 - 365	200
	Zone3 (Mixed woodland)	100 - 250	160
	Zone4 (Mixed woodland)	115 - 300	115
	Zone5 (Low point at edge of perched aquifer)	10 - 6000	2370
	Zone6 (Low point at edge of perched aquifer)	10 - 6000	6000
	Zone7 (Aquitard in unsaturated zone)	10 - 50	10
	Zone8 (Window in aquitard in the unsaturated zone)	10 - 6000	10
	Zone9 (Aquitard in unsaturated zone)	10 - 50	38
	Zone10 (Scrub/bare ground)	230 - 360	230

were strongly correlated, repeating the calibration using different starting values for the parameters yielded the same result for the optimised parameter values, indicating that the calibration process was reaching a global rather than a local minimum for Φ.

The results of the model run with the optimised parameters are shown in Figure 5.6. Overall a good agreement between modelled and measured heads was achieved using the optimised parameters, with the objective function Φ = 0.024m at the end of the calibration process. The maximum absolute error (modelled – measured head) for the 47 observations was 0.06m. Figure 5.6(a) shows a comparison of the modelled and measured head isolines, while in Figure 8b the modelled heads are shown plotted against the measured, whereby the deviation of the points from the line *modelled/measured = 1.0* offers a visual measure of the agreement across the site. It can be seen from Figure 5.6(b) that the errors appear to be randomly distributed as opposed to systematic. The modelled head isolines shown in Figure 5.6(a) are generated from the modelled data at a single elevation, $Z = 48m$, using all nodes in this plane for the interpolation. As there is a high degree of hydraulic connectivity in the system, the hydraulic heads do not vary with depth within the model domain, and hence the interpolated heads at this arbitrary elevation are considered here as being representative for the whole domain. It should be noted that while the interpolation of measured hydraulic heads is based on 47 values, the interpolation of modelled heads is based on a far larger data

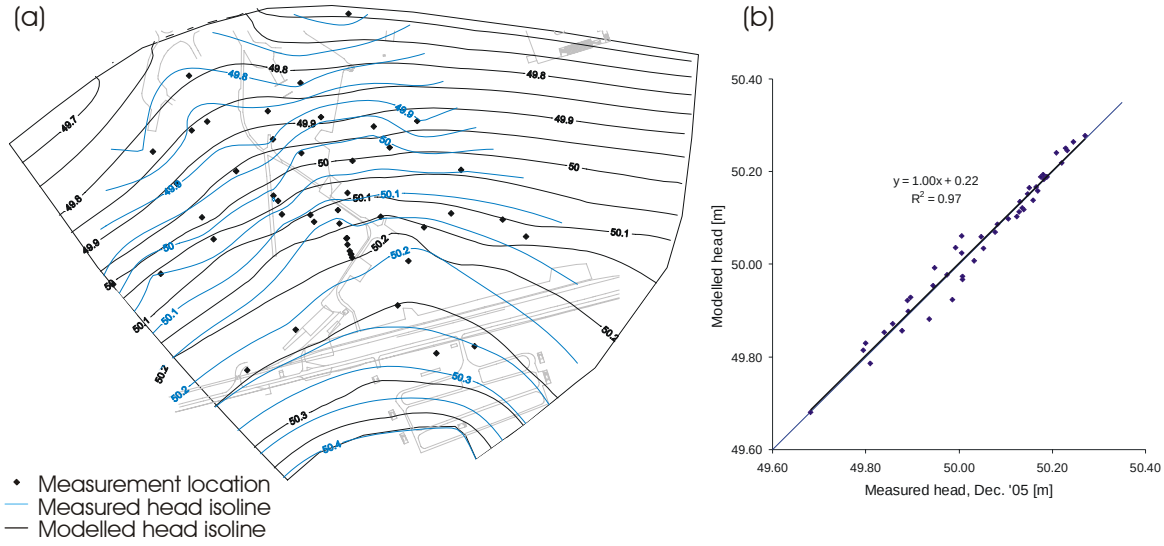

Figure 5.6 Optimised model results. (a) comparison of modelled (black) and measured (blue) heads showing recharge zonation and monitoring wells used for the calibration. (b) Modelled vs. measured head values with linear regression coefficient and *y/x = 1.0* line. Adapted from Miles et al. (2007).

set, i.e. head values at all of the model nodes in the lateral plane, which gives rise to some differences between the two sets of isolines.

The optimised parameters support the assumptions made in the development of the conceptual site model about the way in which the hydrogeological situation at the site is influenced by the hanging aquifer structure. The isolines of the measured head data for the site show an area of divergent flow in the central region of the site where the 50.15m and 50.2m isolines are strongly curved. As there was no obvious geological feature in the structural model of the saturated zone to account for this behaviour, it was thought that the cause might be the influence of the hanging aquifer in the unsaturated zone, as discussed in Section 5.5.1. In the model simulations it was not possible to reproduce this behaviour without considering high values for groundwater recharge, and the results of the model calibration would seem to support the theory. The levels of recharge for zones 5 and 6, intended to represent the overflow points at the edge of the aquitard in the unsaturated zone, are very high, 2370 and 6000mm/yr respectively, while the values for zones 7 and 9, representing the aquitard are very low at 10 and 50mm/yr respectively. For the area in the centre of the hanging aquifer, zone 8, where it was thought that windows in the aquitard allowed communication with the lower aquifer, the calibrated recharge value of 10mm/yr was comparable to the values for the aquitard areas, suggesting that the communication is less significant than thought.

5.6. Reactive transport model

The reactive transport modelling concept for the site was developed based on the observed distributions of contaminants and electron acceptors (or reduced species, respectively) in conjunction with geological and hydrogeological factors. Figure 5.7 shows the site area with the extents of the hanging aquifer and kerosene LNAPL contamination.

The aqueous phase contamination at the site consists mainly of mono-aromatic hydrocarbons (MAH), i.e. benzene, ethylbenzene, xylenes, trimethyl- and propylbenzenes; significant concentrations of toluene are not found at the site. Two isolines for the total MAH concentration are included in Figure 5.7. Concentrations of above 1 mg/l are observed consistently beneath the source zone. Downstream, the concentrations fall to below 0.1 mg/l within a few meters in the western part of the site, while in the east the MAH plume extends much further, with measured concentrations remaining above 0.1 mg/l for about 100 m downstream from the source zone.

The distributions of the four most important electron acceptors and reduced redox species at the site, oxygen, Fe(II), sulfate and methane, are shown in Figure 5.8. Nitrate is not present at significant concentrations and so is not included. Anoxic conditions with dissolved oxygen concentrations of below 1 mg/l exist beneath the source zone and extend downstream for 2-300 meters, beyond which low concentrations of 3-4 mg/l are found. Low concentrations of oxygen are also found in the centre of the site, where there is communication between the perched and main aquifers. Fe(II) is found at high concentrations (> 30 mg/l) beneath the entire source zone, with concentrations falling to below 10 mg/l within 1-200 m downstream. The Fe(II) concentrations downstream from the source zone follow a similar pattern to that of the MAH concentrations, extending further in the east of the site than in the west. In the centre of the site where conditions are slightly oxic, Fe(II) is not detected beyond the source area. The Fe(II) distributions indicate that Fe(III) reduction is occurring as a significant biodegradation process in the source zone and contaminant plume, with re-mineralisation or ion exchange processes limiting the transport of Fe(II) away from the areas where it is being produced. Sulfate is significantly depleted in the eastern part of the site, with concentrations below 10 mg/l compared to the background concentrations of 60 – 70 mg/l found outside the contaminated area. To the west the concentrations are also depleted, though to a lesser extent.

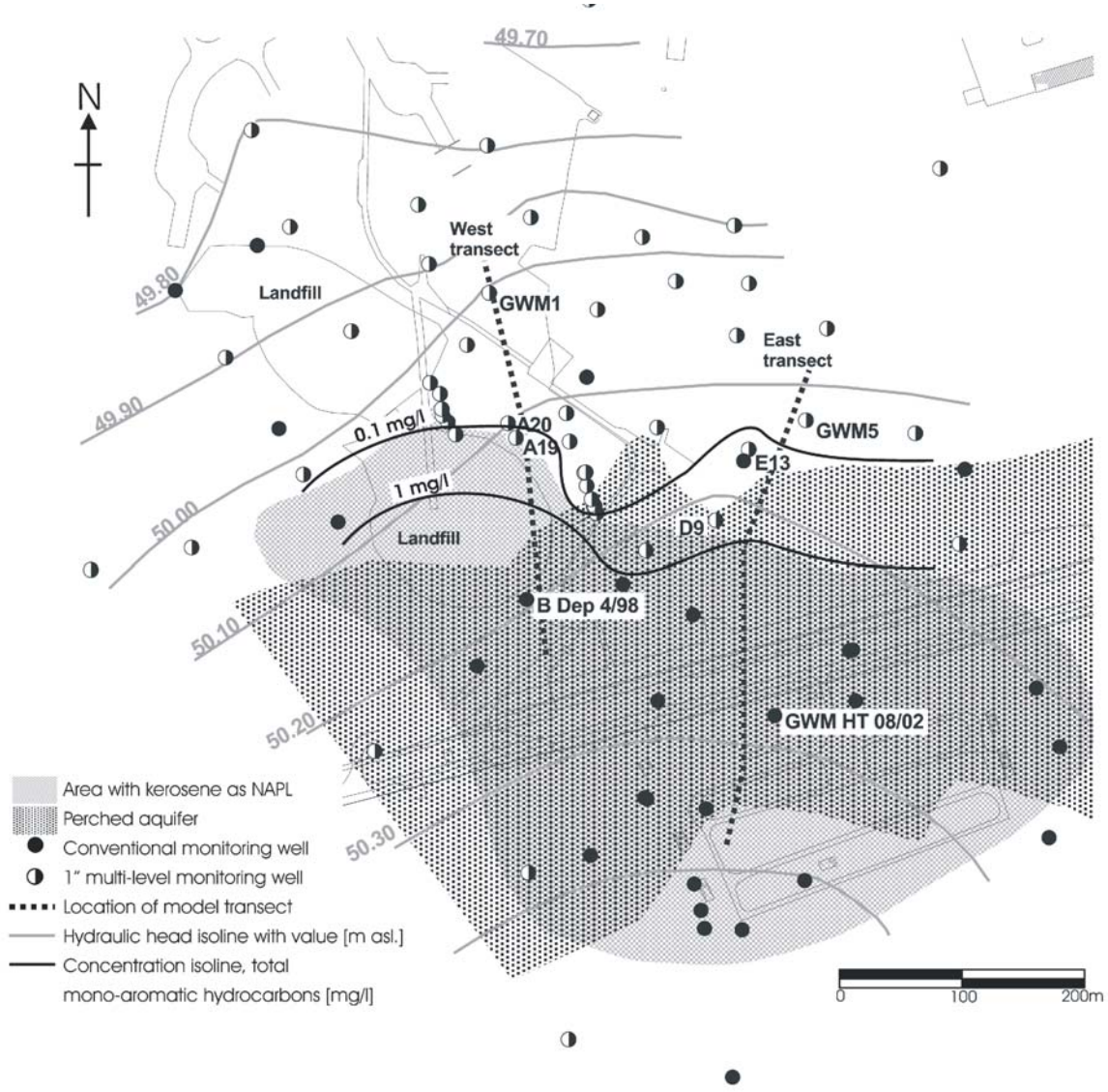

Figure 5.7 Sitemap showing the tankfarm area with the extent of the kerosene spill. The perched aquifer system and the landfill area overlie parts of the kerosene spill. Locations are shown for conventional and 1" multi-level monitoring wells, with well names shown for those providing the measured concentrations for the modelled transects. Hydraulic head isolines show the local groundwater flow situation. Concentration isolines for the total mono-aromatic hydrocarbon concentration are also shown.

In the centre of the site, similarly to oxygen, an area of higher concentration is seen. For methane, the highest concentrations (18 mg/l) occur beneath the source zone in the south-east of the site, with elevated concentrations extending downstream, while to the west much lower methane concentrations, mostly below 1 mg/l, are observed.The observed concentrations of the anaerobic redox species indicate overlapping of anaerobic redox processes at the site. Elevated Fe(II) concentrations are found together with both low

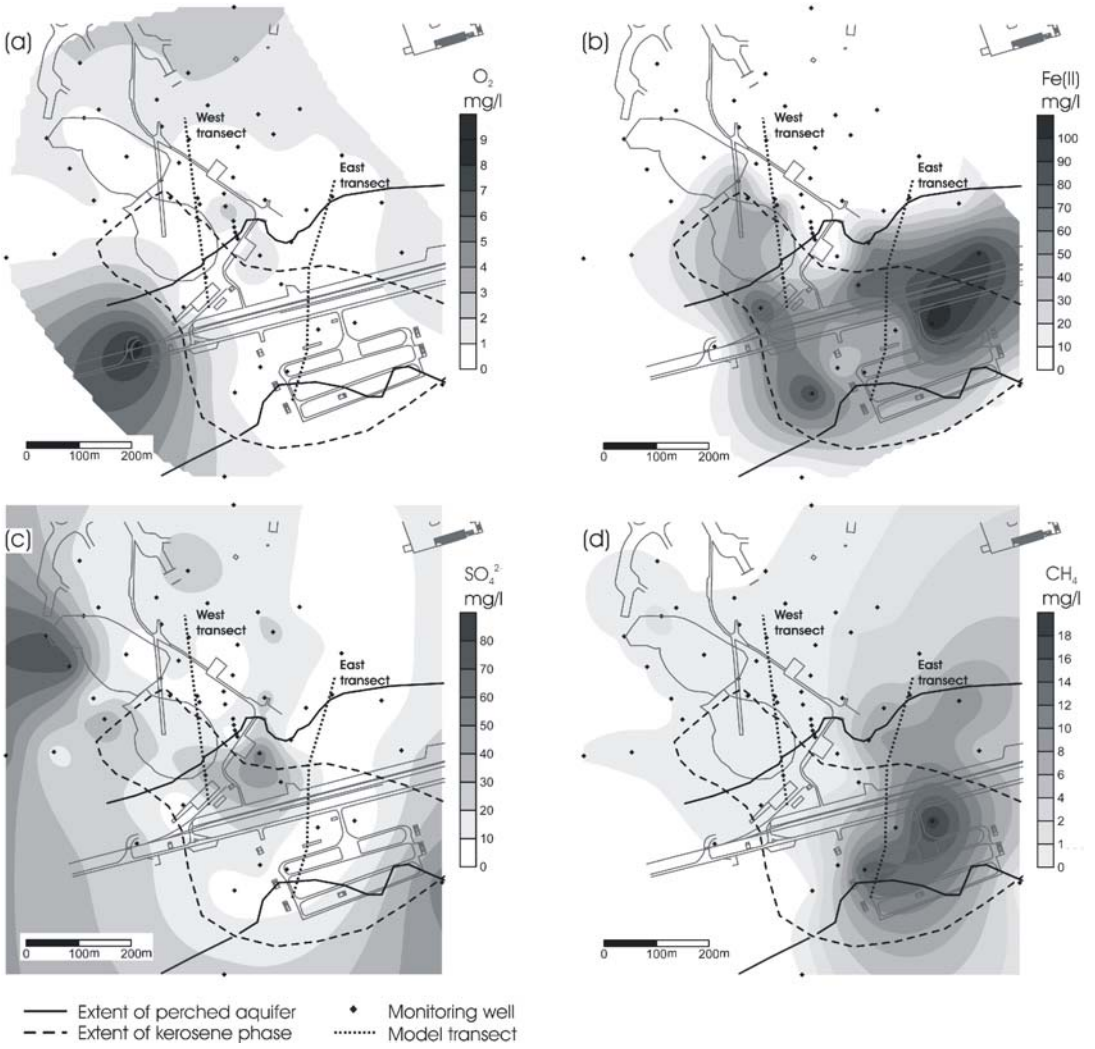

Figure 5.8 Distribution of aqueous phase electron acceptors and reduced products (a) Oxygen (b) Fe(II) (c) Sulfate (d) Methane. For multi-level monitoring wells the minimum (oxygen, sulfate) or maximum (Fe(II), methane) concentrations for the sampled intervals were used in the interpolation. The extent of the kerosene spill and perched aquifer and the positions of the model transects are also shown.

sulfate concentrations and high methane concentrations, which may indicate that Fe(III) reduction is occurring concomitantly with both sulfate reduction and methanogenesis. Sulfate reduction and methanogenesis appear to be more separated, with the highest methane concentrations only found where sulfate concentrations are very low.

Overall, in terms of contaminant plume lengths and distributions of redox species, the site can be broadly divided into two different areas. The eastern part of the site, where the source zone is completely covered by the perched aquifer, i.e. with reduced groundwater recharge, is characterized by high methane and low sulfate concentrations, with elevated Fe(II) concentrations extending downstream from the source zone and long MAH plumes.

In the western part of the site, where the downstream are of the source zone is not covered by the perched aquifer, sulfate concentrations are higher, methane concentrations are lower, elevated Fe(II) concentrations do not extend as far downstream and MAH plumes are short .

5.6.1. Conceptual model

On the basis of the observed differences in the TEAP distributions, two-dimensional flow and reactive transport models were created for two transects of the site approximately parallel to the groundwater flow direction, one in the east, the other in the west of the site (see Figure 5.7 and Figure 5.8

5.6.1.1. Model domain and boundary conditions

The first step in the modelling approach was the creation of flow models for the two transects, with steady-state conditions assumed for the site based on the relatively stable hydraulic conditions observed over the last decade. The reaction system was then developed and calibrated to observed concentrations in the east transect. The calibrated reaction system was then implemented in the west transect without further adjustment of the reaction parameters. The model domains for the 365m × 11.3m east transect and the 270m × 11.3m west transect are depicted in Figure 5.9, with general information and parameter values summarised in Table 5.2. Each transect includes four monitoring wells positioned either directly in, or projected onto the transect (Figure 5.7). The wells within the source zone are conventional 4” monitoring wells, screened over a 2 m interval, while the downstream wells are 1” diameter installed by direct-push, where multilevel groundwater samples were taken using a mobile inflatable packer system with a 90 cm sampling screen. A pre-processing software tool was developed to generate the geological parameter distributions for the transects directly from the GIS-based geological model, allowing the fairly complex stratigraphy of the five material types from the geological model (fine, medium and coarse sand, silt and clay) to be accurately reproduced in the finite volume grid (Figure 5.9(a) and (b)). The finite volume grids for the domains consisted of 26,000 and 30,000 cells for the east and west transects respectively. The grid spacing was 0.75 m horizontally, with local refinement in the central part of the west transect, where difficulties with the flow model were encountered due to the geological parameter distribution, while vertically a variable spacing was used, with a minimum cell size of 0.1 m in the upper portion of the domains to account for steep geochemical gradients.

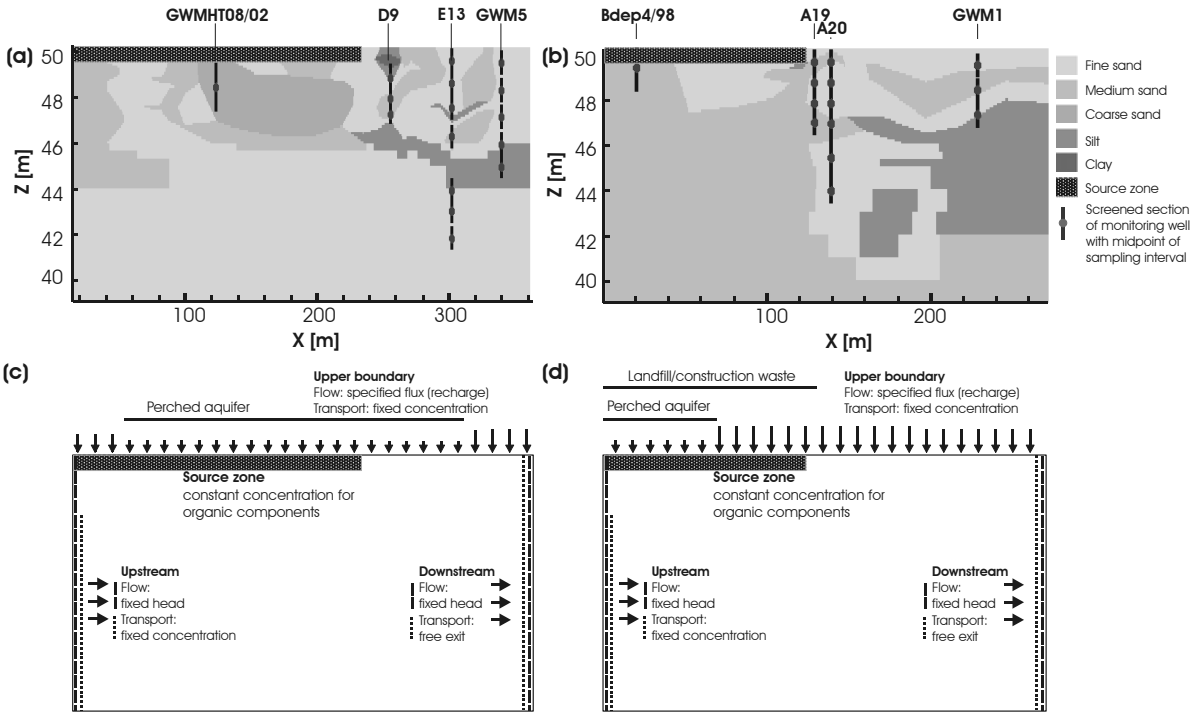

Figure 5.9. Schematic representations of the model transects showing material distributions in the model domain, source zone positions and monitoring well positions for (a) the east transect and (b) the west transect. (c) and (d) show general schematics for flow and transport boundary conditions for the east and west transects respectively. The arrows at the upper boundaries are a qualitative representation of the groundwater recharge distribution. Details of the boundary conditions are given in Table 5.2.

The boundary conditions for the model domains are shown in Figure 5.9(c) and (d) and summarized in Table 5.3. For the steady-state flow models, the groundwater recharge distributions for the upper specified flux boundaries were taken from the existing three-dimensional flow model. The boundary heads and hydraulic conductivities for the five material types were then adjusted to calibrate the flow models to measured hydraulic heads along the transects.

The reactive transport models consider a non-depleting source of organic contaminants at constant concentrations and homogeneously distributed in a source zone in an initially pristine aquifer with background concentrations of electron acceptors, which are also present at fixed concentrations in groundwater flowing into the domain across the upstream boundary and in groundwater recharge entering the domain at the upper boundary. As the upstream boundaries are located within the source zone, no boundary concentrations were set for the uppermost 1.7 meters, where for the typical thickness of the contaminant plume

Table 5.2 General parameters for the reactive transport simulations

Parameter		Parameter Value			
		East transect		West transect	
Model Domain					
Domain dimensions	*x, z* [m]	365.0, 11.4		270.0, 11.3	
No. of volumes in grid	x, z, total	487, 53, 25811		533, 56, 29848	
Boundary conditions, steady-state flow					
Upstream, downstream: fixed head	[m H_2O]	50.31, 50.03 [a]		50.23, 49.95 [a]	
Upper surface: specified flow (groundwater recharge)	[mm/a]	x = 0 – 50m	115 [b]	x = 0 – 43m	50 [b]
		x = 50 – 323m	10 [b]	x = 43 – 191m	200 [b]
		x = 323 – 365m	160 [b]	x = 191 – 270m	160 [b]
Source zone dimensions					
$x_{min} - x_{max}$, thickness		0 – 235 m, 0.7 m		0 – 122 m, 0.7 m	
Physical parameters, porous media					
		Hydraulic conductivity $k_{xx} = k_{zz}$ [ms^{-1}] [a]	Effective porosity n_e [-] [c]	Hydraulic conductivity $k_{xx} = k_{zz}$ [ms^{-1}] [a]	Effective porosity n_e [-] [c]
Fine sand		3×10^{-5}	0.1	1×10^{-5}	0.1
Medium sand		7×10^{-4}	0.2	3.7×10^{-4}	0.2
Coarse sand		1.8×10^{-3}	0.2	-	-
Silt		1×10^{-6}	0.01	2.1×10^{-6}	0.01
Clay		1×10^{-7}	0.01	-	-
Free phase diffusion coefficient, aqueous phase	D_{aq} [m^2s^{-1}]	1.01×10^{-9} [d]			
Longitudinal dispersivity	α_L [m]	1.0 [e]			
Transverse vertical dispersivity	α_T [m]	0.01 [e]			

[a] calibrated value for the transect steady-state flow model
[b] taken from 3D flow model (Miles et al. 2007)
[c] based on published ranges for material types (McWorter and Sunada, 1977)
[d] weighted average value for simulated components
[e] assumed value

beneath the source zone it was assumed that no electron acceptors were present in the inflowing groundwater.

The four principal mono-aromatic hydrocarbon contaminants at the site, benzene, ethylbenzene, m/p-xylene and 124-trimethylbenzene and a bulk “dissolved organic carbon” (DOC) component were included in the simulations with four TEAPs; oxygen, sulfate and solid phase Fe(III) reduction and methanogenesis. Nitrate and manganese reduction were not included, as the available concentration data does not indicate that these are significant processes at the site. DOC was included as a bulk component representing soluble hydrocarbon components of the kerosene not explicitly considered in the simulations. The initial and boundary concentrations for all components in the simulations are given in Table 5.3. GC/MS analyses of kerosene samples from different parts of the site showed differences in the kerosene composition, while the equilibrium concentrations calculated on the basis of the analyses were found to be lower in many cases than the concentrations

Table 5.3 Component concentrations in groundwater recharge, source zone and background (inflow boundary concentrations and initial condition for pristine aquifer)

Component		Recharge water		Background (Pristine aquifer)	Distribution coefficient for linear sorption, K_d
		East transect	West transect		
O_2(aq)	mol L^{-1} (mg L^{-1})	3.8×10^{-4} (6.0) [a]	3.1×10^{-5} (0.5) [b] 3.8×10^{-4} (6.0) [c]	2.5×10^{-4} (6.0)	-
$Fe(OH)_3$(m)	[mg/g]	-	-	0.51	-
Fe^{2+}(aq)	mol L^{-1} (mg L^{-1})	-	-	-	2.0
SO_4^{2-}(aq)	mol L^{-1} (mg L^{-1})	1.6×10^{-4} (15.0) [a]	7.8×10^{-4} (75.0) [b] 1.6×10^{-4} (15.0) [c]	6.9×10^{-4} (66.0)	-
CH_4(aq)	mol L^{-1} (mg L^{-1})	-	-		-
Source zone concentrations					
Benzene	mol L^{-1} (mg L^{-1})	3.1×10^{-5} (2.4)	1.5×10^{-5} (1.5)	-	0.05
Ethylbenzene	mol L^{-1} (mg L^{-1})	6.6×10^{-6} (0.7)	6.6×10^{-6} (0.7)	-	0.5
m/p-Xylene	mol L^{-1} (mg L^{-1})	9.3×10^{-6} (1.0)	9.3×10^{-6} (1.0)	-	0.55
124-TMB	mol L^{-1} (mg L^{-1})	5.0×10^{-6} (0.6)	5.0×10^{-6} (0.6)	-	0.98
DOC	mol L^{-1} (mg L^{-1})	1.7×10^{-4} (5.0)	1.7×10^{-4} (5.0)	-	0.91

[a] *x = 240 – 365m*, mixed ground cover, concentrations assumed and adjusted in calibration. For $0 < x < 240m$ over the extent of the source zone and where recharge is low due to overlying aquitard, delivery of electron acceptors via infiltration was assumed to be insignificant.
[b] *x = 0 – 125m*, infiltration through landfill and above source zone. Low levels of O_2(aq) with elevated SO_4^2(aq) concentrations due to leaching from construction waste were assumed.
[c] *x = 125 – 270m*, mixed ground cover, concentrations assumed and adjusted in calibration.

detected in monitoring wells within the source zone, both of which point to spatial heterogeneity of the kerosene composition. Source zone concentrations for the four contaminants were hence calibrated in the simulations to reproduce measured concentrations in the source zone monitoring wells in the transects. The assumed concentration of DOC in the source zone was based on the sum of mole fraction weighted solubilities for compounds identified in GC/MS analysis of the kerosene found at the site excluding those explicitly considered in the model. The lateral and vertical extents of the source zones in the transects, $x = 0 - 235$ *m* and $x = 0 - 122$ *m* in the east and west transects respectively, with a thickness of 0.7 m, were based on data from the ROST survey.

Values of the distribution coefficient K_d used to represent linear sorption in the model were calculated for each component from the organic carbon-water partition coefficient K_{oc} and the average organic carbon content for 9 samples of aquifer material. The initial quantity of Fe(III) in the simulations corresponds to the average amorphous $Fe(OH)_3$ content of aquifer sediment samples determined by HCl extraction (Jahn, 2005b). Microbial microcosm experiments carried out with aquifer material from the site showed that of the total mineral and amorphous $Fe(OH)_3$ present, the amorphous form was bioavailable and completely utilised by the Fe(III) reducing bacteria found in the aquifer, while the crystalline forms

were barely utilised (Jahn, 2005a). There was a large variability in the amorphous Fe(III) contents determined for the 21 samples of aquifer material analysed, which did not show any trend that could be correlated to sampling locations (uncontaminated area, plume or source zone) or sediment type. Thus in the simulations an average value was used and a homogeneous distribution in the aquifer assumed. In using the average present-day Fe(III) content as an initial condition for the pristine aquifer, it is assumed that while the average Fe(III) content of the sediments has undoubtedly decreased due to iron reduction to date, this change is insignificant compared to the variance for the samples used to calculate the average. For the aqueous phase electron acceptors, the initial and upstream boundary concentrations correspond to concentrations found in groundwater samples outside the contaminated area, while the concentrations in groundwater recharge were calibrated.

5.6.1.2. Reaction system

The reactions considered in the simulations are shown in Table 5.4. Reactions are included for each of the five organic species with each of the TEAPs, with a mixture of Monod and first-order kinetics. Monod kinetics, which are a more accurate representation of biodegradation reactions than first-order kinetics where a wide range of substrate concentrations is to be considered, were applied for reactions with oxygen and sulfate. Methanogenesis, for which it was not necessary to consider the availability of electron acceptors, was simulated using first- order kinetics approximated by setting an extremely high value for the half saturation concentration in the Monod expression. De-gassing of methane, as well as secondary reactions that it may undergo, such as re-oxidation by ferric oxides or hydroxides (Baedecker et al., 1993), were not considered. On the basis of the laboratory microcosm experiments where it was found that the degradation of contaminants with Fe(III) reduction could be adequately described by a simple first-order kinetic expression, the reaction of aqueous phase substrates with Fe(III) was represented in the model as an aqueous phase process with first-order kinetics. Using a two-step approach, the mineral phase Fe(III) was considered as dissolving to produce an equivalent, immobile aqueous phase species which could then react with any of the aqueous phase substrates. A high dissolution rate was used to ensure that the dissolution step was not limiting for the reaction, while a low solubility and high non-kinetic distribution coefficient for linear sorption ensured that the aqueous phase Fe(III) species was effectively immobile but freely available for reactions. Aqueous phase Fe(II) ions produced by the reduction of Fe(III) minerals are known to take part in numerous secondary reactions, such as

Table 5.4 Reactions included in the reactive transport simulations. The kinetic parameters correspond to those in the generalized formulation of the reaction system for MIN3P (Equation 3.1). k_k^a is the calibrated reaction rate [mol L^{-1} H$_2$O s^{-1}] or [s^{-1}], $K_{kj}^{a,mo}$ the half saturation constant for substrate and electron acceptor [mol L^{-1}], with the values in brackets being the value for the electron acceptor in each case. $K_{kj}^{a,in}$ is the aqueous or mineral inhibition constant, [mol L^{-1}] for aqueous or [-] for mineral phase. (aq) denotes a dissolved aqueous species, (m) a mineral.

Reactions	k_k^a mol L^{-1} s^{-1}	$K_{kj}^{a,mo}$ mol L^{-1}	$K_{kj}^{a,in}$ mol L^{-1}
$C_6H_6 + 7.5O_2(aq) + 3H_2O \rightarrow 6CO_3^{2-} + 12H^+$	8.0×10^{-11}	2.2×10^{-6} (7.8×10^{-6})	
$C_6H_5(C_2H_5) + 10.5O_2(aq) + 3H_2O \rightarrow 8CO_3^{2-} + 16H^+$	8.0×10^{-11}	3.8×10^{-7} (7.8×10^{-6})	
$C_6H_4(CH_3)_2 + 10.5O_2(aq) + 3H_2O \rightarrow 8CO_3^{2-} + 16H^+$	8.0×10^{-11}	6.0×10^{-7} (7.8×10^{-6})	-
$C_9H_{12} + 12O_2(aq) + 3H_2O \rightarrow 9CO_3^{2-} + 18H^+$	8.0×10^{-11}	2.8×10^{-7} (7.8×10^{-6})	
$CH_2O + O_2(aq) \rightarrow CO_3^{2-} + 2H^+$	8.0×10^{-11}	3.0×10^{-5} (7.8×10^{-6})	
$C_6H_6 + 30Fe(OH)_3(m) + 48H^+ \rightarrow 6CO_3^{2-} + 30Fe^{2+}(aq) + 72H_2O$	1.03×10^{-8}	1.0	
$C_6H_5(C_2H_5) + 42Fe(OH)_3(m) + 68H^+ \rightarrow 8CO_3^{2-} + 42Fe^{2+}(aq) + 102H_2O$	0.55×10^{-8}	1.0	
$C_6H_4(CH_3)_2 + 42Fe(OH)_3(m) + 68H^+ \rightarrow 8CO_3^{2-} + 42Fe^{2+}(aq) + 102H_2O$	1.03×10^{-8}	1.0	3.1×10^{-7} [a]
$C_9H_{12} + 48Fe(OH)_3(m) + 78H^+ \rightarrow 9CO_3^{2-} + 48Fe^{2+}(aq) + 117H_2O$	1.13×10^{-8}	1.0	
$CH_2O + 4Fe(OH)_3(m) + 6H^+ \rightarrow CO_3^{2-} + 4Fe^{2+}(aq) + 10H_2O$	0.67×10^{-8}	1.0	
$C_6H_6 + \frac{15}{4}SO_4^{2-}(aq) + \frac{30}{4}H^+ \rightarrow 6CO_3^{2-} + \frac{15}{4}H_2S(aq) + 3H_2O$	5×10^{-10}	2.2×10^{-6} (6.9×10^{-5})	
$C_6H_5(C_2H_5) + \frac{21}{4}SO_4^{2-}(aq) + \frac{42}{4}H^+ \rightarrow 8CO_3^{2-} + \frac{21}{4}H_2S(aq) + 5H_2O$	3×10^{-9}	3.8×10^{-7} (6.9×10^{-5})	
$C_6H_4(CH_3)_2 + \frac{21}{4}SO_4^{2-}(aq) + \frac{42}{4}H^+ \rightarrow 8CO_3^{2-} + \frac{21}{4}H_2S(aq) + 5H_2O$	2.6×10^{-10}	6.0×10^{-7} (6.9×10^{-5})	3.1×10^{-7} [a] 8×10^{-7} [b]
$C_9H_{12} + 6SO_4^{2-}(aq) + 12H^+ \rightarrow 9CO_3^{2-} + 6H_2S(aq) + 6H_2O$	1.6×10^{-10}	2.8×10^{-7} (6.9×10^{-5})	
$CH_2O + \frac{1}{2}SO_4^{2-}(aq) + H^+ \rightarrow CO_3^{2-} + \frac{1}{2}H_2S(aq) + H_2O$	3×10^{-9}	3.0×10^{-5} (6.9×10^{-5})	
$C_6H_6 + \frac{18}{4}H_2O \rightarrow \frac{15}{4}CH_4 + \frac{9}{4}CO_2$	6×10^{-9}	1.0	
$C_6H_5(C_2H_5) + \frac{22}{4}H_2O \rightarrow \frac{21}{4}CH_4 + \frac{11}{4}CO_2$	6×10^{-8}	1.0	3.1×10^{-7} [a]
$C_6H_4(CH_3)_2 + \frac{22}{4}H_2O \rightarrow \frac{21}{4}CH_4 + \frac{11}{4}CO_2$	1×10^{-7}	1.0	5×10^{-4} [b] 5×10^{-6} [c]
$C_9H_{12} + 6H_2O \rightarrow 6CH_4 + 3CO_2$	1×10^{-7}	1.0	
$CH_2O + \frac{1}{2}H_2O \rightarrow \frac{1}{2}CH_4 + \frac{1}{2}CO_2$	1×10^{-8}	1.0	
$Fe^{2+}(aq) + \frac{1}{4}O_2 + \frac{10}{4}H_2O \rightarrow Fe(OH)_3(m) + 2H^+$	1.0	1.0	-
$Fe^{2+}(aq)$ 1st order decay	2×10^{-8} [d]	-	-

[a] Inhibition constant for inhibition by O_2(aq)
[b] Inhibition constant for inhibition by $Fe(OH)_3$(am), units [-]
[c] Inhibition constant for inhibition by SO_4^{2-}(aq)
[d] First order decay rate applied to Fe^{2+}(aq), units [s^{-1}]

precipitation as Fe(II) sulfides or re-oxidation to Fe(III) (Tuccillo et al., 1999; Vencelides et al., 2007), and ion exchange processes (Appelo et al., 1999; Freedman et al., 1994) that limit their transport away from areas where Fe(III) reduction is active. In the simulations the

complex geochemistry of Fe(II) was simplified to two processes; re-oxidation of Fe(II) to Fe(III) in the presence of oxygen, and a first order decay term applied to Fe(II) to represent the various other sink reactions. Ion exchange processes were considered by including linear sorption of Fe(II) with an assumed distribution coefficient (see Table 5.3). The reaction of Fe(II) with oxygen was considered as a separate process, as it was found that the resulting depletion of oxygen affected the transport of the organic contaminants in the simulations. The inhibition terms, K_{kj}^{in} in the generalised reaction scheme (see Equation 3.1) were used to control switching between the different TEAPs by inhibiting the reactions to various degrees in the presence of other electron acceptors. Fe(III) reduction was considered to be inhibited by the presence of oxygen, sulfate reduction by oxygen and the mineral phase Fe(III), and methanogenesis by oxygen, Fe(III) and sulfate.

5.6.2. Results and discussion (reactive transport model)

The reactive transport models for the two transects share a single reaction scheme, developed model of the east transect. The model was manually calibrated to observed concentrations along the transect by adjusting reaction rates, inhibition constants and the concentrations of electron acceptors in groundwater recharge. The reaction scheme was then implemented in the model for the west transect, which was calibrated to observed concentrations by adjusting only the concentrations of electron acceptors in groundwater recharge. The parameters for the calibrated reaction scheme are given in Table 5.4. Half saturation constants for the Monod controlled reactions were assigned assumed values of 10% of the maximum or background concentration for the substrates and electron acceptors respectively, with the aim of ensuring that the reaction kinetics would not tend too strongly to first or zero-order over the concentration ranges used. For aerobic degradation, which for mono-aromatic hydrocarbons is rapid compared to anaerobic processes, a maximum utilisation rate k_k^a was assigned such that the maximum reaction rates in the simulations were significantly higher than those for the anaerobic processes. For Fe(III) reduction, laboratory determined first-order degradation rates for the organic components were found to be too high when applied in the simulations, and so values for the rates were determined in the calibration, with an average rate used for DOC. The relative magnitudes of the rates, which were similar for all of the compounds except ethylbenzene, which was found to be significantly less degradable, were not changed in the calibration, but the absolute values for the calibrated rates were two orders of magnitude lower than those determined in the laboratory. For sulfate reduction, maximum utilisation rates were determined by calibration,

resulting in similar rates for benzene, m/p-xylene and 124-TMB and a somewhat higher rate for ethylbenzene. First-order rates for methanogenesis were also determined by calibration, however, as it is widely reported that benzene is poorly degraded in comparison to other mono-aromatic compounds under methanogenic conditions (Aronson and Howard, 1997), applying the condition that the rate for benzene should be lower than for the other compounds. The calibrated rates for the remaining compounds were somewhat higher than the rates for Fe(III) degradation, for which a similar trend is seen in the data reported by Aronson and Howard (1997). For the secondary reactions of Fe(II), it was assumed that in comparison to the biodegradation reactions, oxidation by dissolved oxygen was effectively an instantaneous process. The rate for the first-order decay of Fe(II) was determined by calibration, and was found to be important for reproducing the observed concentrations downstream from the source zone, indicating that secondary reactions such as sulfide formation are a significant sink for Fe(II) downstream from the source zone.

Similarly to Brun et al. (2002), the inhibition constants, which control the degree of separation or overlap of the TEAPs, were found to be critical for reproducing the measured concentrations and the different TEAP distributions in the two transects. For inhibition of the anaerobic processes by oxygen, a very low concentration was used for the inhibition constant, ensuring that the reactions were suppressed until dissolved oxygen concentrations approached zero. Using inhibition by Fe(III) and sulfate it was possible to reproduce the observed situation where high concentrations of methane or sulfate are found together with high Fe(II) concentrations, but high concentrations of methane and sulfate are not found together. The calibrated inhibition constants for inhibition of sulfate reduction and methanogenesis allow both processes to occur while mineral phase Fe(III) is present, with sulfate reduction inhibited significantly more than methanogenesis, while methanogenesis is additionally strongly inhibited by sulfate. Used in this way, the inhibition constants act as a lumped parameter combining a number of factors that may be responsible for the apparent overlap of the redox processes, such as the small spatial scale of redox zones, large sampling volumes or transport of redox species away from active zones. The electron acceptor concentrations applied to groundwater recharge in the simulations are given in Table 5.3. Where the main aquifer was overlain by the perched aquifer and recharge to the main aquifer is minimal, it was assumed that the supply of electron acceptors was insignificant. Over the extent of the source zone it was assumed that recharge reaching the main aquifer would be anoxic due to biodegradation in the unsaturated zone, which has been

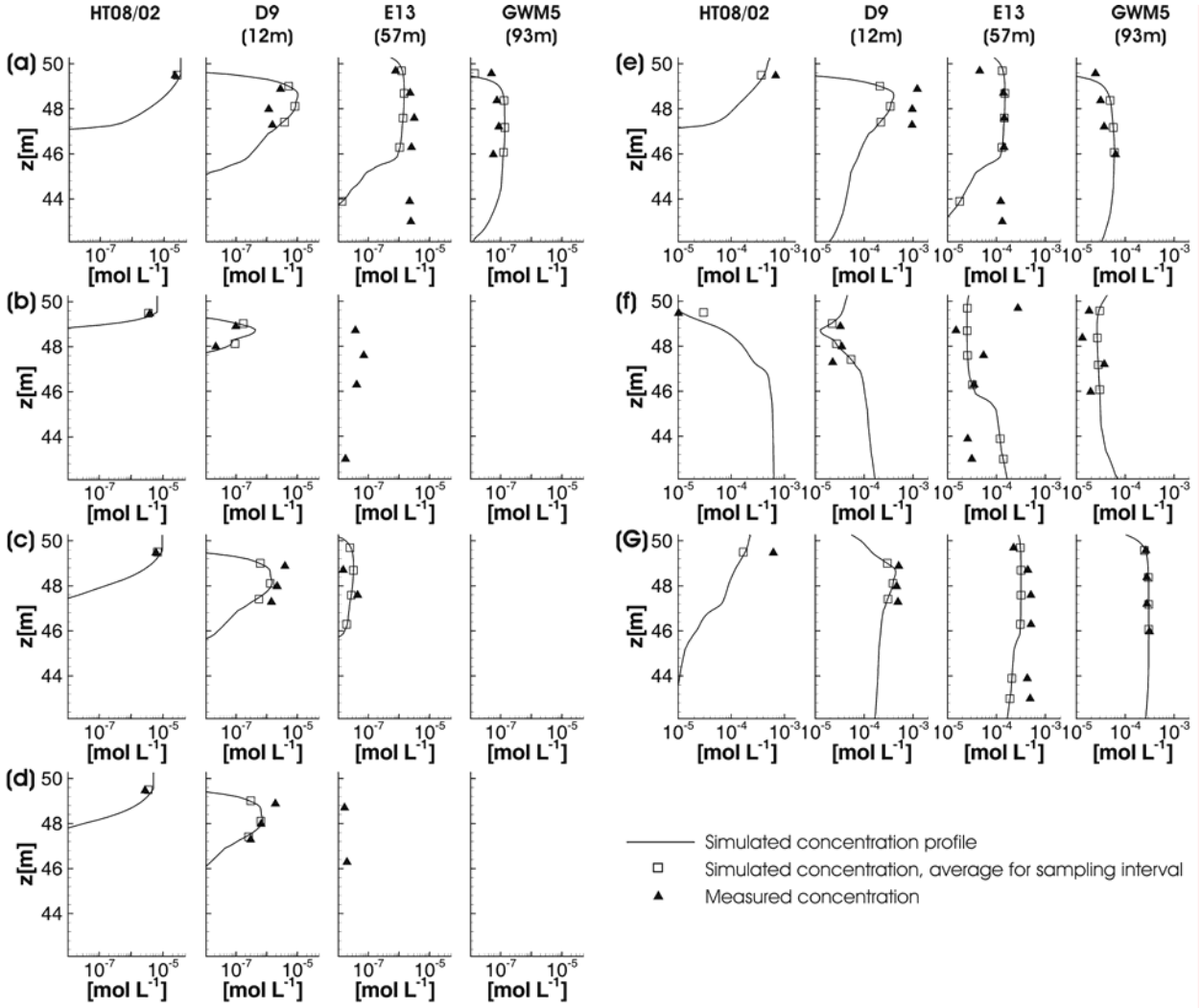

Figure 5.10 Simulated and measured component concentrations for the east transect. (a) benzene, (b) ethylbenzene, (c) m/p-xylene, (d) 124-TMB, (e) Fe(II), (f) sulfate, (g) methane. The downstream distances from the end of the source zone are given below the well names.

shown to be the case for LNAPL contaminated sites (Chaplin et al., 2002; Essaid et al., 2003). Elsewhere the oxygen concentration was assumed to be the same as the background concentration in the aquifer. The concentrations of sulfate at the site were assumed to be variable depending on the ground cover, with high concentrations due to leaching from construction waste in the landfill area of the west transect, and lower concentrations in wooded areas (cf. Figure 5.5(b)).

The simulated and measured concentrations of the organic components and anaerobic redox species at monitoring wells in the east and west transects are shown in Figure 5.10 and Figure 5.11, respectively. The simulated concentrations shown are vertical profiles after 40 years simulation time, which is considered to be a reasonable current age for the

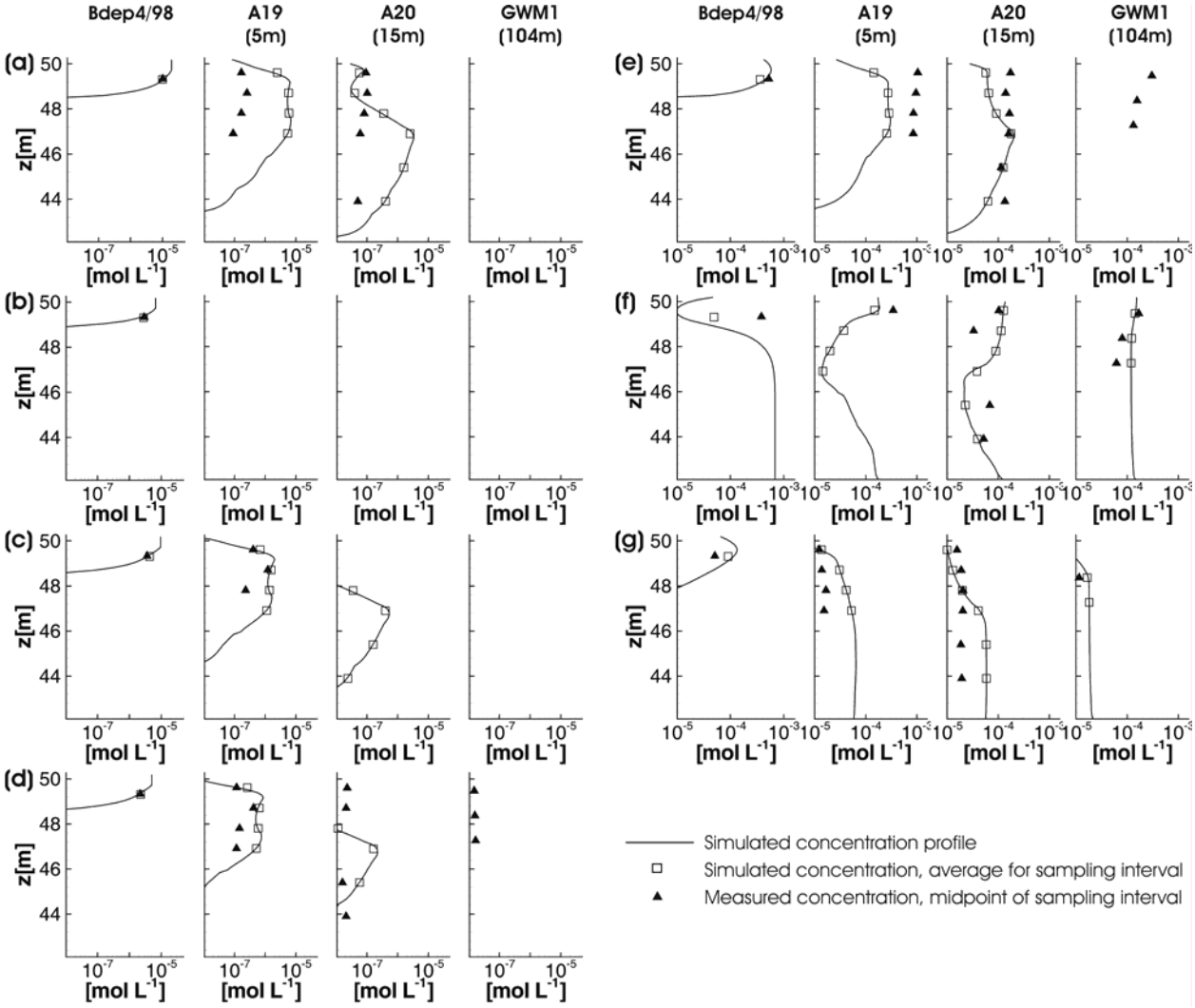

Figure 5.11 Simulated and measured component concentrations for the west transect. (a) benzene, (b) ethylbenzene, (c) m/p-xylene, (d) 124-TMB, (e) Fe(II), (f) sulfate, (g) methane. The downstream distances from the end of the source zone are given below the well names.

contamination, with average concentrations shown for the screened sampling intervals. The locations of the monitoring wells in the transects can be seen in Figure 5.7 and Figure 5.9. From the measured contaminant concentrations, it can be seen that in the east transect, benzene forms the longest plume, being the only one of the four contaminants detected at GWM5, the furthest downstream of the four monitoring wells. The remaining contaminants all have similar plume lengths, being present at significant concentrations close to the source zone at D9, and at low concentrations 50 m further downstream at E13. In the west transect a quite different situation is seen, with shorter plumes for all of the contaminants. Generally the contaminant concentrations fall very rapidly downstream from the source zone; ethylbenzene is not detected in any of the downstream monitoring wells, and at A20 only benzene and 124-TMB are present at low concentrations below 10 µg/l. None of the contaminants are detected at GWM1, around 100 m downstream from the source zone, with

the exception of 124-TMB, where the concentrations of 1-2 µg/l are close to the detection limit.

The measured contaminant concentrations for both transects are reproduced quite well in the simulations. For the east transect, a generally good match is seen between the measured and simulated concentrations for all four compounds. The model successfully reproduces the observed situation with the long benzene plume and shorter plumes for the other compounds but somewhat underestimates the plume length for ethylbenzene, with simulated concentrations at E13 much lower than the measured. The concentrations for benzene in the lowest sampling intervals at E13, which lie below a thick silt layer, are also underestimated in the model. A reasonable match is also seen between simulated and measured concentrations for the west transect, with the model again reproducing the general situation with no downstream plume for ethylbenzene and short plumes for the other compounds. Concentrations are overestimated close to the source zone for benzene at A19 and for benzene, xylene and TMB in the lower intervals at A20.

The concentrations of the redox species are also reproduced quite well in the simulations. In the east transect, the situation with low sulfate concentrations and high Fe(II) and methane concentrations is reproduced quite successfully, although the simulated concentrations of methane beneath the source zone at GWMHT8/02 are lower than the measured, as are the Fe(II) concentrations adjacent to the source zone at D9. In the west transect the model reproduces the general features of the observed situation with higher sulfate and lower methane concentrations quite well. The simulated methane concentrations are generally slightly higher than the measured, while the simulated sulfate concentration below the source zone at Bdep4/98 is significantly lower than the measured value. For Fe(II) the simulated concentrations adjacent to the source zone at A19 are again lower than the measured. That this is the case in both transects suggests that the first-order decay term applied to Fe(II) to account for the various geochemical sinks may be resulting in too much mass loss at higher concentrations. The model could also not account for the measured Fe(II) concentrations at GWM1, which are equal to or higher than those at A20. It is possible in this case that there is a separate source of Fe(II), possibly related to the landfill.

To look at the medium to long-term evolution of conditions in the two transects, the calibrated models were run for a period of 400 years. Although it is considered likely that for such a time scale particularly the soluble MAHs will be depleted in the source zone and

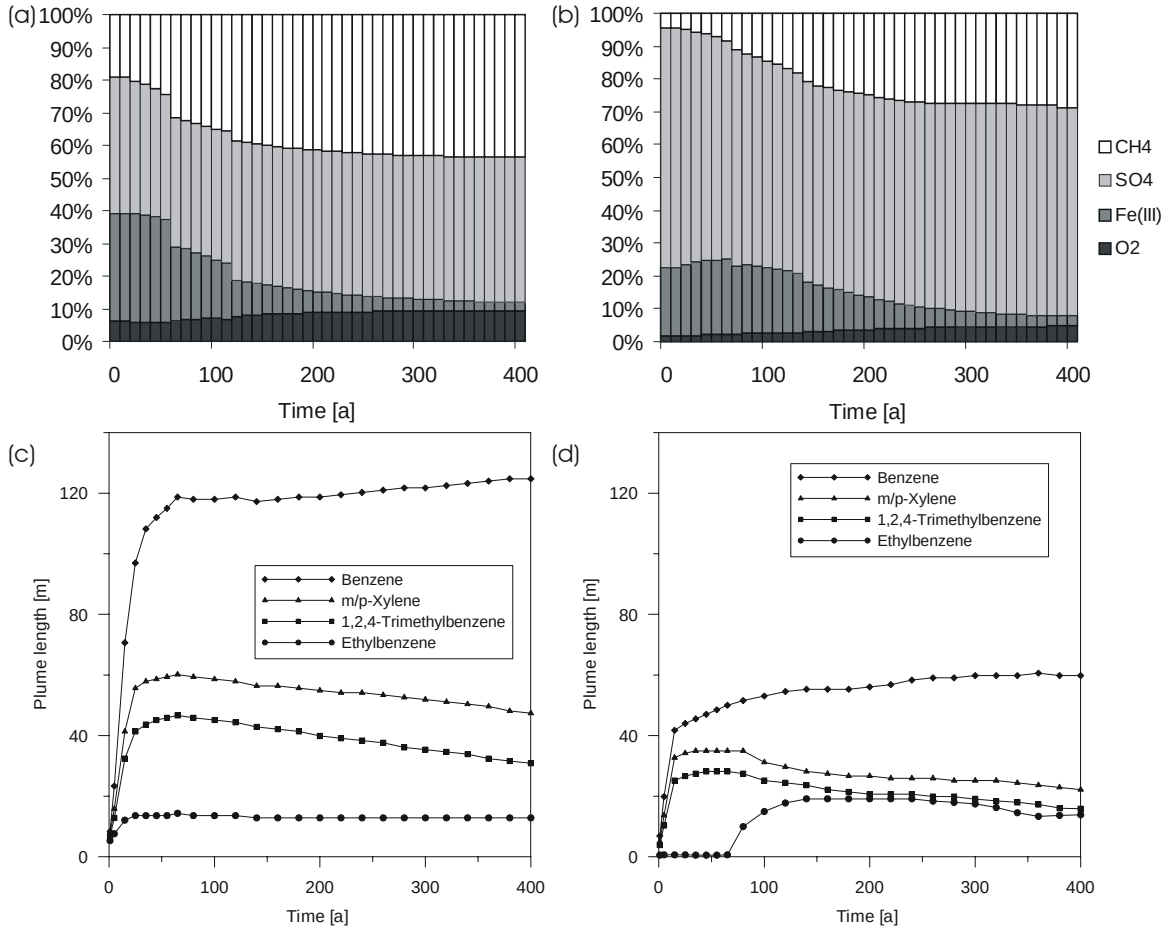

Figure 5.12 Contributions of the four TEAPs to the overall degradation of the organic components and plume lengths from the downstream end of the source zone during the simulations. TEAP contributions are expressed as the rate of organic component mass loss due to each TEAP [moles T^{-1}] as a percentage of the total rate of organic component mass loss due to all TEAPs [moles T^{-1}] for (a) the east transect and (b) the west transect. The plume lengths (c) and (d) for the east and west transects respectively are defined by a 5µg/l concentration threshold.

the contaminant emission will decrease accordingly, a non-depleting source at constant concentration was assumed, being a conservative approach in terms of MNA.

Figure 5.12 shows the temporal development of plume lengths from the downstream edge of the source zone for the two transects, together with the contributions of the four TEAPs to the total degradation. The TEAP contributions (Figure 5.12(a) and (b)) show that anaerobic processes dominate the degradation in both transects throughout the simulated period, with the contribution from aerobic degradation at the plume fringes less than 10%. Of the anaerobic TEAPs, sulfate reduction accounts for the largest fraction of the total degradation, remaining fairly constant at about 50% of the total in the east transect and 70% in the west

transect, which is comparable to a large number of field studies reported by Wiedermaier et al. (1999). In the east transect this occurs principally at the upstream plume fringe, where there is a supply of sulfate from water entering the model domain across the upstream boundary. In the west transect the supply of sulfate from groundwater recharge accounts for the additional contribution to degradation. This additional supply of sulfate is also responsible for the smaller contribution of methanogenesis to the degradation in the west transect than the east, as it inhibits methanogenesis in the source zone. The contribution of Fe(III) reduction is similar in both transects, though slightly higher in the east due to the larger source zone, and decreases over time as Fe(III) becomes depleted in the source zone. As the iron becomes depleted, the contribution of methanogenesis increases in the source zone and body of the plume where the supply of sulfate, which would otherwise be the next TEAP in the series, is restricted. Figure 5.12(c) shows that in the east transect plumes develop rapidly for all four contaminants, reaching maximum lengths of 10 to 50 m within 50 years for ethylbenzene, xylene and 124-TMB, while the benzene plume reaches a length of 120 m. After 50 years, as Fe(III) becomes depleted in the source zone and conditions become more methanogenic, a gradual increase is seen in the plume length for benzene, which degrades less well under methanogenic conditions, while the plumes for xylene and 124-TMB, which in the calibrated reaction scheme degrade more rapidly under methanogenesis, begin to shrink. In the west transect, where conditions are initially less methanogenic and electron acceptors are supplied by groundwater recharge, shorter plumes develop initially for benzene, xylene and 124-TMB, with the same behaviour seen as Fe(III) becomes depleted in the source zone, in that the plume lengths increase for benzene and decrease for xylene and 124-TMB. For ethylbenzene, which in the calibrated reaction scheme is more degradable than the other contaminants under sulfate reducing conditions, a plume only develops after 80 years, once sulfate concentrations have been significantly depleted in the wake of the other plumes. In the east transect, where sulfate is rapidly depleted, the ethylbenzene plume develops from the beginning of the simulation. Changes in contaminant plume length in response to changing TEAPs as Fe(III) becomes depleted have been reported at field sites and in modelling studies (Chapelle et al., 2002; Cozzarelli et al., 2001; Essaid et al., 2003), with increases in plume lengths for benzene and ethylbenzene. The simulations described in this work similarly show this behaviour in the medium to long-term under the assumption of steady state conditions with a constant contaminant source. They also show the converse may also occur in that a contaminant that

degrades more rapidly under a subsequent TEAP exhibits plume shrinkage as Fe(III) becomes depleted.

5.7. Summary and Conclusions

A detailed three dimensional groundwater flow model was developed for the former tankfarm at Flughafen Brand from a high resolution geological dataset using the GeoSys/RockFlow finite element code. A GIS-based conceptual site model was developed based on the geological and hydrogeological data. New software tools were developed and implemented for the translation of the complex conceptual site model into a numerical finite element model. Using this approach, the translation of the highly detailed and complex conceptual site model to the numerical model could be achieved with a high degree of accuracy, and without the need for structural simplification.

Calibration of the groundwater flow model using readily available automated calibration software produced a good agreement between modelled and measured hydraulic head data with reasonable values for the optimised parameters. The parameters identified in the calibration process could support hypotheses regarding the hydrogeological situation at the site, specifically the influence of groundwater recharge on the local flow situation.

The detailed three-dimensional flow model and the identified parameter values provided an essential basis for the subsequent reactive transport models developed to investigate observed differences in contaminant plume lengths and TEAP distributions in different parts of the site. Models were developed for two transects with a reaction scheme calibrated to measured contaminant and redox species concentrations for one of the transects. Using the reaction scheme calibrated for one transect it was possible to reasonably reproduce measured concentrations in the second transect. The observed overlapping of anaerobic TEAPs at the site could be successfully simulated using Monod-type inhibition terms. With the same reaction scheme used in both models, the differences in contaminant and TEAP distributions for the two transects can be attributed to hydrogeological and hydrological differences. In particular the supply of electron acceptors in groundwater recharge was found to play a critical role in the distribution of TEAPs at the site, with more methanogenesis and less sulfate reduction in the transect where an overlying perched aquifer prevented recharge to the main aquifer. This resulted in longer contaminant plumes, particularly for benzene, which degrades poorly under methanogenic conditions, compared to the second transect where the supply of sulfate in groundwater recharge inhibited

methanogenesis in the source zone and allowed more sulfate reduction in the plume. Long-term simulations for the two transects showed that the distribution of TEAPs and the contaminant plume lengths are not steady state, with benzene plume lengths increasing as Fe(III) is depleted in the vicinity of the source zone and conditions evolve from iron reducing to methanogenic. This transient behaviour in the medium to long-term is an important factor to consider for the implementation of MNA at the site.

6. General summary and conclusions

Numerical modelling studies were carried out for three kerosene-contaminated sites near Berlin, Germany. The three sites are similar in that they all involve a historical release of kerosene at the ground surface leading to contamination of a sandy-silty aquifer, but differ in the quantity and distribution of the kerosene in the subsurface, and were used as case studies to consider three conceptual categories of LNAPL contamination. Different modelling approaches were applied at the sites, considering different processes and focussing on different aspects of the situation in each case.

For the first category, represented by the field site TL1, which considers an immobile LNAPL source zone at low residual saturation in the capillary fringe, a multi-component model was used to simulate contaminant emission and transport in the saturated and unsaturated zones with a transient source composition. Simple geological heterogeneity was included in the unsaturated zone. Biodegradation was simulated using a simple first-order kinetic approach. Multiple scenarios were used to determine the influence of different parameters on contaminant emission to the aqueous and gaseous phases, aqueous phase plume development and the source lifetime. The simulations showed that of the total contaminant emission about 80% was to the aqueous phase, and 20% to the gaseous phase. For most of the contaminants the rate of emission remained fairly constant over a 50 year simulation period, with only highly soluble and volatile components with small mass fractions becoming depleted in the source. Steady-state and shrinking plumes were seen for all components in the simulations. Analysis of the scenarios simulated showed that the contaminant emission was strongly affected by the lateral extent of the source zone, the rate of groundwater recharge, flow velocity and degradation rates, but not by the source mass or NAPL distribution, which were important factors for the source lifetime. The maximum aqueous phase plume length was only significantly affected by groundwater flow velocity and degradation rates, with the time taken to reach the maximum length depending only on the degradation rate.

For the second category of LNAPL contamination, represented by the field site TL2, which considers LNAPL at high saturations forming mobile pools in the capillary fringe, a compositional multiphase modelling approach was used to estimate contaminant emission. The infiltration and spreading of the kerosene, simplified to a single NAPL component, was simulated for multiple realisations of statistically generated geological heterogeneity. The results demonstrated that the simulated LNAPL distribution is massively sensitive to

permeability and porosity distributions, which severely limits the usefulness of such a model in any deterministic role. It was, however, possible to derive a simple linear relationship between the lateral extent of the LNAPL source and the emission to the aqueous phase, which was shown to be independent of the distribution of the LNAPL saturations or the source zone thickness. Groundwater recharge rates and horizontal flow velocity in the aquifer were shown to be controlling factors for the relationship.

For the third category of LNAPL contamination, represented by the field site Brand, which considers a large but immobile LNAPL pool with an extensive and well established contaminant plume, a detailed geological and hydrogeological model was developed and used as a basis for a reactive transport model considering multiple contaminants and electron acceptors. The hydrogeological model showed that the flow situation at the site is strongly influenced by a hanging aquifer system intercepting groundwater recharge. In the reactive transport simulations it was found that the interception of groundwater recharge limits the supply of electron acceptors to the source zone and contaminant plume, which in turn affects the distribution of TEAPs at the site. The distribution of TEAPs has a direct effect on the downstream plume lengths for the aqueous phase contaminants. The inclusion of Fe(III) as an immobile solid phase electron acceptor resulted in a transient TEAP distribution in the simulations, which led to changes in plume lengths for some components as Fe(III) became depleted.

Overall, the three cases studies serve to highlight some important points for consideration in modelling LNAPL contaminated sites. As well as demonstrating how the modelling approach used can influence the model outcome, the studies show that different questions or tasks necessitate different modelling approaches. The case studies TL1 and TL2 both showed that in terms of the source zone geometry only the lateral extent is of significance for contaminant emission; the thickness of the source zone and the distribution of the NAPL saturations in the source, as well as the source mass are of little relevance for contaminant emission. More important is the definition of the hydrogeological and hydrological conditions, particularly groundwater flow velocity and recharge rates. All three case studies showed that groundwater recharge is one of the most important parameters to consider, especially for large area LNAPL contaminations. On the one hand it plays a significant role in contaminant emission, while on the other hand, as a source of electron acceptors it can be a key determining factor for contaminant degradation. Comparing the case studies for TL1 and Brand, it can be seen how the processes considered in the modelling approach can affect the model outcome. Representing degradation processes with simple first-order kinetics is a

widely used approach, and attractive in that it there are relatively few parameters to consider and degradation rates can be directly estimated from field data. Using this approach results in steady-state plumes as long as the input from the source is constant. A more complex representation of the degradation processes, however, may show a quite different picture, especially if solid-phase electron acceptors are shown or assumed to play a significant role and included in the reaction scheme, with transient redox zonation and non-steady-state plume behaviour. Furthermore, where in the first-order kinetic approach an increase in groundwater recharge will result in an increase in plume lengths due to an increase in contaminant emission, for a more complex reaction scheme where electron acceptors are considered, an increase in recharge can lead to a decrease in plume length by increasing the supply of electron acceptors to the plume. Factors such as this are important to consider in developing a modelling approach for a contaminated site.

References

Appelo, C.A.J., Drijver, B., Hekkenberg, R. and de Jonge, M., 1999. Modeling in situ iron removal from ground water. Ground Water, 37(6): 811-817.

Aronson, D. and Howard, P.H., 1997. Anaerobic biodegradation of organic chemicals in groundwater: a summary of field and laboratory studies. SRC TR-97-0223F, Syracuse Research Corporation.

Baedecker, M.J., Cozzarelli, I.M., Eganhouse, P., Siegel, D.I. and Bennett, P.C., 1993. Crude oil in a shallow sand and gravel aquifer-III- Biogeochemical reactions and mass balance modeling in anoxic groundwater. Applied Geochemistry, 8(6): 569-586.

Bagrov, N.A., 1953. O srednem mnogoletnem isparenii s poverchnosti susi (On multi-year average of evapotranspiration from land surface). Meteorog. i Gridrolog. (Russ.), 10.

Bear, J., 1972. Dynamics of fluids in porous media. Elsevier, New York.

Beinhorn, M., 2005. Contributions to computational hydrology: Non-linear flow processes in subsurface and surface hydrosystems. PhD Thesis, Universität Tuebingen, Tuebingen, Germany.

Berglund, S., 1997. Aquifer remediation by pumping: A model for stochastic-advective transport with nonaqueous phase liquid dissolution. Water Resour. Res., 33(4): 649-661.

Bjerg, P.L., Rügge, K., Pederson, J.K. and Christensen, T., 1995. Distribution of redox-sensitive groundwater quality parameters downgradient of a landfill (Grinsted, Denmark). Environ. Sci. Technol, 29(5): 1387-1394.

Brun, A., Engesgaard, P., Christensen, T. and Rosbjerg, D., 2002. Modelling of transport and biogeochemical processes in pollution plumes: Vejen landfill, Denmark. Journal of Hydrology, 256: 228-247.

Buscheck, T.E. and Alcantar, C.M., 1995. Regression Techniques and Analytical Solutions to Demonstrate Intrinsic Bioremediation. In: R.E. Hinchee, J.T. Wilson and D.C. Downey (Editors), In-Situ and On-Site Bioreclamation Symposium. Battelle Press, San Diego, California, pp. 109-116.

Carrera, J. and Neuman, S., 1986. Estimation of aquifer parameters under transient and steady state conditions. Water Resour. Res., 22(2): 199-242.

Chapelle, F.H., Bradley, P.M., Lovley, D.R., O'Niell, K. and Landeyer, J.E., 2002. Rapid evolution of redox processes in a petroleum hydrocarbon-contaminated aquifer. Ground Water, 40(4): 353-360.

Chaplin, B.P., Delin, G.N., Baker, R.J. and Lahvis, M.K., 2002. Long-term evolution of biodegradation and volatilisation rates in a crude oil-contaminated aquifer. Bioremediation J., 6(3): 237-255.

Chrysikopoulos, C.V., Hsuan, P., Fyrillas, M.M. and Lee, K.Y., 2003. Mass transfer coefficient and concentration boundary layer thickness for a dissolving NAPL pool in porous media. Jounal of Hazardous Materials, B97: 245-255.

Cozzarelli, I.M., Bekins, B.A., Baedecker, M.J., Aiken, G.R., Eganhouse, R.P. and Tuccillo, M.E., 2001. Progression of natural attenuation processes at a crude-oil spill site: I. geochemical evolution of the plume. Journal of Contaminant Hydrology, 53: 369-385.

Dillard, L.A., Essaid, H.I. and Herkelrath, W.N., 1997. Multiphase flow modelling of a crude-oil spill site with a bimodal permeablity distribution. Journal of Contaminant Hydrology, 48(1-2): 89-119.

Doherty, J., 2004. PEST. Watermark Computing, Corinda, Australia.

Domenico, P.A. and Schwartz, F.W., 1990. Physical and chemical hydrogeology. John Wiley & Sons Inc., New York.

Eberhardt, C. and Grathwohl, P., 2002. Time scales of organic contaminant dissolution from complex source zones: coal tar pools vs. blobs. Journal of Contaminant Hydrology, 59(1-2): 45-66.
Essaid, H.I., Cozzarelli, I.M., Eganhouse, R.P., Herkelratha, W.N., Bekinsa, B.A. and Delinc, G.N., 2003. Inverse modeling of BTEX dissolution and biodegradation at the Bemidji, MN crude-oil spill site. Journal of Contaminant Hydrology, 67: 269-299.
Essaid, H.I., Herkelrath, W.N. and Hess, K.M., 1993. Simulation of fluid distributions observed at a crude oil spill site incorporating hysteresis, oil entrapment, and spatial variability of hydraulic properties. Water Resour. Res., 29(6): 1753-1770.
Essaid, H.I. and Hess, K.M., 1993. Monte Carlo simulations of multiphase flow incorporating spatial variability of hydraulic properties. Ground Water, 31(1): 123-134.
ESTI, 1990a. SOILPROP. Environmental Systems and Technologies Inc., Virginia, USA.
ESTI, 1990b. SPILLVOL. Environmental Systems and Technologies Inc., Virginia, USA.
Forsyth, P.A., Unger, A.J.A. and Sudicky, E.A., 1998. Nonlinear iteration methods for non-equilibrium multiphase subsurface flow. Advances in Water Resources, 21: 443-449.
Freedman, Y.E., Magaritz, M., Long, G.L. and Ronen, D., 1994. Interaction of metals with mineral surfaces in a natural groundwater environment. Chemical Geology, 116: 111-121.
Frind, E.O., Molson, J.W., Schirmer, M. and Guiguer, N., 1999. Dissolution and mass transfer of multiple organics under field conditions: The Borden emplaced source. Water Resour. Res., 35(3): 683-694.
Fuller, E.N., Schettler, P.D. and Giddings, J.C., 1966. A new method for prediction of binary gas-phase diffusion coefficients. Ind. Eng. Chem., 58: 19-27.
Gaganis, P., Karapanagioti, H.K. and Vasilis, B.N., 2002. Modeling multicomponent NAPL transport in the unsaturated zone with the constituent averaging technique. Advances in Water Resources, 25: 723-732.
Glugla, G. and Müller, E., 1997. Grundwasserneubildung als Komponente der Abflußbildung. Freiburger Schriften zur Hydrologie, 5.
Grathwohl, P., 1998. Diffusion in Natural Porous Media: Contaminant Transport, Sorption, Desorption and Dissolution Kinetics. Kluwer Academic Publishers, Boston, 228 pp.
Guiguer, N. and Frind, E.O., 1994. Dissolution and mass transfer processes for residual organics in the saturated groundwater zone. In: S. Dracos (Editor), Transport and Reactive Processes in Aquifers. Balkema, Rotterdam, pp. 475-480.
Hazen, A., 1911. Discussion: Dams on sand foundations. Transactions, American Society of Civil Engineers, 73: 199.
Hill, M.C., 1992. A computer program (MODFLOWP) for estimating parameters of a transient, three-dimensional, ground-water flow model using nonlinear regression. 91-484, U.S. Geological Survey.
Hill, M.C., 1998. Methods and guidelines for effective model calibration. 98-4005, U.S. Geological Survey.
Huntley, D. and Beckett, G.D., 2002. Persistence of LNAPL sources: relationship between risk reduction and LNAPL recovery. Journal of Contaminant Hydrology, 59: 3-26.
Huntley, D., Wallace, J.W. and Hawk, R.N., 1994. Nonaqueous phase hydrocarbon in a fine-grained sandstone, 2. Effect of local sediment variability on the estimation of hydrocarbon volumes. Ground Water, 32(5): 778-783.
Irwin, R.J., Van Mouwerik, M., Stevens, L., Seese, M.D. and Basham, W., 1997. Environmental Contaminants Encyclopedia, National Park Service, Water Resources Division, Fort Collins, Colorado.

Jahn, M., 2005a. Microbial dissimilatory iron(III) reduction: Studies on the mechanism and on processes of environmental relevance. PhD. Thesis, Eberhard-Karls-University, Tübingen, 96 pp.
Jahn, M., 2005b. Final report Brand-Niedergörsdorf: Microbiology, TGF, Tuebingen.
Karickhoff, S.W., Brown, D.S. and Scott, T.A., 1979. Sorption of hydrophobic pollutants on natural sediments. Water Research, 13(3): 241-248.
Khachikian, C. and Harmon, T.C., 2000. Nonaqueous phase liquid dissolution in porous media: current state of knowledge and research needs. Transport in Porous Media, 38: 3-28.
Kolditz, O., Xie, M., Kalbacher, T., Bauer, S., Wang, W., McDermott, C., Chen, C., Beyer, C., Gronewald, J., Kemmler, D., Walsh, R., Du, Y., Park, C.-H., Hess, M., Bürger, C. and Delfs, J.-O., 2006. GeoSys/Rockflow - User Manual, University of Tuebingen, Center of Applied Geoscience, http://www.uni-tuebingen.de/zag/geohydrology/geosys.
Kueper, B.H., Abbot, W. and Farquhar, G., 1989. Experimental observations of multiphase flow in heterogeneous porous media. Journal of Contaminant Hydrology, 5: 83-95.
Kueper, B.H. and Gerhard, J.I., 1995. Variability of point source infiltration rates for two-phase flow in heterogeneous porous media. Water Resour. Res., 31(12): 2971-2980.
LABO, 2005. Berücksichtigung natürlicher Schadstoffminderungsprozesse bei der Altlastenbearbeitung. Ad-Hoc Unterausschuss "Natural Attenuation" Positionspapier, Bund/Länder-Arbeitsgemeinschaft Bodenschutz.
Lahvis, M.A. and Baehr, A.L., 1996. Estimation of rates of aerobic hydrocarbon biodegradation by simulation of gas transport in the unsaturated zone. Water Resources Research, 32: 2231-2249.
Lahvis, M.A., Baehr, A.L. and Baker, R.J., 1999. Quantification of aerobic biodegradation and volatilization rates of gasoline hydrocarbons near the water table under natural attenuation conditions. Water Resources Research, 35(3): 753-765.
Leverett, M.C., 1941. Capillary behaviour in porous solids. Trans. Am. Inst. Min. Metall. Pet. Eng., 142: 152-169.
Lønborg, M.J., P., E., P.L., B. and Rosbjerg, D., 2006. A steady state redox zone approach for modeling the transport and degradation of xenobiotic organic compounds from a landfill site. Journal of Contaminant Hydrology, 87: 191-210.
Lovley, D.R., Chapelle, F.H. and Woodward, J.C., 1994. Use of dissolved H_2 concentrations to determine distribution of microbially catalyzed redox reactions in anoxic groundwater. Environmental Science and Technology, 28(7): 1205-1210.
Lyman, W.J., Reidy, P.J. and Levy, B., 1992. Mobility and Degradation of Organic Contaminants in Subsurface Environments. C.K. Smoley, Boca Raton, 395 pp.
Mayer, A.S. and Miller, C.T., 1996. The influence of mass transfer characteristics and porous media heterogeneity on nonaqueous phase dissolution. Water Resour. Res., 32(6): 1551-1567.
Mayer, K.U., Frind, E.O. and Blowes, D.W., 2002. Multicomponent reactive transport modeling in variably saturated porous media using a generalized formulation for kinetically controlled reactions. Water Resour. Res., 38(9): 1174.
McCarthy, K.A. and Johnson, R.L., 1993. Transport of volatile compounds across the capillary fringe. Water Resour. Res., 29: 1675-1683.
McWorter, D.B. and Sunada, D.K., 1977. Groundwater and Hydraulics. Water Resources Publications, Fort Collins, CO.
Miles, B., 2003. 1-dimensional modelling of volatilisation and dissolution of kerosene in the unsaturated zone at Flughafen Niedergörsdorf. MSc. Thesis, University of Tübingen, Tübingen.

Miles, B., Kalbacher, T., Kolditz, O., Chen, C., Gronewald, J., Wang, G. and Peter, A., 2007. Development and parameterisation of a complex hydrogeological model based on high-resolution data. Environmental Geology, 52(7): 1399-1412.
Millington, R.J. and Quirk, J.M., 1961. Permeability of porous solids. Trans. Faraday Soc., 57: 1200-1207.
Monod, J., 1942. Recherches sur la croissance des cultures bacteriennes. Hermann & Cie, Paris.
Ostendorf, D.W. and Kampbell, D.H., 1991. Biodegradation of hydrocarbon vapours in the unsaturated zone. Water Resources Research, 27(4): 453-462.
Parker, J.C. and Lenhard, R.J., 1987. A model for hysteretic constitutive relations governing multiphase flow 2. Permeability-saturation relations. Water Resources Research, 23(12): 2197-2206.
Peter, A., Miles, B. and Teutsch, G., submitted. Estimation of emission from an LNAPL contaminated zone considering groundwater recharge.
Poeter, B.P. and Hill, M.C., 1997. Inverse models: A necessary next step in ground water modeling. Ground Water, 35(2): 250-260.
Postma, D. and Jakobsen, R., 1996. Redox zonation: Equilibrium constraints on the Fe(III)/SO_4-reduction interphase. Geochim. Cosmochim. Acta, 60: 3169-3175.
Prommer, H., Davis, G.B. and Barry, D.A., 1999. Geochemical changes during biodegradation of petroleum hydrocarbons: field investigations and biogeochemical modelling. Org. Geochem., 30: 423-435.
Rice, D.W., Dooher, B.P., Cullen, S.J., Everett, L.G., Kastenberg, W.E., Grose, R.D. and Marino, M.A., 1995. Recommendations to improve the cleanup process for California's leaking underground fuel tanks (LUFTS), California Environmental Protection Department, Sacramento, CA.
Rifai, H.S., Borden, R.C., Wilson, J.T. and Ward, C.H., 1995. Intrinsic Bioattenuation for Subsurface Restoration. In: R.E. Hinchee, J.T. Wilson and D.C. Downey (Editors), In-Situ and On-Site Bioreclamation Symposium. Battelle Press, San Diego, California, pp. 109-116.
Robin, M.J.L., Gutjahr, A.L., Sudicky, E.A. and Wilson, J.L., 1993. Cross-Correlated Random Field Generation With the Direct Fourier Transform Method. Water Resour. Res., 29(7): 2385-2397.
Scholl, M.A., Cozzarelli, I.M. and Christensen, S.C., 2006. Recharge processes drive sulfate reduction in an alluvial aquifer contaminated with landfill leachate. Journal of Contaminant Hydrology, 86: 239-261.
Schreiber, M.E., Carey, G.R., Feinstein, D.T. and Bahr, J.M., 2004. Mechanisms of electron acceptor utilization: implications for simulating anaerobic biodegradation. Journal of Contaminant Hydrology, 73: 99-127.
Seagren, E.A. and Moore, T.O., 2003. Nonaqueous phase liquid pool dissolution as a function of average pore water velocity. Journal of Environmental Engineering, 129(9): 786-799.
Shewchuk, J.R., 1996. Engineering a 2D quality mesh generator and Delaunay triangulator., Applied Computational Geometry: Towards Geometric Engineering. Springer Verlag, Berlin, pp. 203-222.
Simkins, S. and Alexander, M., 1984. Models for mineralization kinetics with the variables of substrate concentration and population density. Applied and Environmental Microbiology, 47(6): 1299-1306.
Sleep, B.E. and Sykes, J.F., 1989. Modeling the transport of volatile organics in variably saturated media. Water Resour. Res., 25: 81-92.

Sleep, B.E. and Sykes, J.F., 1993. Compositional simulation of groundwater contamination by organic compounds, 2. Model applications. Water Resour. Res., 29(6): 1709-1718.
Stone, H.L., 1973. Estimation of three-phase relative permeability and residual oil data. J. Can. Pet. Tech., 12: 53-61.
Stumm, W. and Morgan, J.J., 1981. Aquatic Chemistry. Wiley, New York.
Tuccillo, M.E., Cozzarelli, I.M. and Herman, J.S., 1999. iron reduction in the sediments of a hydrocarbon-contaminated aquifer. Applied Geochemistry, 14(5): 655-667.
UKEA, 2000. Guidance on the Assessment and Monitoring of Natural Attentuation of Contaminants in Groundwater. R&D Publication 95, UK Environment Agency, Bristol.
Unger, A.J.A., Forsyth, P.A. and Sudicky, E.A., 1996. Variable spatial and temporal weighting schemes for use in multi-phase compositional problems. Advances in Water Resources, 19(1): 1-27.
Unger, A.J.A., Forsyth, P.A. and Sudicky, E.A., 1998. Influence of alternative dissolution models and subsurface heterogeneity on DNAPL disappearance times. Journal of Contaminant Hydrology, 30: 217-242.
USEPA, 1997. The Rapid Optical Screening Tool (ROST) Laser-Induced Fluorescence System for Screening of Petroleum Hydrocarbons in Subsurface Soils, US EPA, Las Vegas, Nevada.
USEPA, 1999. Use of Monitored Natural Attenuation at Superfund, RCRA Corrective Action, and Underground Storage Tank Sites. OSWER Directive 9200.4-17P, USEPA, Washington DC.
Van Genuchten, M., 1980. A closed form equation for predicting the hydraulic conductivity of unsaturated soils. Soil Sci. Soc. Am. J., 44: 892-898.
Vencelides, Z., Sracek, O. and Prommer, H., 2007. Modelling of iron cycling and its impact on the electron balance at a petroleum hydrocarbon contaminated site in Hnevice, Czech Republic. Journal of Contaminant Hydrology, 89: 270-294.
Wiedemeier, T.H., Rifai, H.S., Newell, C.J. and Wilson, J.T., 1999. Natural Attenuation of Fuels and Chlorinated Solvents in the Subsurface. John Wiley & Sons, New York, 617 pp.
Wiedemeier, T.H., Swanson, M.A., Wilson, J.T., Kampbell, D.H., Miller, R.N. and Hansen, J.E., 1996. Approximation of biodegradation rate constants for monoaromatic hydrocarbons in ground water. Ground Water Monitoring Review(Summer 1996): 186-194.
Worch, E., 1993. Eine neue Gleichung zur Berechnung von Diffusionskoeffizienten gelöster Stoffe. Vom Water, 81: 289-297.
Zhu, J. and Sykes, J.F., 2000. Stochastic simulations of NAPL mass transport in variably saturated porous media. Transport in Porous Media, 39: 289-314.

Appendix: Kerosene composition and physico-chemical properties of components

Table 1. Composition of kerosene samples from the three field sites expressed as mole fractions (based on an average molecular weight for the kerosene of 166.5 gmol^{-1})

	TL1-1	TL1-16	TL2-TB 3	TL2-TB 7	TL2-TB 12	Brand SBH16	Brand SBH8
C-8	1.6E-02	2.9E-02	2.0E-02	2.2E-02	2.3E-02	9.5E-03	8.9E-03
C-9	5.5E-02	1.4E-01	5.2E-02	5.8E-02	5.5E-02	3.2E-02	3.0E-02
C-10	6.3E-02	1.2E-01	6.2E-02	6.3E-02	6.1E-02	4.2E-02	4.0E-02
C-11	5.1E-02	8.5E-02	5.4E-02	5.5E-02	5.3E-02	5.2E-02	4.8E-02
C-12	2.9E-02	4.5E-02	3.2E-02	3.2E-02	3.2E-02	2.9E-02	2.7E-02
C-13	1.3E-02	1.9E-02	1.4E-02	1.5E-02	1.4E-02	1.2E-02	1.2E-02
C-14	2.3E-03	1.6E-03	3.3E-03	3.6E-03	3.2E-03	2.3E-03	2.6E-03
C-15	4.1E-04	4.7E-04	4.9E-04	5.8E-04	4.6E-04	4.8E-04	5.1E-04
C-16	1.0E-04		1.0E-04	1.1E-04	9.6E-05	1.5E-04	1.2E-04
C-17	4.3E-05		4.3E-05	5.5E-05	4.7E-05	1.4E-04	7.9E-05
C-18	1.7E-05		1.9E-05	1.9E-05	2.1E-05	4.3E-05	1.5E-05
C-19	8.0E-06		4.8E-06	5.6E-06	7.3E-06	2.7E-05	7.3E-06
C-20			3.5E-06	4.2E-06	3.7E-06	1.7E-05	
Benzene			0.0E+00	0.0E+00	0.0E+00	7.0E-04	9.4E-05
Toluene	1.3E-04		2.1E-04	4.1E-04	4.7E-04	1.2E-03	7.4E-04
Ethyl-benzene	3.7E-03	3.9E-03	3.7E-03	2.9E-03	5.2E-03	2.7E-03	2.6E-03
p-Xylene	1.0E-02	1.2E-02	1.2E-02	1.0E-02	1.5E-02	6.5E-03	6.4E-03
o-Xylene	4.0E-03	9.4E-04	5.1E-03	5.2E-03	6.4E-03	4.6E-03	4.0E-03
Isopropyl-benzene	2.3E-03	2.4E-03	2.1E-03	1.7E-03	2.7E-03	2.7E-03	2.6E-03
Propyl-benzene	5.3E-03	5.7E-03	4.6E-03	3.3E-03	5.9E-03	5.0E-03	4.8E-03
3/4-Ethyl-teneuene	1.5E-02	1.5E-02	1.5E-02	1.2E-02	1.7E-02	1.1E-02	1.1E-02
1,3,5-TMB	4.7E-03	8.0E-03	5.4E-03	4.5E-03	5.9E-03	3.0E-03	3.0E-03
2-Ethyl-toluene	7.2E-03	8.0E-03	6.1E-03	5.2E-03	7.2E-03	7.1E-03	6.8E-03
1,2,4-TMB	2.0E-02	2.7E-02	2.2E-02	1.7E-02	2.4E-02	1.1E-02	1.1E-02
1,2,3-TMB	1.1E-02	1.4E-02	1.2E-02	9.9E-03	1.3E-02	7.2E-03	7.3E-03
Indan			1.1E-03	8.9E-04	1.3E-03		
1,2,4,5-TetraMB		8.4E-03	1.6E-03	1.3E-03	1.7E-03	9.0E-04	9.5E-04
1,2,3,5-TetraMB			8.1E-03	6.6E-03	8.3E-03	3.6E-03	3.5E-03
1,2,3,4-TetraMB			1.5E-02	1.2E-02	1.5E-02	8.0E-03	7.6E-03
Iso-Butyl-Benzene			5.0E-04	3.9E-04	5.9E-04		
1,3-Diethyl-Benzene			1.9E-03	1.6E-03	2.1E-03		
n-Butyl-Benzene			3.0E-03	2.3E-03	3.7E-03		
Napthalene	1.8E-03	4.2E-03	1.4E-03	1.4E-03	1.6E-03	1.6E-03	1.8E-03
2-Methylnapthalene	1.8E-03	3.0E-03	1.6E-03	1.7E-03	1.8E-03	1.5E-03	1.8E-03
1-Methylnapthalene	1.3E-03		1.1E-03	1.2E-03	1.2E-03	1.3E-03	1.4E-03
∑	3.2E-01	5.5E-01	3.6E-01	3.5E-01	3.8E-01	2.6E-01	2.5E-01

Table 2. Physico-chemical properties of kerosene components

	CAS Nr.	Density [g/cm^3]	Molecular weight [g/mol]	Vapour pressure [kPa]	Henry constant [-]	log K_{ow}	Solubility [mg/l]
n-Hexane	110-54-3	0.660	86.18	20.2 [9]	68.58 [9]	4.11 [11]	9.5 [11]
n-Heptane	142-82-5	0.684	100.21	6.11 [9]	92.79 [9]	5 [11]	2.93 [11]
n-Octane	111-65-9	0.703	114.23	1.88 [9]	121.0 [9]	5.15 [11]	0.66 [11]
n-Nonane	111-84-2	0.722	128.26	0.59 [13]	134 [11]	5.65 [11]	0.22 [18]
n-Decane	124-18-5	0.730	142.29	0.175 [9]	197.85 [10]	6.25 [11]	0.052 [11]
n-Undecane	1120-21-4	0.740	156.31	0.0549 [13]	74.8 [10]	6.94 [11]	0.009 [20]
n-Dodecane	112-40-3	0.749	170.34	0.0157 [9]	296.77 [10]	7.24 [11]	0.0037 [11]
n-Tridecane	629-50-5	0.756	184.37	0.00967 [18]	93.88 [10]	7.57 [18]	0.0047 [19]
n-Tetradecane	629-59-4	0.763	198.40	0.00388 [18]	46.4 [10]	7.2 [1,18]	0.0007 [18]
n-Pentadecane	629-62-9	0.768	212.42	0.00155 [18]	19.223 [10]	8.63 [18]	0.000076 [19]
n-Hexadecane	544-76-3	0.773	226.45	0.000638 [18]	9.39 [10]	8.25 [18]	0.00005 [18]
n-Heptadecane	629-78-7	0.778	240.48	0.00027 [18]	2.423 [10]	9.69 [18]	0.0002938 [21]
n-Octadecane	593-45-3	0.782	254.50	0.000116 [18]	0.367 [10]	9.32 [18]	0.000004 [18]
n-Nonadecane	629-92-5	0.785	268.53	0.000051 [18]	0.119 [10]	10.74 [18]	0.00002971 [21]
Icosane	112-95-8	0.789	282.56	0.0000226 [18]	0.013 [10]	11.27 [18]	0.0000003 [18]
Methylcyclopentane	96-37-7	0.746	84.16	18.4 [2,12]	14.8 [12,14,18]	3.37 [1,16]	42 [21]
Cyclohexane	110-82-7	0.779	84.16	12.67 [18]	7.84 [14]	3.44 [1,18]	55 [21,18]
Methylcyclohexane	108-87-2	0.769	98.19	6.13 [13]	17.6 [15]	3.61 [1,16]	14 [21,17]
iso-Pentamethylheptane	13475-82-6	0.747	170.34	0.195 [21]	9.35 [21]	5.9389 [21]	0.025 [20]
iso-Heptamethylnonane	4390-04-9	0.793	226.45	0.036 [21]	29 [21]	7.7922 [21]	0.00031 [20]
Benzene	71-43-2	0.877	78.11	12.672 [5]	0.217 [3]	2.13 [1]	1790 [6]
Toluene	108-88-3	0.867	92.14	3.805 [5]	0.244 [3]	2.73 [1]	556 [5]
Ethylbenzene	100-41-4	0.867	106.17	1.280 [13]	0.269 [7]	3.15 [1]	152 [18]
m /p-Xylene	108-38-3/106-42-3	0.864	106.17	1.106 [5]	0.26 [7]	3.2 [1]	158 [6]
o-Xylene	95-47-6	0.897	106.17	0.881 [13]	0.161 [7]	3.12 [1]	220 [18]
Styrene	100-42-5	0.905	104.15	0.800 [18]	0.109 [10]	2.95 [1]	310 [17]
1,3,5-TMB (mesitylene)	108-67-8	0.865	120.20	0.325 [18]	0.336 [10]	3.42 [1]	48.2 [17]
1,2,4-TMB	95-63-6	0.876	120.20	0.271 [5]	0.28 [8]	3.78 [1]	57 [4]
1,2,3-TMB	526-73-8	0.894	120.20	0.2 [18]	0.149 [10]	3.66 [1]	75.2 [17]
Isopropylbenzene (cumene)	98-82-8	0.862	120.20	0.61 [18]	0.464 [8]	3.66 [1]	50 [18]
n-Propylbenzene	103-65-1	0.862	120.20	0.450 [18]	0.416 [10]	3.69 [18,22]	52 [18]
3/4-Ethyltoluene	620-14-4/622-96-8	0.861	120.20	0.395 [18]	0.201 [10,9]	3.98 [23]	95 [18]
2-Ethyltoluene	611-14-3	0.887	120.20	0.33 [18]	0.176 [10]	3.53 [1]	74.6 [17]
1-Methyl-4-Isopropylbenzene	99-87-6	0.860	134.22	0.204 [18]	0.310 [9]	4.10 [1,18]	34 [18]
Indane	496-11-7	0.964	118.18	0.196 [15]	0.094 [18]	3.18 [1]	109 [17]
1,2,4,5-Tetramethylbenzene	95-93-2	0.838	134.22	0.066 [18]	1.04 [10]	4.00 [1]	3.48 [17, 18]
Diisopropylbenzene	100-18-5	0.857	162.28	0.033 [13]	0.0204 [21]	4.905 [21]	4.325 [21]
Naphthalene	91-20-3	0.997	128.18	0.011 [24]	0.0168 [9,15]	3.30 [1]	31 [18]
Methylnaphthalene	90-12-0	1.025	142.20	0.011 [18]	0.018 [9,18]	3.87 [1,18]	25 [18]

1 Hansch et al. (1995)
2 US-EPA (1994)
3 Peng and Wan (1997)
4 Verschueren (1983)
5 Shiu and Ma (2000)
6 Montgomery and Welcom (1990)
7 Dewulf et al. (1995)
8 Hansen et al. (1995)
9 Mackay and Shiu (1981)
10 Yaws and Yang (1992)
11 Mackay et al. (1993)
12 Boublik et al. (1984)
13 Daubert and Danner (1989)
14 VP/WSOL - SRC PhysProb Database
15 Hine & Mookerjee (1975)
16 Biobyte Corp. (1994)
17 Yalkowsky and Dannenfelser (1992)
18 Gustafson et al (1997)
19 Coates et al (1985)
20 Tolls et al (2001)
21 US EPA EPI-Suite (2000) (H values estimated using bond method)
22 Sangster (1994)
23 Sherblom and Eganhouse (1988)
24 Sanemaser et al (1982)

References for physico-chemical properties

Biobyte Corp., ClogP for Windows, 1.0.0, MedChem, 1994, Claremont, CA.

Boublik, T., Fried, V., Hála, E., The vapour pressures of pure substances, selected values of the temperature dependence of the vapour pressures of some pure substances in the normal and low pressure region, Physical sciences data 17, Elsevier, 1984, second revised edition, Amsterdam, The Netherlands.

Coates,M.; Connell D.W.; Barron D.W.; Aqueous solubility and octan-1-ol-water partition coefficients of aliphatic hydrocarbons.; Environ. Sci. Technol.; 19:628-32.; 1985

www.chemfinder.com

Daubert,T.E., Danner, R.P., Physical and thermodynamic properties of pure chemicals: Data compilation, Design Institute for Physical Property Data, American Institute of Chemical Engineers. Hemisphere Pub. Corp., New York, 4 Vol., 1989.

Dewulf, J.; Drijvers, D.; van Langenhove, H., Measurement of Henry's law constant as function of temperature and salinity for the low temperature range, Atmos. Environ., 1995, 29, 323-331

EPA (2000), EPI SUITE - bond estimation method for H calculation

Hansch C.; Leo A.; Hoekman D., Exploring QSAR – Hydrophobic, Electronic, and Steric Constants. Washington, DC: American Chemical Society, 1995.

Gustafson, J. B., J. Griffith-Tell, et al. (1997). Selection of representative TPH fractions based on fate and transport considerations. Massachusetts, Total Petroleum Hydrocarbon Criteria Working Group. Volume 3.

Hine, J., Mookerjee, P.K., The intrinsic hydrophilic character of organic compounds. Correlations in terms of structural contributions, J. Org. Chem., 1975, 40, 292-298.

Mackay, D.; Shiu, W.Y., A critical review of Henry's law constants for chemicals of environmental interest, J. Phys. Chem. Ref. Data, 1981, 10, 1175-1199.

Mackay, D., W.Y. Shiu and K.C. Ma, Illustrated Handbook of physical-chemical properties and environmental fate for organic chemicals - Vol. 3 Volatile organic chemicals. 1993, Boca Raton: Lewis. 916.

Montgomery JH, Welcom LM. Groundwater chemicals desk reference. Michigan: Lewis publishers Inc, 1990.

Peng J. and A. Wan, Measurement of Henry’s Constants of High-Volatility Organic Compounds Using a Headspace Autosampler. Environ. Sci. Technol. 31, 2998-3003, 1997.

Sanemasa,I.; Araki,M.; Deguchi,T.; Nagai,H; Solubility measurements of benzene and the alkylbenzenes in water by making use of solute vapor.; Bull. Chem. Soc. Jpn.; 55:1054-62; 1982

Sangster, J. 1994. LOGKOW Databank. A databank of evaluated octanol-water partition coefficients (Log P) on microcomputer diskette. Montreal, Quebec, Canada: Sangster Research Laboratories.

Sherblom, P.M. and R.P. Eganhouse, "Correlations between octanol-water partition coefficients and reversed-phase high-performance liquid chromatography capacity factors", J. Chromatogr., 454, 37-50 (1988).

Shiu W-Y and K-C Ma, Temperature Dependence of Physical-Chemical Properties of Selected Chemicals of Environmental Interest. I. Mononuclear and Polynuclear Aromatic Hydrocarbons, J. Phys. Chem. Ref. Data, 29(1), 2000.

SRC PhysProp Database, http://esc.syrres.com/interkow/PhysProp.htm

Tolls, J.; van Dijk, J.; Verbruggen, E. J. M.; Hermens, J. L. M.; Loeprecht, B.; Schuurmann, G., Aqueous Solubility-Molecular Size Relationships: A Mechanistic Case Study Using C10- to C19-Alkanes, J. Phys. Chem. A.; 2002; 106(11); 2760-2765.

United States Environmental Protection Agency, Locating and Estimating Air Emissions from Sources of Toluene. EPA-454/R-93-047, 1994.
Verschueren K (Ed). Handbook of Environmental Data on Organic Chemicals, 2nd ed. New York: Van Nostrand Reinhold Co., 1162-1163, 1983
Yaws, C.L.; Yang, H.-C., Henry's law constant for compound in water in Thermodynamic and Physical Property Data, C. L. Yaws, ed(s)., Gulf Publishing Company, Houston, TX, 1992, 181-206.
Yaws, C.L., Chemical properties handbook: physical, thermodynamic, environmental and inorganic chemicals. 1999, New York: McGraw-Hill. 779.
Yalkowsky, S. H., Dannenfelser, R. M., Aquasol Database of Aqueous Solubility, Version 5, PC Version, College of Pharmacy, Univ. of Arizona - Tucson, AZ.

In der Reihe C Hydro-, Ingenieur- und Umweltgeologie
der Tübinger Geowissenschaftlichen Arbeiten (TGA) sind bisher erschienen:

Nr. 1: Grathwohl, Peter (1989): Verteilung unpolarer organischer Verbindungen in der wasserungesättigten Bodenzone am Beispiel der leichtflüchtigen aliphatischen Chlorkohlenwasserstoffe. 102 S.

Nr. 2: Eisele, Gerhard (1989): Labor- und Felduntersuchungen zur Ausbreitung und Verteilung leichtflüchtiger chlorierter Kohlenwasserstoffe (LCKW) im Übergangsbereich wasserungesättigte/wassergesättigte Zone. 84 S.

Nr. 3: Ehmann, Michael (1989): Auswirkungen atmogener Stoffeinträge auf Boden- und Grundwässer sowie Stoffbilanzierungen in drei bewaldeten Einzugsgebieten im Oberen Buntsandstein (Nordschwarzwald). 134 S.

Nr. 4: Irouschek, Thomas (1990): Hydrogeologie und Stoffumsatz im Buntsandstein des Nordschwarzwaldes. 144 S.

Nr. 5: Sanns, Matthias (1990): Experimentelle Untersuchungen zum Ausbreitungsverhalten von leichtflüchtigen Chlorkohlenwasserstoffen (LCKW) in der wassergesättigten Zone. 122 S. **(Vergriffen!)**

Nr. 6: Seeger, Thomas (1990): Abfluß- und Stofffrachtseparation im Buntsandstein des Nordschwarzwaldes. 154 S.

Nr. 7: Einsele, Gerhard & Pfeffer, Karl-Heinz (Hrsg.) (1990): Untersuchungen über die Auswirkungen des Reaktorunfalls von Tschernobyl auf Böden, Klärschlamm und Sickerwasser im Raum von Oberschwaben und Tübingen. 151 S.

Nr. 8: Douveas, Nikon G. (1990): Verwitterungstiefe und Untergrundabdichtung beim Talsperrenbau in dem verkarsteten Nord-Pindos-Flysch (Projekt Pigai-Aoos, NW-Griechenland). 165 S.

Nr. 9: Schlöser, Heike (1991): Quantifizierung der Silikatverwitterung in karbonatfreien Deckschichten des Mittleren Buntsandsteins im Nordschwarzwald. 93 S.

Nr. 10: Köhler, Wulf-Rainer (1992): Beschaffenheit ausgewählter, nicht direkt anthropogen beeinflußter oberflächennaher und tiefer Grundwasservorkommen in Baden-Württemberg. 144 S.

Nr. 11: Bundschuh, Jochen (1991): Der Aquifer als thermodynamisch offenes System. – Untersuchungen zum Wärmetransport in oberflächennahen Grundwasserleitern unter besonderer Berücksichtigung von Quellwassertemperaturen (Modellversuche und Geländebeispiele). 100 S. **(Vergriffen!)**

Nr. 12: Herbert, Mike (1992): Sorptions- und Desorptionsverhalten von ausgewählten polyzyklischen aromatischen Kohlenwasserstoffen (PAK) im Grundwasserbereich. 111 S.

Nr. 13: Sauter, Martin (1993): Quantification and forecasting of regional groundwater flow and transport in a karst aquifer (Gallusquelle, Malm, SW-Germany. 150 S.

Nr. 14: Bauer, Michael (1993): Wasserhaushalt, aktueller und holozäner Lösungsabtrag im Wutachgebiet (Südschwarzwald). 130 S.

Nr. 15: Einsele, Gerhard & Ricken, Werner (Hrsg.) (1993): Eintiefungsgeschichte und Stoffaustrag im Wutachgebiet (SW-Deutschland). 215 S.

Nr. 16: Jordan, Ulrich (1993): Die holozänen Massenverlagerungen des Wutachgebietes (Südschwarzwald). 132 S. **(Vergriffen!)**

Nr. 17: Krejci, Dieter (1994): Grundwasserchemismus im Umfeld der Sonderabfalldeponie Billigheim und Strategie zur Erkennung eines Deponiesickerwassereinflusses. 121 S.

Nr. 18: Hekel, Uwe (1994): Hydrogeologische Erkundung toniger Festgesteine am Beispiel des Opalinustons (Unteres Aalenium). 170 S. **(Vergriffen!)**

Nr. 19: Schüth, Christoph (1994): Sorptionskinetik und Transportverhalten von polyzyklischen aromatischen Kohlenwasserstoffen (PAK) im Grundwasser - Laborversuche. 80 S.

Nr. 20: Schlöser, Helmut (1994): Lösungsgleichgewichte im Mineralwasser des überdeckten Muschelkalks in Mittel-Württemberg. 76 S.

Nr. 21: Pyka, Wilhelm (1994): Freisetzung von Teerinhaltsstoffen aus residualer Teerphase in das Grundwasser: Laboruntersuchungen zur Lösungsrate und Lösungsvermittlung. 76 S.

Nr. 22: Biehler, Daniel (1995): Kluftgrundwässer im kristallinen Grundgebirge des Schwarzwaldes – Ergebnisse von Untersuchungen in Stollen. 103 S.

Nr. 23: Schmid, Thomas (1995): Wasserhaushalt und Stoffumsatz in Grünlandgebieten im württembergischen Allgäu. 145+ 92 S.

Nr. 24: Kretzschmar, Thomas (1995): Hydrochemische, petrographische und thermodynamische Untersuchungen zur Genese tiefer Buntsandsteinwässer in Baden-Württemberg. 142 S. **(Vergriffen!)**

Nr. 25: Hebestreit, Christoph (1995): Zur jungpleistozänen und holozänen Entwicklung der Wutach (SW-Deutschland). 88 S.

Nr. 26: Hinderer, Matthias (1995): Simulation langfristiger Trends der Boden- und Grundwasserversauerung im Buntsandstein-Schwarzwald auf der Grundlage langjähriger Stoffbilanzen. 175 S.

Nr. 27: Körner, Johannes (1996): Abflußbildung, Interflow und Stoffbilanz im Schönbuch Waldgebiet. 206 S.

Nr. 28: Gewald, Thomas (1996): Der Einfluß der Desorptionskinetik bei der Freisetzung von Trichlorethen (TCE) aus verschiedenen Aquifersanden. 67 S.

Nr. 29: Schanz, Ulrich (1996): Geophysikalische Untersuchungen im Nahbereich eines Karstsystems (westliche Schwäbische Alb). 114 S.

Nr. 30: Renner, Sven (1996): Wärmetransport in Einzelklüften und Kluftaquiferen – Untersuchungen und Modellrechnungen am Beispiel eines Karstaquifers. 89 S.

Nr. 31: Mohrlok, Ulf (1996): Parameter-Identifikation in Doppel-Kontinuum-Modellen am Beispiel von Karstaquiferen. 125 S.

Nr. 32: Merkel, Peter (1996): Desorption and Release of Polycyclic Aromatic Hydrocarbons (PAHs) from Contaminated Aquifer Materials. 76 S.

Nr. 33: Schiedek, Thomas (1996): Auftreten und Verhalten von ausgewählten Phthalaten in Wasser und Boden. 112 S.

Nr. 34: Herbert, Mike & Teutsch, Georg (Hrsg.) (1997): Aquifersysteme Südwestdeutschlands - Eine Vorlesungsreihe an der Eberhard-Karls-Universität Tübingen. 162 S.

Nr. 35: Schad, Hermann (1997): Variability of Hydraulic Parameters in Non-Uniform Porous Media: Experiments and Stochastic Modelling at Different Scales. 233 S.

Nr. 36: Herbert, Mike & Kovar, Karel (Eds.) (1998): GROUNDWATER QUALITY 1998: Remediation and Protection - Posters -.- Proceedings of the GQ'98 conference, Tübingen, Sept. 21-25, 1998, Poster Papers. 146 S.

Nr. 37: Klein, Rainer (1998): Mechanische Bodenbearbeitungsverfahren zur Verbesserung der Sanierungseffizienz bei In-situ-Maßnahmen. 106 S.

Nr. 38: Schollenberger, Uli (1998): Beschaffenheit und Dynamik des Kiesgrundwassers im Neckartal bei Tübingen. 74 S.

Nr. 39: Rügner, Hermann (1998): Einfluß der Aquiferlithologie des Neckartals auf die Sorption und Sorptionskinetik organischer Schadstoffe. 78 S.

Nr. 40: Fechner, Thomas (1998): Seismische Tomographie zur Beschreibung heterogener Grundwasserleiter. 113 S.

Nr. 41: Kleineidam, Sybille (1998): Der Einfluß von Sedimentologie und Sedimentpetrographie auf den Transport gelöster organischer Schadstoffe im Grundwasser. 82 S.

Nr. 42: Hückinghaus, Dirk (1998): Simulation der Aquifergenese und des Wärmetransports in Karstaquiferen. 124 S.

Nr. 43: Klingbeil, Ralf (1998): Outcrop Analogue Studies – Implications for Groundwater Flow and Contaminant Transport in Heterogeneous Glaciofluvial Quaternary Deposits. 111 S.

Nr. 44: Loyek, Diana (1998): Die Löslichkeit und Lösungskinetik von polyzyklischen aromatischen Kohlenwasserstoffen (PAK) aus der Teerphase. 81 S.

Nr. 45: Weiß, Hansjörg (1998): Säulenversuche zur Gefahrenbeurteilung für das Grundwasser an PAK-kontaminierten Standorten. 111 S.

Nr. 46: Jianping Yan (1998): Numerical Modeling of Topographically-closed Lakes: Impact of Climate on Lake Level, Hydrochemistry and Chemical Sedimentation. 144 S.

Nr. 47: Finkel, Michael (1999): Quantitative Beschreibung des Transports von polyzyklischen aromatischen Kohlenwasserstoffen (PAK) und Tensiden in porösen Medien. 98 S.

Nr. 48: Jaritz, Renate (1999): Quantifizierung der Heterogenität einer Sandsteinmatrix (Mittlerer Keuper, Württemberg). 106 S.

Nr. 49: Danzer, Jörg (1999): Surfactant Transport and Coupled Transport of Polycyclic Aromatic Hydrocarbons (PAHs) and Surfactants in Natural Aquifer Material - Laboratory Experiments. 75 S.

Nr. 50: Dietrich, Peter (1999): Konzeption und Auswertung gleichstromgeoelektrischer Tracerversuche unter Verwendung von Sensitivitätskoeffizienten. 130 S.

Nr. 51: Baraka-Lokmane, Salima (1999): Determination of Hydraulic Conductivities from Discrete Geometrical Characterisation of Fractured Sandstone Cores. 119 S.

Nr. 52: M^{c}Dermott, Christopher I. (1999): New Experimental and Modelling Techniques to Investigate the Fractured System. 170 S.

Nr. 53: Zamfirescu, Daniela (2000): Release and Fate of Specific Organic Contaminants at a Former Gasworks Site. 96 S.

Nr. 54: Herfort, Martin (2000): Reactive Transport of Organic Compounds Within a Heterogeneous Porous Aquifer. 76 S.

Nr. 55: Klenk, Ingo (2000): Transport of Volatile Organic Compounds (VOC's) From Soilgas to Groundwater. 70 S.

Nr. 56: Martin, Holger (2000): Entwicklung von Passivsammlern zum zeitlich integrierenden Depositions- und Grundwassermonitoring: Adsorberkartuschen und Keramikdosimeter. 84 S.

Nr. 57: Diallo, Mamadou Sanou (2000): Acoustic Waves Attenuation and Velocity Dispersion in Fluid-Filled Porous Media: Theoretical and Experimental Investigations. 101 S.

Nr. 58: Lörcher, Gerhard (2000): Verarbeitung und Auswertung hyperspektraler Fernerkundungsdaten für die Charakterisierung hydrothermaler Systeme (Goldfield/Cuprite, Yellowstone National Park). 158 S.

Nr. 59: Heinz, Jürgen (2001): Sedimentary Geology of Glacial and Periglacial Gravel Bodies (SW-Germany): Dynamic Stratigraphy and Aquifer Sedimentology. 102 S.

Nr. 60: Birk, Steffen (2002): Characterisation of Karst Systems by Simulating Aquifer Genesis and Spring Responses: Model Development and Application to Gypsum Karst. 122 S**.**

Nr. 61: Halm, Dietrich & Grathwohl, Peter (Eds.) (2002): Proceedings of the 1st International Workshop on Groundwater Risk Assessment at Contaminated Sites (GRACOS). 280 S.

Nr. 62: Bauer, Sebastian (2002): Simulation of the genesis of karst aquifers in carbonate rocks. 143 S.

Nr. 63: Rahman, Mokhlesur (2002): Sorption and Transport Behaviour of Hydrophobic Organic Compounds in Soils and Sediments of Bangladesh and their Impact on Groundwater Pollution – Laboratory Investigations and Model Simulations. 73 S.

Nr. 64: Peter, Anita (2002): Assessing natural attenuation at field scale by stochastic reactive transport modelling. 101 S.

Nr. 65: Leven-Pfister, Carsten (2002): Effects of Heterogeneous Parameter Distributions on Hydraulic Tests - Analysis and Assessment. 94 S.

Nr. 66: Schwarz, Rainer (2002): Grundwasser-Gefährdungsabschätzungen durch Emissions- und Immissionsmessungen an Deponien und Altlasten. 100 S.

Nr. 67: Abel, Thekla (2003): Untersuchungen zur Genese des Malmkarsts der Mittleren Schwäbischen Alb im Quartär und jüngeren Tertiär. 187 S.

Nr. 68: Prokop, Gundula & Bittens, Martin & Cofalka, Piotr & Roehl, Karl Ernst & Schamann, Martin & Younger, Paul (Eds.) (2003): Summary Report on the 1st IMAGE-TRAIN Advanced Study Course “Innovative Groundwater Management Technologies”. 119 S.

Nr. 69: Halm, Dietrich & Grathwohl, Peter (Eds.) (2003): Proceedings of the 2nd International Workshop on Groundwater Risk Assessment at Contaminated Sites (GRACOS) and Integrated Soil and Water Protection (SOWA). 260 S.

Nr. 70: Bayer, Peter (2004): Modelling, economic assessment and optimisation of in-situ groundwater remediation systems. 78 S.

Nr. 71: Kraft, Siegfried (2004): Untersuchungen zum Langzeiteinsatz der in-situ Aktivkohlefiltration zur Entfernung von organischen Schadstoffen aus Grundwasser. 64 S.

Nr. 72: Bold, Steffen (2004): Process-based prediction of the long-term risk of groundwater pollution by organic non-volatile contaminants. 76 S.

Nr. 73: Maier, Ulrich (2004): Modelling of Natural Attenuation in Soil and Groundwater. 81 S.

Nr. 74: Susset, Bernd (2004): Materialuntersuchungen und Modellierungen zur Unterscheidung Gleichgewicht / Ungleichgewicht in Säulenversuchen für die Sickerwasserprognose organischer Schadstoffe. 100 S.

Nr. 75: Madlener, Iris (2004): Quantifizierung und Modellierung des PAK-Desorptionsverhaltens aus feinkörnigem Material mittels Säulenversuchen (DIN V 19736) und Hochdruck-Temperatur-Elution (ASE). 86 S.

Nr. 76: Henzler, Rainer (2004): Quantifizierung und Modellierung der PAK-Elution aus verfestigten und unverfestigten Abfallmaterialien. 98 S.

Nr. 77: Valley, Stephan (2004): Natural Attenuation of Volatile Organic Compounds (VOC) in Groundwater: A Method for the Determination of Compound-Specific Stable Carbon Isotope Ratios at Low Concentration Levels. 67 S.

Nr. 78: Röttgen, Klaus Peter (2004): Kritische Analyse des Aufwandes zur Erkundung von Kontaminationen in niedersächsischen Grundwassergeringleitern. 84 S.

Nr. 79: Gocht, Tilman (2005): Die vier Griechischen Elemente: Massenbilanzierung von polyzyklischen aromatischen Kohlenwasserstoffen (PAK) in Kleineinzugsgebieten des ländlichen Raumes. VI, 140, 42.

Nr. 80: Halm, Dietrich & Grathwohl, Peter (Eds.) (2004): Proceedings of the 2nd International Workshop on Integrated Soil and Water Protection (SOWA). 161 S.

Nr. 81: Prokop, Gundula, Bittens, Martin, Moraczewska-Maikut, Katarzyna, Roehl, Karl Ernst, Schamann, Martin & Younger, Paul (Eds.) (2004): Summary Report on the 3rd IMAGE-TRAIN Advanced Study Course “Quantitative Risk Assessment”. 66 S.

Nr. 82: Hoffmann, Ruth (2004): Optimierungsansätze zur Datenerfassung und Interpretation von Multielektrodenmessungen. 91 S.

Nr. 83: Kostic, Boris (2004): 3D sedimentary architecture of Quaternary gravel bodies (SW-Germany): implications for hydrogeology and raw materials geology. 103 S.

Nr. 84: Bayer-Raich, Marti (2004): Integral pumping tests for the characterization of groundwater contamination. 112 S.

Nr. 85: Piepenbrink, Matthias (2006): **– Im Druck.**

Nr. 86: Becht, Andreas (2004): Geophysical methods for the characterization of gravel aquifers: case studies and evaluation experiments. 75 S.

Nr. 87: Brauchler, Ralf (2005): Characterization of Fractured Porous Media Using Multivariate Statistics and Hydraulic Travel Time Tomography. 74 S.

Nr. 88: Stefan Gödeke (2004): Evaluierung und Modellierung des Natural Attenuation Potentials am Industriestandort Zeitz. 139 S.

Nr. 89: Nicolai-Alexeji Kummer (2005): Entwicklung eines kommerziell einsetzbaren Katalysators zur Grundwassersanierung: Katalytische Hydrodehalogenierung und Hydrierung umweltrelevanter (Chlor-) Kohlenwasserstoffverbindungen an trägergestützten Edelmetallkatalysatoren. 122 S.

Nr. 90: Beinhorn, Martin (2005): Contributions to computational hydrology: Non-linear flow processes in subsurface and surface hydrosystems. 87 S.

Nr. 91: Olsson, Asa (2005): Investigation and Modelling of Dispersion-Reaction Processes in Natural Attenuation Groundwater. 68 S.

Nr. 92: Safinowski, Michael (2005): Anaerobic biodegradation of polycyclic aromatic hydrocarbons. 65 S.

Nr.93: Bürger, Claudius (2005): Technical-economic optimization of in-situ reactive barrier systems under uncertainty. 94 S.

Nr. 94: Jahn, Michael (2006): Microbial dissimilatory iron(III) reduction: Studies on the mechanism and on processes of environmental relevance. 63 S.

Nr. 95: Bi, Erping (2006): Sorption and transport of heterocyclic aromatic compounds in soils. 63 S.

Nr. 96: Kübert, Markus (2006): Modelling and Technical-Economic Evaluation of Point Scale and Integral Approaches for Investigating Contaminant Plumes in Groundwater. 124 S.

Nr. 97: Chen, Cui (2006): Integrating GIS Methods for the Analysis of Geosystems. 157 S.

Nr. 98: Regierungspräsidium Freiburg, Abt. Landesamt für Geologie, Rohstoffe und Bergbau (Hrsg.) (2006): Untersuchungen zur Aquiferdynamik im Einzugsgebiet des Blautopfs (Oberjura, Süddeutschland). 77 S.

Nr. 99: Jochmann, Maik (2006): Solventless Extraction and Enrichment for Compound Specific Isotope Analysis. … S. **– Im Druck.**

Nr. 100: Kouznetsova, Irina (2006): Development and application of a phenomenological modelling concept for simulating the long-term performance of zero-valent iron. 99 S.

Nr. 101: Gronewold, Jan (2006): Entwicklung eines Internet Informationssystems zur Modellierung natürlicher Rückhalte- und Abbauprozesse im Grundwasser. 72 S.

Nr. 102: Rein, Arno (2006): Remediation of PCB-contaminated soils – Risk analysis of biological in situ processes. 181 S.

Nr. 103: Dietze, Michael (2007): Evaluierung von Feldmethoden zur Quantifizierung von Schadstoffminderungen im Fahnenbereich am Beispiel eines BTEX-Schadens. 156 S.

Nr. 104: Kunapuli, Umakanth (2007): Anaerobic degradation of monoaromatic hydrocarbons by dissimilatory iron(III)-reducing pure and enrichment cultures. 73 S.

Nr. 105: Miles, Benedict (2007): Practical Approaches to Modelling Natural Attenuation Processes at LNAPL Contaminated Sites. 127 S.